ADVANCED TECHNIQUE DEVELOPMENT AND CHARACTERIZATION FOR DYNAMIC PULMONARY MAGNETIC RESONANCE IMAGING

A Dissertation

Presented to

The Faculty of the School of Engineering and Applied Science

University of Virginia

In partial fulfillment

Of the requirements for the Degree

Doctor of Philosophy in Biomedical Engineering

by

William J. Garrison

December 2023

APPROVAL SHEET

This

Dissertation

is submitted in partial fulfillment of the requirements
for the degree of

Doctor of Philosophy

Author: William J. Garrison

This Dissertation has been read and approved by the examining committee:

Advisor: G. Wilson Miller

Committee Member: Craig H. Meyer

Committee Member: Richard J. Price

Committee Member: Scott T. Acton

Committee Member: John P. Mugler

Accepted for the School of Engineering and Applied Science:

Jennifer L. West, School of Engineering and Applied Science

December 2023

Abstract

Magnetic resonance imaging (MRI) of the lung is challenging due to the low proton density of lung parenchymal tissue relative to that of other soft tissue structures within the body, the high concentration of air-tissue interfaces and associated short transverse relaxation time following radiofrequency (RF) excitation within lung parenchyma, and the need to avoid or mitigate motion-related effects associated with breathing. This thesis aims to produce advancements to a number of MRI-based approaches for assessing lung structure and function.

The first work shown in this thesis demonstrates a method for performing 3D multi-phase MRI of grid-tagged hyperpolarized ^{3}He gas in the lungs during exhalation. This technique is promising for direct measurement of volume change during the breathing cycle on both a global and regional basis, for quantification of lung biomechanical quantities related to pulmonary compliance, such as regional strain values, and for visualization and assessment of global and regional biomechanical abnormalities. The approach described herein takes advantage of the predictable distribution of k-space energy imposed by using an RF pulse train to apply a tag pattern to inhaled hyperpolarized ^{3}He. Dynamic images of tagged ^{3}He were collected during exhalation using this technique, and multiple-time-point displacement and strain maps and lobar strain profiles were calculated from tagged ^{3}He images collected as described.

The second work shown in this thesis seeks to improve dissolved-phase ^{129}Xe MRI of the lung, a technique for visualization and quantification of pulmonary gas exchange efficacy, by characterizing dependence of quantitative gas-exchange metrics derived from dissolved-phase ^{129}Xe MRI on lung volume during imaging in healthy individuals and in individuals with chronic obstructive pulmonary disease (COPD). Linear relative-difference relationships between gas-exchange metrics and lung volume were observed and characterized in healthy and diseased subject samples. Significant differences in some of these metrics between healthy individuals and individuals with COPD were observed, but were largely eliminated upon correcting for lung-volume contribution by projecting signal ratios to expected values at reference volumes specific to each target inflation level. This result demonstrates the need for careful consideration of volume-related effects when comparing results in individuals with COPD, who frequently present with chronic lung hyperinflation, with those in healthy individuals.

The third work shown in this thesis seeks to demonstrate an optimized proton lung MRI approach, in which an ultrashort echo time, balanced steady-state free precession pulse sequence designed to maximize sampled signal in lung tissue is combined with temporally-constrained compressed sensing reconstruction, permitting generation of motion-resolved, high-resolution, high-quality 3D image frames at a range of positions in the breathing cycle. This approach produces high-signal, high-resolution lung images at end-of-exhalation collected during free breathing, with work ongoing to improve image quality in non-end-of-exhalation frames by reducing blurring of moving features at these respiratory phases.

Acknowledgments

I would first like to thank my advisor, Dr. Wilson Miller, for his incredible mentorship and unflagging support throughout my graduate career. When I first visited UVA as a prospective graduate student, I did not actually interview with Wilson, and only met and interacted with him relatively briefly over the course of my visit. Even in that short time, it was clear that his expertise and personality would make him a fantastic advisor, and I jumped at the opportunity to rotate in, and eventually join, his laboratory.

My time working with Wilson as a graduate student has taught me more than I would have thought possible about MRI, science, and teaching, and has shaped who I am and who I strive to be in massive ways. Wilson is unflinchingly positive and optimistic, celebrating successes and tirelessly working through obstacles and difficulties. He is incredibly supportive of me and my goals, and never fails to be a listening ear and a kind friend to me. He is an amazing role model to me as a scientist, an educator, and a human being, and will remain an example for me to follow for the rest of my life and academic career.

I am grateful to a number of other professors and researchers that have helped me in my time at UVA. I would like to thank my committee, Drs. Craig Meyer, Rich Price, Scott Acton, and John Mugler, for their input on this thesis and on my graduate work in general. I would also like to thank Dr. Gustavo Rohde for his excellent instruction in several graduate courses on imaging and mathematics, and Drs. Mike Shim, Jaime Mata, Zach Miller, Mu He, Kun Qing, Nick Tustison, Alan Ropp, and Jing Cai for their input, assistance, and guidance on my research. I also thank Jim Patrie for his assistance with the statistical methods for one of the projects discussed in this work, and Roselove Nunoo-Asare, Rene Herrera, Carol Bampoe, Jamie Weathersbee, and Jose Reyes for their help in conducting the human studies described in this work.

I also appreciate the efforts of several professors who shaped my undergraduate experience and thereby paved the way for my graduate success. I would like to thank the instructors of two incredibly memorable courses I took at Northwestern – Dr. Michael Peshkin, whose amazing course on electronics design ignited my passion for signal processing and electronics, and Dr. Robert Wallace, whose thought-provoking course on Thucydides' History of the Peloponnesian War challenged me to develop and improve my writing and critical reading abilities. I would also

Table of Contents

List of Abbreviations

1D	One-dimensional
2D	Two-dimensional
3D	Three-dimensional
4D	Four-dimensional
ADC	Apparent diffusion coefficient
ANTsPyNet	Advanced Normalization Toolbox in Python with Neural Networks
bSSFP	Balanced steady-state free precession
CI	Confidence interval
COPD	Chronic obstructive pulmonary disease
CS	Compressed sensing
CSSR	Chemical shift saturation recovery
CT	Computed tomography
CV	Coefficient of variation
DIR	Deformable image registration
FEV_1	Forced expiratory volume in one second
FOV	Field of view
FVC	Forced vital capacity
GRASP	Golden-angle radial sparse parallel
HPG	Hyperpolarized gas
ICC	Intraclass correlation coefficient
IDEAL	Iterative decomposition of water and fat with echo asymmetry and least-squares estimation
IPF	Idiopathic pulmonary fibrosis
LoA	Limit of agreement
Mbr	Alveolar membrane and blood plasma
MRI	Magnetic resonance imaging
NMR	Nuclear magnetic resonance
NUFFT	Non-uniform fast Fourier transform
PACE	Prospective acquisition correction
PAP	Pulmonary alveolar proteinosis
PCA	Principal component analysis
POCS	Projection onto convex sets
RBC	Red blood cell

RF	Radiofrequency
RMS	Root mean square
ROI	Region of interest
RV	Residual volume
SEOP	Spin-exchange optical pumping
SNR	Signal-to-noise ratio
TLC	Total lung capacity
TR	Repetition time
UTE	Ultrashort echo time
XD-GRASP	Extra-dimensional golden-angle radial sparse parallel

List of Figures

List of Tables

Chapter 1: Introduction

1.1. Magnetic resonance imaging

Magnetic resonance imaging (MRI) is a medical imaging technique that can be used to image and characterize anatomical structures and physiological processes in humans. Among the advantages of MRI are its flexible methods and tunable parameters that permit high-contrast imaging of a wide variety of tissue types and physiological processes, its sensitivity to a diverse set of diseases and physical ailments, and its safety and potential for serial imaging given its lack of ionizing radiation. Novel MRI acquisition and image reconstruction methods have been developed at a rapid rate since the technique's invention and continue to be developed in the present day. This thesis seeks specifically to continue this development process for various types of MRI of the human lung.

The description of basic MRI principles given in the ensuing sections is drawn heavily from *Magnetic Resonance Imaging: Physical Principles and Sequence Design* by Brown *et al* (1).

1.1.1. Polarization of spin-½ nuclei

The signal detected in nuclear magnetic resonance (NMR) and MRI techniques originates from the magnetic moments of nuclei contained in an external magnetic field B_0. The magnetic moment of a nucleus $\vec{\mu}$ is related to its spin angular momentum $\vec{S}$ as follows:

$$\vec{\mu} = \gamma \vec{S} \tag{1.1}$$

where γ is the gyromagnetic ratio of the nucleus.

For a spin-½ particle such as a hydrogen-1, helium-3, or xenon-129 nucleus in a field B_0, the wave functions $\psi_{\pm}$ of the spin component operator S_z have the following eigenvalues:

$$m_s \hbar = \pm \frac{1}{2} \hbar \tag{1.2}$$

such that:

$$S_z \psi_{\pm} = \pm \frac{1}{2} \hbar \psi_{\pm} \tag{1.3}$$

where $\hbar = h/(2\pi)$ is the reduced Planck constant. These eigenvalues correspond with alignment and anti-alignment of the spin to the field B_0. The energy levels of the spin in these two states are as follows:

$$\epsilon_{\pm} = -\vec{\mu} \cdot \vec{B} = -\gamma \vec{S} \cdot \vec{B} = -\gamma m_s \hbar B_0 = \pm \frac{\hbar \omega_0}{2} \tag{1.4}$$

where $\omega_0 = \gamma B_0$ is the precession frequency, or Larmor frequency, of the spins in the magnetic field B_0. The energy difference of the two states is therefore as follows:

$$\Delta \epsilon = \epsilon_+ - \epsilon_- = \hbar \omega_0 \tag{1.5}$$

The Boltzmann factor relating the probability and number of anti-aligned spins $N_{\downarrow}$ to aligned spins $N_{\uparrow}$ at thermal equilibrium is calculated from the energy difference of the respective states as follows:

$$\frac{N_{\downarrow}}{N_{\uparrow}} = e^{-\frac{\Delta \epsilon}{kT}} = e^{-\frac{\hbar \omega_0}{kT}} \tag{1.6}$$

where k is the Boltzmann constant and T is the temperature of the sample in Kelvin. The polarization of the sample can then be written as follows using the above ratio:

$$P = \frac{N_{\uparrow} - N_{\downarrow}}{N_{\uparrow} + N_{\downarrow}} = \frac{1 - \frac{N_{\downarrow}}{N_{\uparrow}}}{1 + \frac{N_{\downarrow}}{N_{\uparrow}}} = \frac{1 - e^{-\frac{\hbar \omega_0}{kT}}}{1 + e^{-\frac{\hbar \omega_0}{kT}}} = \tanh\left(\frac{\hbar \omega_0}{2kT}\right) = \tanh\left(\frac{\gamma h B_0}{4\pi kT}\right) \tag{1.7}$$

For $\tanh(x)$ where $x \ll 1$ (in this case, where $kT \gg \gamma h B_0$), we have that $\tanh(x) \approx x$, and so the polarization P can be approximated as follows:

$$P = \tanh\left(\frac{\gamma h B_0}{4\pi kT}\right) \approx \frac{\gamma h B_0}{4\pi kT} \tag{1.8}$$

The magnetization per unit volume of a sample in a magnetic field is defined as the sum of the

individual magnetic moments in the sample divided by the volume. Understanding that the net number of spins aligned with the field is equivalent to the number of spins in the sample times the polarization and magnetic moment of spins in the sample, the net magnetization per unit volume of the sample is expressed as follows for a spin population at thermal equilibrium in a field $\vec{B} = B_0\hat{z}$:

$$\vec{M}_0 = \frac{1}{V}\sum_{i=1}^{N}\vec{\mu}_i = \frac{NP\vec{\mu}}{V} \approx \frac{N}{V} \cdot \frac{\gamma h B_0}{4\pi kT} \cdot \gamma m_s \hbar \hat{z} = n\frac{\gamma^2\hbar^2 B_0}{4kT}\hat{z} \qquad (1.9)$$

where $n = N/V$ is the number density of spins per volume. For a large volume with spatially varying number density, the magnetization is given as follows as a function of position:

$$\left|\vec{M}_0(\vec{r})\right| = n(\vec{r})\frac{\gamma^2\hbar^2 B_0}{4kT} \qquad (1.10)$$

For a thermally polarized sample of ^{1}H-dense media, the polarization P of the ^{1}H is approximately 5 ppm at body temperature in a static 1.5 T magnetic field (Table 1.1). However, the high ^{1}H spin density per unit volume of aqueous tissue (~10^{19} molecules per cubic millimeter) results in a high enough magnetization to produce detectible signal within such a field at thermal polarization.

Nucleus	$\gamma/(2\pi)$ (MHz/T)	f_0 (MHz)	P_{therm} (ppm)
^{1}H	42.6	63.9	4.94
^{3}He	-32.4	-48.7	3.76
^{129}Xe	-11.8	-17.7	1.37

Table 1.1: Gyromagnetic ratio $\gamma/(2\pi)$, frequency f_0 in a 1.5 T magnetic field, and thermal polarization in a 1.5 T magnetic field at body temperature for hydrogen-1, helium-3, and xenon-129.

The thermal polarization and gyromagnetic ratios of spin-½ noble gases ^{3}He and ^{129}Xe are each of a similar order of magnitude to those of ^{1}H (Table 1.1). However, because helium and xenon occupy a gaseous state at physiologically relevant temperatures, the spin density per unit volume (and therefore the magnetization per unit volume) of ^{3}He and ^{129}Xe is far lower than that of ^{1}H in

aqueous tissue. In order to increase magnetization of ^{3}He and ^{129}Xe and facilitate MRI using these agents, hyperpolarization techniques such as spin-exchange optical pumping (SEOP) can be used to polarize samples of ^{3}He and ^{129}Xe to several orders of magnitude above thermal polarization. SEOP hyperpolarizers available at research institutions can polarize ^{3}He to approximately 60% (i.e., 600,000 ppm) and ^{129}Xe to approximately 40% (i.e., 400,000 ppm) (2–4). The ^{3}He and ^{129}Xe polarization tends toward its thermal equilibrium over time, however, and the hyperpolarized state is therefore transient.

1.1.2. Spin dynamics and the Bloch equation

The fundamental equation of motion for a single magnetic moment contained in a magnetic field is as follows:

$$\frac{d\vec{\mu}_i}{dt} = \gamma \vec{\mu}_i \times B \tag{1.11}$$

The above equation describes Larmor precession, or the precession of a magnetic moment about an external magnetic field. The magnitude of the Larmor frequency in units of radians/second is equal to γB.

Considering an ensemble of spins with the same phase and experiencing the same magnetic field B (hereafter referred to as an isochromat), and plugging in the relationship between the net magnetization per unit volume and individual magnetic moments described earlier, we can produce an expression describing the motion of the isochromat magnetization as follows:

$$\frac{1}{V}\sum_{i=1}^{N}\frac{d\vec{\mu}_i}{dt} = \frac{\gamma}{V}\sum_{i=1}^{N}\vec{\mu}_i \times B$$
$$\frac{d\vec{M}}{dt} = \gamma \vec{M} \times \vec{B} \tag{1.12}$$

That is, the isochromat as a whole exhibits Larmor precession behavior, neglecting spin interactions with each other and with their surroundings.

For an isochromat not oriented along the axis of the magnetic field (considered here to be oriented along the z-axis), thermal interactions of the spins with the lattice of nearby atoms will

tend to drive the magnetization toward its minimum energy state of orientation along the axis of the field. The rate of change of the magnetization component oriented along the axis of the field (hereafter called the longitudinal magnetization) is proportional to the difference between the equilibrium longitudinal magnetization and the current longitudinal magnetization, as follows:

$$\frac{d\vec{M}}{dt} = \frac{M_0 - M_z}{T_1}\hat{z} \tag{1.13}$$

The empirically-determined time constant T_1 describes the rate of longitudinal relaxation, and varies across nuclei and for different tissues and magnetic field strengths.

Spins also experience small magnetic fields associated with neighboring spins, and thus exhibit slightly varying precessional frequencies. This leads to loss of coherent magnetization normal to the axis of the magnetic field (hereafter called the transverse magnetization) separate from the loss due to longitudinal relaxation. Considering the isochromat in a reference frame rotating about the z-axis at the Larmor frequency γ and thereby ignoring Larmor precession of the isochromat, this loss of coherent transverse magnetization can be described as follows:

$$\frac{d\vec{M}_{xy}}{dt} = -\frac{M_{xy}}{T_2} \tag{1.14}$$

As with T_1, T_2 is determined empirically and varies across imaged media and magnetic field strengths.

Combining the three described motion components (Larmor precession, longitudinal relaxation, and transverse relaxation) yields the following expression for the motion of the isochromat magnetization:

$$\frac{d\vec{M}}{dt} = \gamma\vec{M} \times \vec{B} + \frac{M_0 - M_z}{T_1}\hat{z} - \frac{M_{xy}}{T_2} \tag{1.15}$$

This motion equation, called the Bloch equation, has the following solution for magnetization over time along each of the three dimensions in a constant magnetic field B_0:

$$M_x(t) = e^{-t/T_2}\big(M_x(0)\cos\omega_0 t + M_y(0)\sin\omega_0 t\big) \tag{1.16}$$

$$M_y(t) = e^{-t/T_2}\big(M_y(0)\cos\omega_0 t - M_x(0)\sin\omega_0 t\big)$$

$$M_z(t) = M_z(0)e^{-t/T_1} + M_0\big(1 - e^{-t/T_1}\big)$$

where $\omega_0 = \gamma B_0$ is the Larmor frequency. The steady-state solution at $t \to \infty$ is $M_x = M_y = 0$, $M_z = M_0$, corresponding to the minimum-energy situation in which the isochromat magnetization is oriented along the axis of the magnetic field. Evolution of the magnetization over time from a starting orientation normal to the magnetic field axis is depicted in Fig. 1.1.
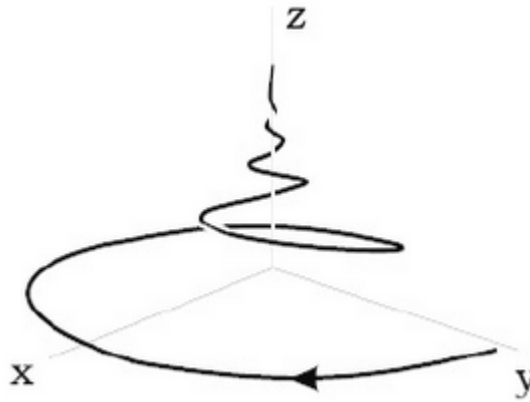
Figure 1.1: Schematic of the motion of the trajectory of the tip of a magnetization vector *M* in an external magnetic field B_0 oriented along the *z*-axis, starting from the position $M_x = M_z = 0$, $M_y = M_0$. The magnetization precesses about the axis of the magnetic field, decays in the transverse (*x-y*) plane, and regrows along the longitudinal (*z*-) axis. The equilibrium magnetization is equal to $M_x = M_y = 0$, $M_z = M_0$. Reproduced from Brown *et al (1)*.

The steady state toward which the magnetization inevitably evolves is independent of the initial state of the system. Notably, this means that for hyperpolarized media imaged using MRI, the magnetization will evolve toward thermal equilibrium over time, rather than toward the initial starting longitudinal magnetization of the hyperpolarized substance (which is much higher than the longitudinal magnetization at thermal equilibrium).

Inhomogeneities in the external magnetic field can also drive dephasing and loss of coherent magnetization in the sample. The time constant used to describe this behavior is called T_2'. The time constant T_2^* describing combined loss of coherent transverse magnetization due to spin-spin interactions and magnetic field inhomogeneities can be expressed as follows:

$$\frac{1}{T_2^*} = \frac{1}{T_2} + \frac{1}{T_2'} \tag{1.17}$$

1.1.3. Excitation of spins using a radiofrequency field

Detectible MR signal is generated by induction of an electromotive force in a coil of wire, via Larmor precession of nearby spins. In order to produce detectible MR signal, the spins must therefore be "excited," or perturbed from their equilibrium state of alignment with the magnetic field. Excitation is performed using a radiofrequency (RF) field.

In order to describe more easily the action of the RF field on the spins, a reference frame rotating about the z-axis at the Larmor frequency can be denoted using axis labels x', y', and z' (where z and z' are identical). A circularly-polarized RF field B_1 rotating at the Larmor frequency can then be described as follows:

$$\vec{B}_1 = B_1 \hat{x}' \tag{1.18}$$

and the total external magnetic field experienced by the spins as a result of B_0 and B_1 in the rotating frame (rotating at angular frequency ω) is:

$$\vec{B}' = \left(B_0 - \frac{\omega}{\gamma}\right)\hat{z} + B_1 \hat{x}' \tag{1.19}$$

Plugging this expression into the Bloch equation (Eq. 1.15), assuming that $\omega = \omega_0$, and neglecting T_1 and T_2 behavior, we obtain the following expressions for motion of the magnetization in the rotating frame for a circularly-polarized RF field B_1:

$$\left(\frac{dM_{x'}}{dt}\right)' = 0$$

$$\left(\frac{dM_{y'}}{dt}\right)' = \omega_1 M_z \tag{1.20}$$

$$\left(\frac{dM_z}{dt}\right)' = -\omega_1 M_{y'}$$

where the spin frequency due to the RF field is given as $\omega_1 = \gamma B_1$. In other words, the magnetization precesses about the x'-axis along which the B_1 field is applied, tipping away from the z axis and producing transverse magnetization that will generate detectible MR signal via Larmor precession. The solutions to the above equations of motion are as follows:

$$M_{x'}(t) = M_{x'}(0)$$
$$M_{y'}(t) = M_{y'}(0)\cos\theta + M_z(0)\sin\theta \qquad (1.21)$$
$$M_z(t) = -M_{y'}(0)\sin\theta + M_z(0)\cos\theta$$

where

$$\theta = \int_0^t \omega_1(s)\,ds \qquad (1.22)$$

is given by the duration and shape of the RF pulse and is hereafter called the flip angle of the excitation. The evolution of the magnetization following an RF pulse can be described using the Bloch equation for magnetization subject only to a B_0 field, using the magnetization components immediately following RF excitation as the magnetization components at time $t = 0$.

The above assumes that all spins in the sample of interest experience the RF field and are excited equally. In practice, it is often preferred to excite only some of the spins in the sample. Commonly, a 3D volume that is relatively thin along one of the three dimensions (commonly called a *slice*) is excited for imaging. Slice-selective excitation (demonstrated here for a slice plane normal to the z-axis) is performed by applying a linear magnetic field gradient G_z to modulate the spin frequencies as a function of position:

$$f(z) = f_0 + \frac{\gamma}{2\pi}G_z z \qquad (1.23)$$

and then applying an RF pulse with bandwidth equivalent to the range of frequencies Δf corresponding to the range of spatial positions (or slice thickness) Δz:

$$BW_{rf} = \Delta f = \frac{\gamma}{2\pi}G_z \Delta z \qquad (1.24)$$

The slice thickness Δz can then be expressed as a function of the RF pulse bandwidth and the gradient G_z as follows:

$$\Delta z = \frac{BW_{rf}}{\frac{\gamma}{2\pi} G_z} \tag{1.25}$$

The desired RF excitation profile is equivalent to the rect function rect($f/\Delta f$) in the frequency domain. The corresponding temporal envelope is the inverse Fourier transform of the desired frequency profile, which is the following sinc function:

$$B_1(t) \propto sinc(\pi \Delta f t) \tag{1.26}$$

1.1.4. Position encoding in MRI

The complex MR signal as a function of time can be expressed as proportional to the electromotive force induced in nearby radiofrequency receiver coils, which is equal to the negative of the time derivative of the flux through the coil, as follows:

$$s(t) \propto emf = -\frac{d}{dt}\Phi_M(t) = -\frac{d}{dt}\int d^3r \, \vec{M}(\vec{r},t) \cdot \vec{B}^{receive}(\vec{r})$$

$$= -\frac{d}{dt}\int d^3r \left[M_x(\vec{r},t) \cdot \mathcal{B}_x^{receive}(\vec{r}) + M_y(\vec{r},t) \right. \tag{1.27}$$

$$\left. \cdot \mathcal{B}_y^{receive}(\vec{r}) + M_z(\vec{r},t) \cdot \mathcal{B}_z^{receive}(\vec{r}) \right]$$

where Φ is the flux through the coil and $\vec{B}^{receive}(\vec{r})$ is the magnetic field per unit current, called the "receive field," of the coil.

Plugging in the following for the transverse magnetization vector components as a function of position and time given by the Bloch equation:

$$M_+(\vec{r},t) = e^{-t/T_2(\vec{r})} e^{i(-\omega(\vec{r})t + \phi_0(\vec{r}))} M_\perp(\vec{r},0)$$

$$M_x = Re(M_+); \; M_y = Im(M_+); \tag{1.28}$$

we can obtain the following for $s(t)$ by evaluating the time derivative in Eq. 1.27 and neglecting the contribution of the $\underline{M_z}$ component due to the several-order-of-magnitude difference between ω and $1/T_1$ for typical nuclei imaged using MRI at typical MR field strengths:

$$
\begin{aligned}
s(t) &\propto \omega(\vec{r}) \int d^3r e^{-t/T_2(\vec{r})} \big[Re\big(iM_+(\vec{r},0)e^{-i\omega(\vec{r})t}\big) \cdot \mathcal{B}_x^{receive}(\vec{r}) \\
&\quad + Im\big(iM_+(\vec{r},0)e^{-i\omega(\vec{r})t}\big) \cdot \mathcal{B}_y^{receive}(\vec{r}) \big] \\
&= \omega_0 \int d^3r e^{-t/T_2(\vec{r})} M_\perp(\vec{r},0) \big[\sin\big(\omega(\vec{r})t - \phi_0(\vec{r})\big) \\
&\quad \cdot \mathcal{B}_x^{receive}(\vec{r}) + \cos\big(\omega(\vec{r})t - \phi_0(\vec{r})\big) \cdot \mathcal{B}_y^{receive}(\vec{r}) \big]
\end{aligned}
\tag{1.29}
$$

By representing $\mathcal{B}_x^{receive}$ and $\mathcal{B}_y^{receive}$ in terms of the position-dependent magnitude $\mathcal{B}_\perp(\vec{r})$ and angle $\theta_\mathcal{B}(\vec{r})$:

$$
\mathcal{B}_x^{receive} = \mathcal{B}_\perp(\vec{r}) \cos\theta_\mathcal{B}(\vec{r}); \quad \mathcal{B}_y^{receive} = \mathcal{B}_\perp(\vec{r}) \sin\theta_\mathcal{B}(\vec{r})
\tag{1.30}
$$

and using the trigonometric identity $\sin(a+b) = \sin(a)\cos(b) + \cos(a)\sin(b)$, we obtain:

$$
\begin{aligned}
s(t) &\propto \omega(\vec{r}) \int d^3r e^{-t/T_2(\vec{r})} M_\perp(\vec{r},0) \mathcal{B}_\perp(\vec{r}) \sin\big(\omega(\vec{r})t + \theta_\mathcal{B}(\vec{r}) \\
&\quad - \phi_0(\vec{r})\big)
\end{aligned}
\tag{1.31}
$$

Demodulation, or multiplication of the signal with a sinusoid with frequency equal to the Larmor frequency ω_0, yields the following:

$$
s(t) \propto \omega(\vec{r}) \int d^3r e^{-t/T_2(\vec{r})} M_\perp(\vec{r},0) \mathcal{B}_\perp(\vec{r}) e^{i\big((\omega_0 - \omega(\vec{r}))t - \theta_\mathcal{B}(\vec{r}) + \phi_0(\vec{r})\big)}
\tag{1.32}
$$

Assuming that the initial magnetization phase ϕ_0 and the amplitude and phase of the receive field are independent of position, neglecting T_2, generalizing the signal to include time-dependent precession frequency $\omega(\vec{r},t)$, and introducing the constant Λ that absorbs these factors and the gain factors for the receive electronics, we can write

$$s(t) = \omega(\vec{r})\Lambda B_\perp \int d^3 r M_\perp(\vec{r}, 0) e^{i(\omega_0 t + \phi(\vec{r},t))} \tag{1.33}$$

where ϕ is accumulated phase defined as follows:

$$\phi(\vec{r}, t) = -\int_0^t dt' \, \omega(\vec{r}, t') \tag{1.34}$$

Assuming the initial transverse magnetization to simply equal M_0, and introducing the effective spin density ρ that combines the true spin density and the characteristics of the receive electronics:

$$\rho(\vec{r}) = \omega(\vec{r})\Lambda B_\perp M_0(\vec{r}) \tag{1.35}$$

we can write:

$$s(t) = \int d^3 r \, \rho(\vec{r}) e^{i(\omega_0 t + \phi(\vec{r},t))} \tag{1.36}$$

The signal $s(t)$ can be represented for simplicity of the following as a function of only one spatial dimension, chosen here to be z, as follows:

$$s(t) = \int dz \, \rho(z) e^{i(\omega_0 t + \phi(z,t))} \tag{1.37}$$

by expressing ρ as a function of z as follows:

$$\rho(z) = \iint dx \, dy \, \rho(\vec{r}) \tag{1.38}$$

Application of a linear magnetic field gradient G_z along the z-direction

$$G_z = \delta B_z / \delta z \tag{1.39}$$

produces the following magnetic field B as a function of position and time:

11

$$B_z(z,t) = B_0 + zG(t) \tag{1.40}$$

and an associated distribution of spin angular frequencies:

$$\omega(z,t) = \omega_0 + \gamma zG(t) = \omega_0 + \omega_G(z,t) \tag{1.41}$$

The phase accumulated due to the applied gradient as a function of time t and position z can then be expressed as follows:

$$\phi_G(z,t) = -\int_0^t dt'\,\omega_G(z,t') = -\gamma z\int_0^t dt'\,G(t') \tag{1.42}$$

The phase of the spin population at a given time t under a linear gradient $G(t)$ can thus be expressed as a linear function of position z. Eq. 1.37 can be modified to express $s(t)$ as a function of the gradient $G(t)$ as follows:

$$s(t) = \int dz\,\rho(z)e^{i\phi_G(z,t)} = \int dz\,\rho(z)e^{-i\gamma z\int_0^t dt'\,G(t')} \tag{1.43}$$

Defining the spatial frequency quantity $k(t)$, in units of cycles per spatial length, as follows:

$$k(t) = \frac{\gamma}{2\pi}\int_0^t dt'\,G(t') \tag{1.44}$$

yields the following expression for s as a function of k:

$$s(k) = \int dz\,\rho(z)e^{-i2\pi kz} \tag{1.45}$$

In other words, the signal as a function of spatial frequency $s(k)$ forms a Fourier transform pair with the spin density as a function of spatial position $\rho(z)$ when linear gradients are implemented. The spin density can accordingly be obtained by taking an inverse Fourier transform of the signal $s(k)$ as follows:

$$\rho(z) = \int dk\,s(k)e^{i2\pi kz} \tag{1.46}$$

A 1D "image" along the *z*-axis can therefore be obtained by using linear gradients to traverse *k*-space, sampling the signal *s(k)* at a collection of sampling points. This formalism can be extended to 3D imaging as follows:

$$s(\vec{k}) = \int d^3r\, \rho(\vec{r})e^{-i2\pi\vec{k}\cdot\vec{r}}$$

$$\rho(\vec{r}) = \int d^3k\, s(\vec{k})e^{i2\pi\vec{k}\cdot\vec{r}}$$

(1.47)

A single MRI measurement can be summarized as follows: use RF excitation to excite all, or a subset, of spins in a sample contained in the magnetic field B_0; use a magnetic field gradient G_r to traverse *k*-space; and sample the detected signal in one or more RF receiver coils while the gradient G_r is carried out. For any given MR measurement type, a pulse sequence describes the particular amplitudes and timings of RF pulses and gradients that constitute the measurement.

A typical set of MRI measurements leading to the formation of an image consists of numerous iterations of the pulse sequence each carried out with differing gradients and/or RF pulses in order to sample a collection of *k*-space points sufficient for image reconstruction. For the example Cartesian coverage of 2D *k*-space where *z* is a slice-select dimension (Fig. 1.2), it is common to perform a gradient along G_y prior to readout to "phase-encode" a particular *y*-dependent phase contribution, then sample during execution of a "frequency-encode" gradient along G_x such that a line is traced through k_x-k_y space and samples are collected along that line. The process is repeated with different amplitudes of the phase-encode gradient G_y until the entirety of the necessary *k*-space has been sampled.
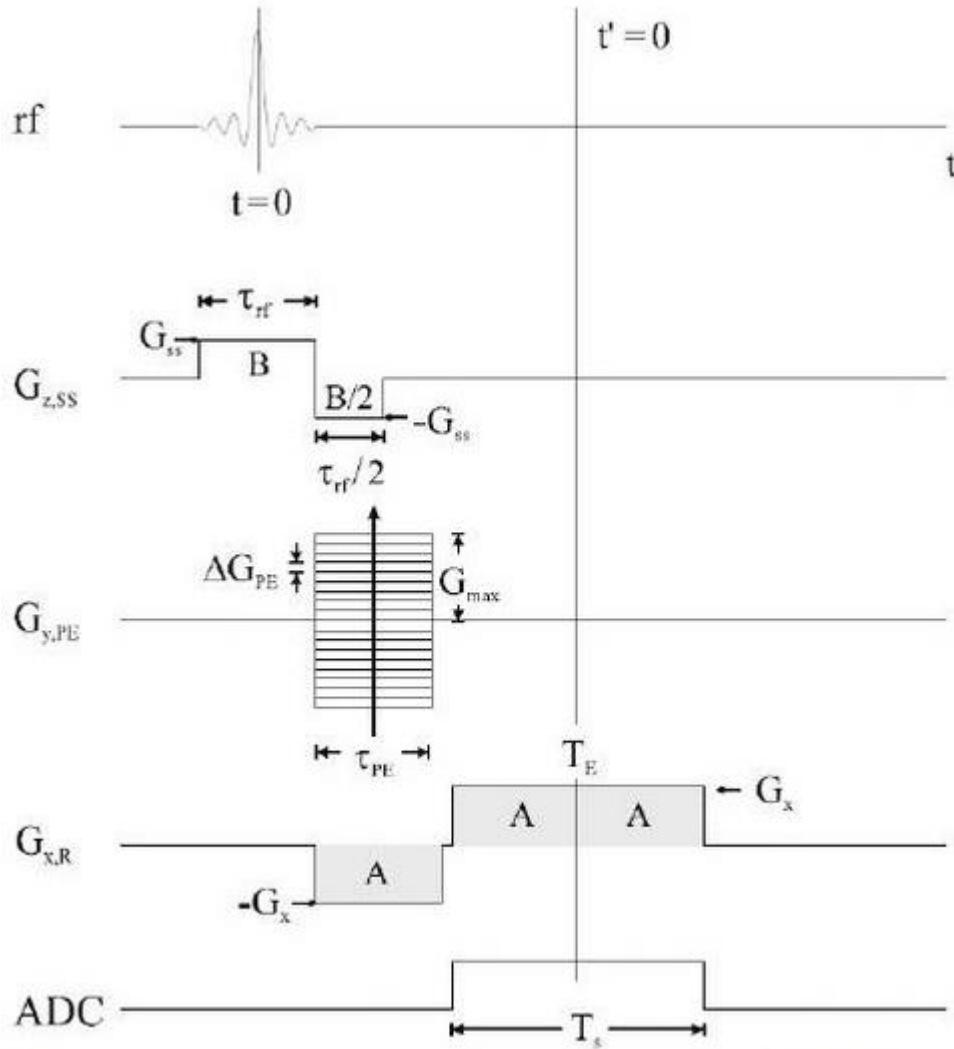
Figure 1.2: Example of a simple two-dimensional slice-selective MR pulse sequence. A slice-select gradient along G_z and a sinc-shaped RF pulse are used to excite a slice of spins normal to the z-axis. A phase-encode gradient along G_y is used to move to a point in k_y, and the y-dependent phase contribution to the sample remains unchanged throughout sampling. Finally, a frequency-encode gradient G_x is used to traverse a line in k-space at the position k_y for varying k_x, and sampling is performed throughout the traversal of k-space by G_x. Reproduced from Brown *et al* *(1)*.

The pulse sequence shown in Fig. 1.2 samples k-space lines in a Cartesian raster fashion. Various other options exist for traversal of k-space for MR sampling. Of particular interest in this work is radial sampling, in which k-space lines begin at the k-space origin and are traced outward radially toward the k-space periphery. Fig. 1.3 depicts a 2D slice-selective radial sequence.

14
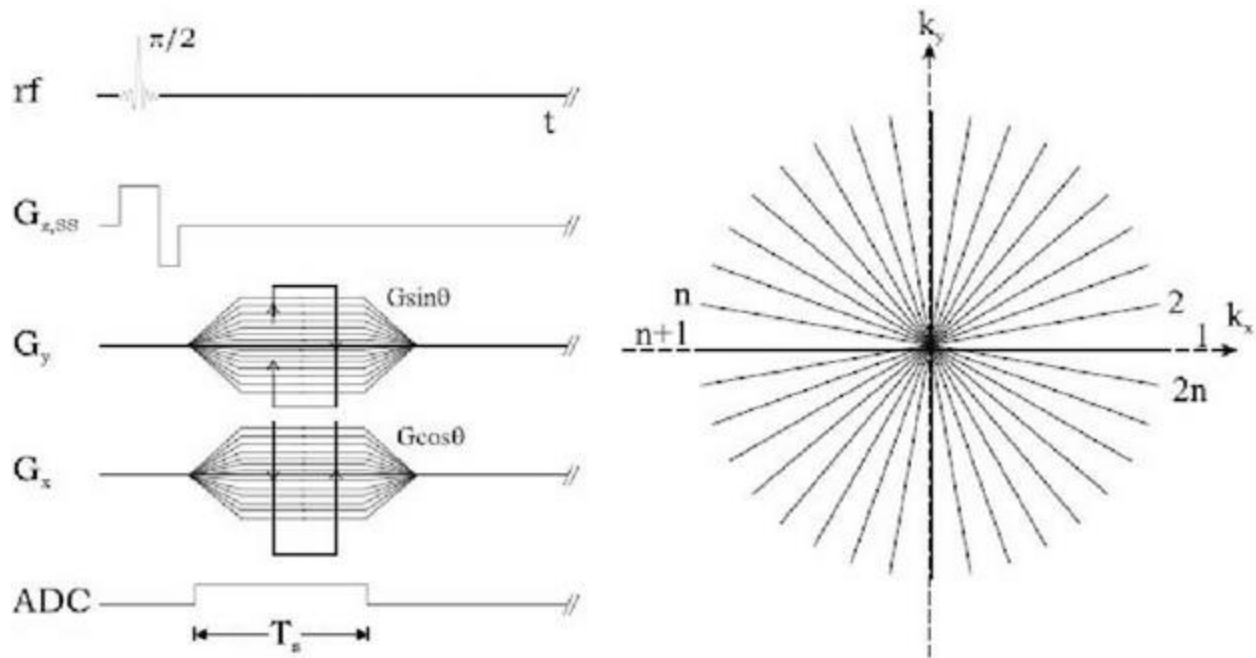
Figure 1.3: Example of a two-dimensional slice-selective radial MR pulse sequence (left) and a resulting radial *k*-space sampling matrix (right). A slice-select gradient along G_z and a sinc-shaped RF pulse are used to excite a slice of spins normal to the *z*-axis. Frequency-encode gradients G_x and G_y are used to traverse a radial line in *k*-space, and sampling is performed throughout the traversal of *k*-space by G_x and G_y. Adapted from Brown *et al (1)*.

Both the Cartesian sequence depicted in Fig. 1.2 and the radial sequence depicted in Fig. 1.3 can be performed without slice selection, permitting isotropic coverage of *k*-space in all three dimensions and allowing shorter, rectangular RF excitations to be used. For Cartesian sampling, the dimension used as the slice-select direction for 2D imaging (typically k_z) can be reformulated as a second phase-encode dimension. For radial sampling, k_z can be reformulated as a third frequency-encode direction (as k_x and k_y both already act as frequency-encode dimensions).

1.2. MR sampling and image reconstruction

1.2.1. MR sampling

The Fourier relationship between $s(k)$ and $\rho(r)$ indicates that $\rho(r)$ can be known precisely at all spatial locations with precise knowledge of $s(k)$ at all spatial frequency locations. In practice, it is only possible to sample a limited extent of *k*-space with a finite sampling period, rather than an infinite extent of *k*-space with an infinitely small sampling period. For a constant frequency-

encoding gradient executed along the x-axis, the sampling period in k-space Δk as a function of the sampling period in time Δt can be written as follows:

$$\Delta k = \frac{\gamma}{2\pi} G_x \Delta t \tag{1.48}$$

Sampling in k-space can then be described as multiplication of the k-space representation of the sampled object $s(k)$ by a sampling function $u(k)$ consisting of a Dirac comb function with infinite support and period Δk and a sampling envelope function $v(k)$ consisting of a rect function with support covering a finite region of sampling centered at the center of k-space and with width $W = 2n\Delta k$, where $2n$ is the number of sampled k-space points:

$$
\begin{aligned}
s_m(k) &= s(k) \cdot u(k) \cdot v(k) \\
&= s(k) \cdot \left(\Delta k \sum_{p=-\infty}^{\infty} \delta(k - p\Delta k) \right) \cdot rect\left(\frac{k + \frac{1}{2}\Delta k}{W} \right) \\
&= \Delta k \sum_{p=-n}^{n-1} s(p\Delta k)\delta(k - p\Delta k)
\end{aligned} \tag{1.49}
$$

The reconstructed spin density after sampling is obtained by taking the inverse Fourier transform of $s_m(k)$ as follows:

$$
\begin{aligned}
\hat{\rho}(x) &= \int_{-\infty}^{\infty} dk\, s_m(k) e^{i2\pi kx} = \int_{-\infty}^{\infty} dk\, \big(s(k) \cdot u(k) \cdot v(k)\big) e^{i2\pi kx} \\
&= \rho(x) * U(x) * V(x) \\
&= \rho(x) * \sum_{q=-\infty}^{\infty} \delta\left(x - \frac{q}{\Delta k}\right) * \left(W sinc(\pi W x) e^{-i\pi x \Delta k} \right)
\end{aligned} \tag{1.50}
$$

In other words, the reconstructed spin density after sampling is the true spin density convolved with a comb function of period $L = 1/\Delta k$ (i.e., the imaged object is replicated in image-space with center-to-center spacing of the copies equal to L) and convolved with a sinc function (i.e., the object is blurred). An example for a simple 1D object is shown in Fig. 1.4. It is apparent that if the extent A of the object exceeds the field-of-view L, coherent "copies" of the object due to

sampling will overlap the true object. The requirement that $L = 1/\Delta k > A$ in order to avoid coherent aliasing for uniformly-spaced samples is called the Nyquist criterion.
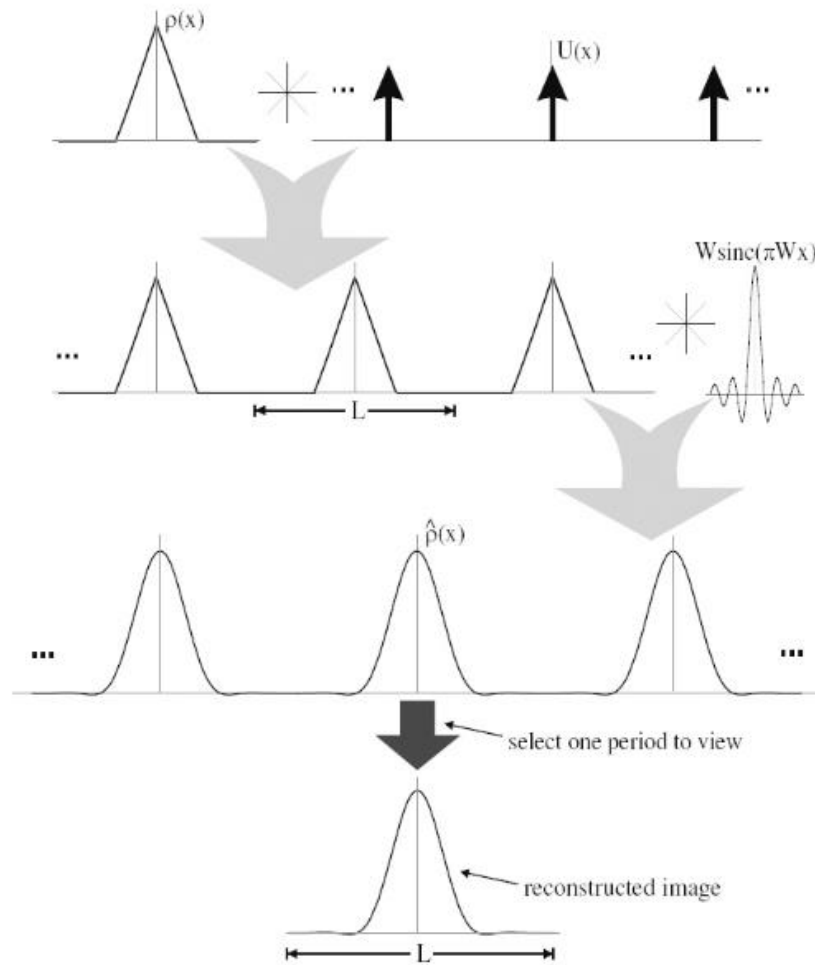
Figure 1.4: Demonstration of convolution of an object $\rho(x)$ with the Fourier transforms of the sampling function $u(k)$ and rect function $v(k)$. For this object, the field-of-view L has been chosen such that $L > A$, the extent of the object in image-space, so no overlap of the aliased copies occurs. Convolution with the sinc function due to finite sampling leads to slight blurring of image features and slight ringing near object boundaries. Reproduced from Brown *et al* (1).

For Cartesian sampling, it is trivial to sample densely enough in the frequency-encode direction to avoid aliasing, as no time penalty is imposed by doing so. However, the total imaging time scales linearly with the number of phase-encode lines that are read, and so there exists a trade-off between minimizing Δk along the phase-encode direction(s) and minimizing imaging time.

1.2.2. Under-sampling effects

Under-sampling an image, or acquiring a smaller number of lines than those required by the Nyquist criterion for the k-space matrix being covered, results in under-sampling artifacts. These artifacts can take various forms, as the creation of perfect, coherent copies in the imaging field-of-view only occurs when k-space is uniformly under-sampled (i.e., a constant Δk is still used, but is chosen such that $1/\Delta k < A$).

Fig. 1.5 depicts a simulation of various types of under-sampling artifacts that can occur for 2D imaging of an object with under-sampling in the phase-encode direction. Uniform under-sampling leads to uniform aliased copies of the object (Fig. 1.5b). Random under-sampling leads to the stacking of a large number of incoherent, shifted, low-signal-intensity copies of the object (Fig. 1.5c). Variable-density under-sampling with preferential sampling of lines near the k-space center results in decrease of image degradation due to copies, but slight blurring and ringing (Fig. 1.5d), reflecting convolution with the sinc function $V(x)$ described above. Sampling of only the central half of k-space, omitting the top and bottom quarters of k-space, eliminates the object copies entirely but introduces yet more severe blurring and ringing than seen for variable-density under-sampling (Fig. 1.5e). In all cases, the object is under-sampled by a factor of 2 (i.e., half of the necessary k-space lines to avoid under-sampling artifacts are sampled), but the resulting under-sampling artifact properties vary drastically from case to case.
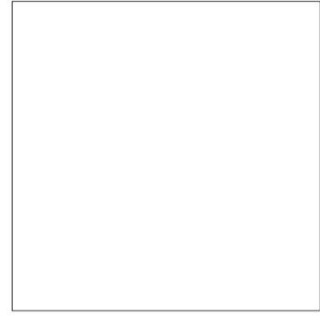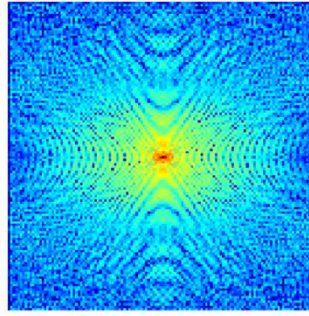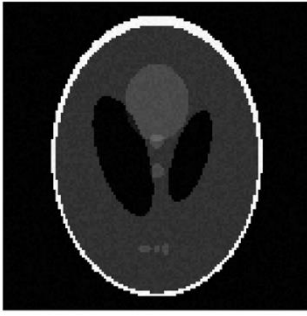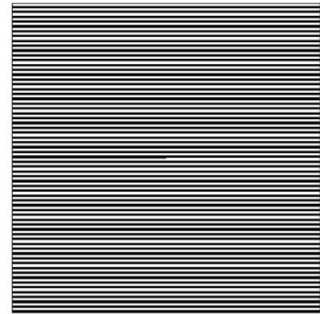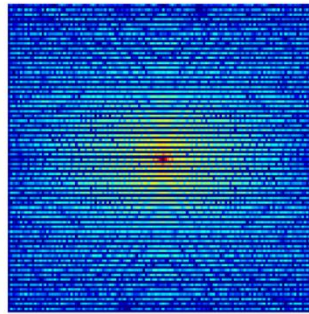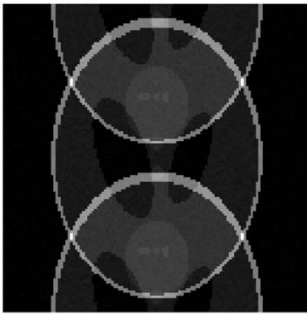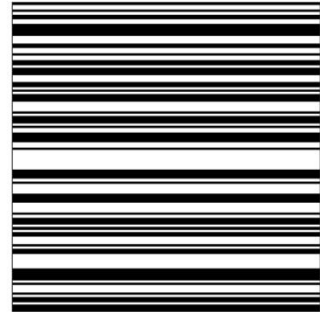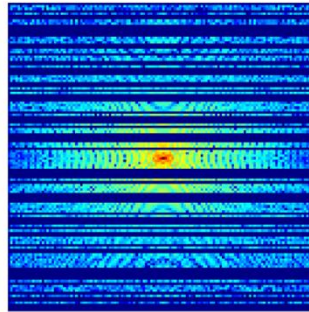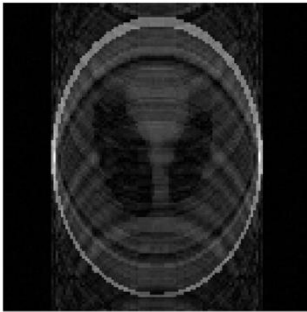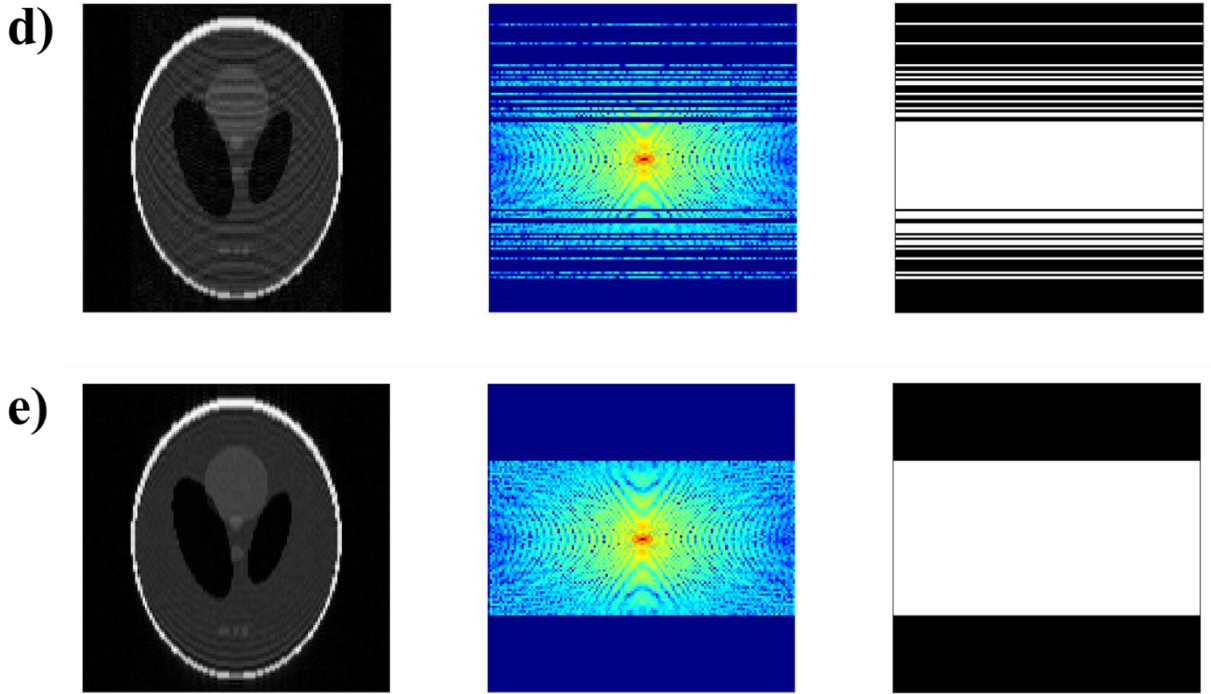
Figure 1.5: Simulated image (left column), simulated sampled k-space data (middle column), and binary sampling matrix (right column) for cases of **a)** full sampling, **b)** uniformly-spaced under-sampling, **c)** random under-sampling, **d)** variable-density under-sampling with preferential sampling of central k-space, and **e)** sampling of the central half of k-space. In all cases shown in b-e), half of the total necessary k-space lines according to the Nyquist criterion are sampled.

It can be qualitatively observed that the under-sampling artifacts produced by variable-density under-sampling with preferential sampling of the k-space center are more "noise-like" than those for other sampling schemes. This forms a key aspect of compressed sensing MRI, as discussed below.

The Nyquist criterion is less well-defined for a collection of radial MR readouts of k-space, but avoidance of under-sampling artifacts can be assured by designing a radial trajectory such that the outermost points on two adjacent rays are no more than $L = 1/\Delta k_r$ apart, where Δk_r is the circumferential distance between the two points. The minimum number of spoke-radial rays required to satisfy this condition equals π times the number of Cartesian phase-encode lines that would be required to satisfy the Nyquist criterion for the same intended FOV. Under-sampling using a radial trajectory leads to under-sampling artifacts that commonly manifest as streaking throughout the image (5). However, as these artifacts are generally not as coherent as the under-

sampling artifacts produced by uniform under-sampling for Cartesian imaging, they can often be removed as well via compressed sensing reconstruction.

1.2.3. Reconstruction of under-sampled MR images using compressed sensing

Compressed sensing (CS) approaches propose to reconstruct MR images sampled at only a fraction of the points required to satisfy the Nyquist criterion, without manifestation of severe under-sampling artifacts in the final reconstructed image (6,7). Given that MR imaging time scales essentially linearly with the number of k-space lines collected during the acquisition, CS methods offer significant potential reduction of MR imaging time without significant loss of image quality or accuracy, if carefully designed and implemented.

The following conditions are generally held to be necessary in order to produce a high-quality CS-based image reconstruction of an under-sampled MR image:

- The image must have a sparse representation in one or more known transform domains.
- The aliasing artifacts due to k-space under-sampling must be noise-like.
- The reconstruction must be performed using a method that enforces both sparse representation of the image in its known sparse transform domain(s) and consistency of the reconstructed image with the original k-space data.

The first condition is generally satisfied for MR images, as known transforms such as finite-differences and the wavelet transform are generally observed to produce sparse representation of MR images and other natural images (8). The second condition can often be satisfied by sampling in a pseudo-random fashion with higher sampling density near the k-space center and lower sampling density near the k-space periphery, as shown in Fig. 1.5d.

The third condition is satisfied by expressing the problem as a constrained under-sampling problem:

$$minimize \ \|\Psi m\|_1 \ such \ that \ \|F_u m - y\|_2^2 \leq \epsilon \qquad (1.51)$$

where Ψ is a sparsifying transform on the image m, F_u is the under-sampled Fourier transform, y is the measured under-sampled k-space data, and ϵ is an error term that controls the extent to

which the solution can differ from the measured k-space data. The L_1 norm is used for the sparsifying transform term in order to enforce sparsity in the transform space.

A simple algorithm that can be used to solve the minimization shown above is projection onto convex sets (POCS), which can be formulated as follows:

- Set y_0 equal to y, the original under-sampled k-space data.
- Perform the following set of operations iteratively:
  - Perform an inverse Fourier transform on the current y_i to generate an image:

$$m_j = F^{-1}y_j \tag{1.52}$$

  - Apply the chosen sparsifying transform to the image to generate a representation of the image in the sparse domain:

$$\psi_j = \Psi m_j \tag{1.53}$$

  - Apply soft thresholding to each element of the image representation in the sparse domain:

$$\psi_j(\overline{x}, \lambda) = \begin{cases} 0 & if\ |\psi_j(\overline{x})| \leq \lambda \\ \dfrac{(|\psi_j(\overline{x})| - \lambda)}{|\psi_j(\overline{x})|}\psi_j(\overline{x}) & if\ |\psi_j(\overline{x})| > \lambda \end{cases} \tag{1.54}$$

    where $\overline{x}$ is the coordinates of a given pixel or voxel in the sparsifying transform domain and λ is a user-chosen weighting parameter.

  - Perform the inverse of the sparsifying transform on ψ_j to obtain a new image estimate m_j, and perform a Fourier transform on m_j to generate a k-space estimate y_j.
  - Enforce hard data consistency in the frequency domain by setting all values of y_j that were originally sampled in y_0 to their original values in y_0:

$$y_{j+1}(\overline{y}) = \begin{cases} y_0(\overline{y}) & if\ y_0(\overline{y}) > 0 \\ y_j(\overline{y}) & otherwise \end{cases} \tag{1.55}$$

- Repeat the above steps until one of the following two conditions is satisfied:

- A preset number of iterations have been performed.
- The optimization converges to a solution as assessed below, where ϵ_m is a user-defined error term:

$$\|m_{j+1} - m_j\| < \epsilon_m \qquad (1.56)$$

The final image estimate m is then the inverse Fourier transform of the final estimate of the k-space data y_{end}. The above iterative process can be thought of as producing a solution of Eq. 1.51 such that ϵ is chosen to equal zero (as it is enforced in every iteration that $F_u m = y$).

Fig. 1.6 shows the result of performing the POCS procedure above for each of the under-sampled 2D image cases shown in Fig. 1.5, using a 2D Haar wavelet transform as the sparsifying transformation Ψ, setting $\lambda = 0.01$, and performing 200 iterations. Variable-density under-sampling with preferential sampling of the k-space center displays the lowest root-mean-square error with respect to the original image.
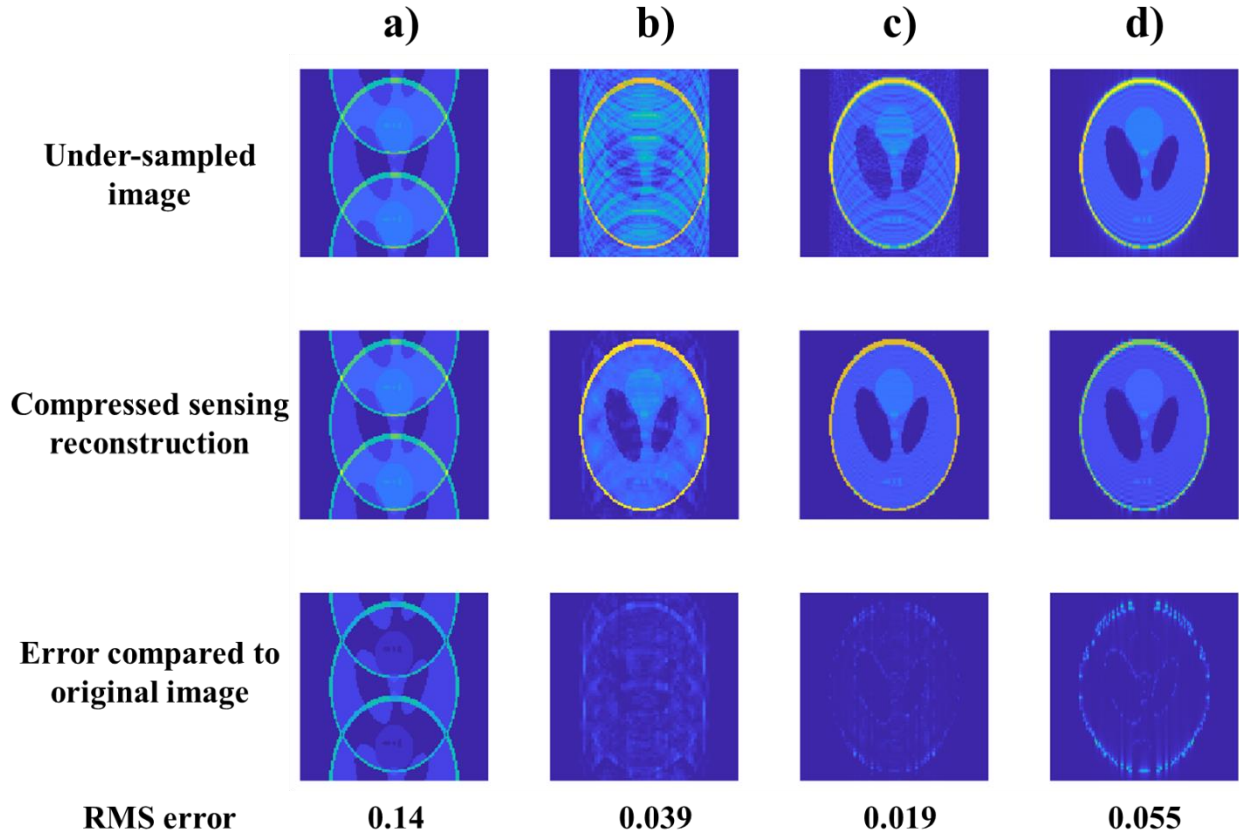
Figure 1.6: Simulated image (top row), projection onto convex sets-based compressed sensing reconstruction (middle row), and error with respect to original fully-sampled image as shown in Fig. 1.5a (bottom row) for cases of **a)** uniformly-spaced under-sampling (as shown in Fig. 1.5b), **b)** random under-sampling (as shown in Fig. 1.5c), **c)** variable-density under-sampling with preferential sampling of central *k*-space (as shown in Fig. 1.5d), and **d)** sampling of the central half of *k*-space (as shown in Fig. 1.5e). Root-mean-square (RMS) error with respect to the original image is shown at the bottom of the figure for each under-sampling type.

In practice for under-sampled image reconstruction, the optimization problem described in Eq. 1.51 is usually formulated as an unconstrained optimization problem in Lagrangian form, as follows:

$$\widetilde{m} = \arg\min_{m} \|F_u m - y\|_2^2 + \lambda \|\Psi m\|_1 \tag{1.57}$$

where λ is a weighting parameter that balances sparsification in the sparse transform domain with data consistency. More than one sparsifying term can potentially be used in the image reconstruction, and reconstruction of image series using a sparsifying term assessed across a

temporal or pseudo-temporal dimension (such as temporal finite-differences) is well characterized (9,10).

Common solution methods for compressed-sensing problems of the form above include nonlinear conjugate gradient descent (11,12) and alternating direction method of multipliers (13). The following algorithm describes an implementation of nonlinear conjugate gradient descent to solve the optimization problem described in Eq. 1.57 for an image m:

- Compute a gradient descent direction for the objective function. For the first iteration, this direction is the negative of the objective function gradient:

$$p_0 = -g_0 = -\nabla f(m_0) \tag{1.58}$$

  For subsequent iterations, identify a conjugate gradient direction as follows:
  - Calculate the new steepest-ascent gradient direction:

$$g_j = \nabla f(m_j) \tag{1.59}$$

  - Choose a descent direction based on the current steepest-descent direction and the previous descent direction as follows:

$$p_j = -g_j + \beta_j p_{j-1} \tag{1.60}$$

  where the scalar factor β_j can be calculated using a variety of methods, including the following (11):

$$\beta_j = \frac{g_j^T g_j}{g_{j-1}^T g_{j-1}} \tag{1.61}$$

- Perform backtracking line search as follows:
  - Start with a chosen step size t and evaluate the value of the objective function for a step of size t and for a step of size 0 along the current gradient direction p_j.
  - Check whether the Armijo rule (14) is satisfied:

$$f(m_j + tp_j) \le f(m_j) - \alpha t \nabla f(m_j)^T p_j \tag{1.62}$$

  where α is a small pre-set factor.
  - If the above inequality is satisfied, accept the current step size t and proceed. If not, multiply the step size by a set factor greater than 0 and less than 1 and repeat the above.

- Perform the gradient step using the gradient p_j and the step size t:

$$m_{j+1} = m_j + t p_j \qquad (1.63)$$

- Check whether the maximum number of iterations has been reached or whether another stopping criterion (such as the norm of the gradient descent direction falling below a set tolerance) has been satisfied. Perform another iteration if neither of these have occurred.

1.3. Lung anatomy and physiology

1.3.1. Lung gross anatomy and motion during breathing

The lungs are situated in separate pleural sacs within the thoracic cavity, with their apices in the root of the neck and their bases resting on the diaphragm. Each lung is divided into lobes by one or more fissures (Fig. 1.7). The left lung is divided by an oblique fissure into superior and inferior lobes, while the right lung is divided by an oblique fissure and a horizontal fissure into superior, middle, and inferior lobes. There is significant variation between individuals in the completeness and orientation of the fissures (15,16). In particular, the right horizontal fissure is commonly reported to be incomplete or absent in as many as 80% of individuals.
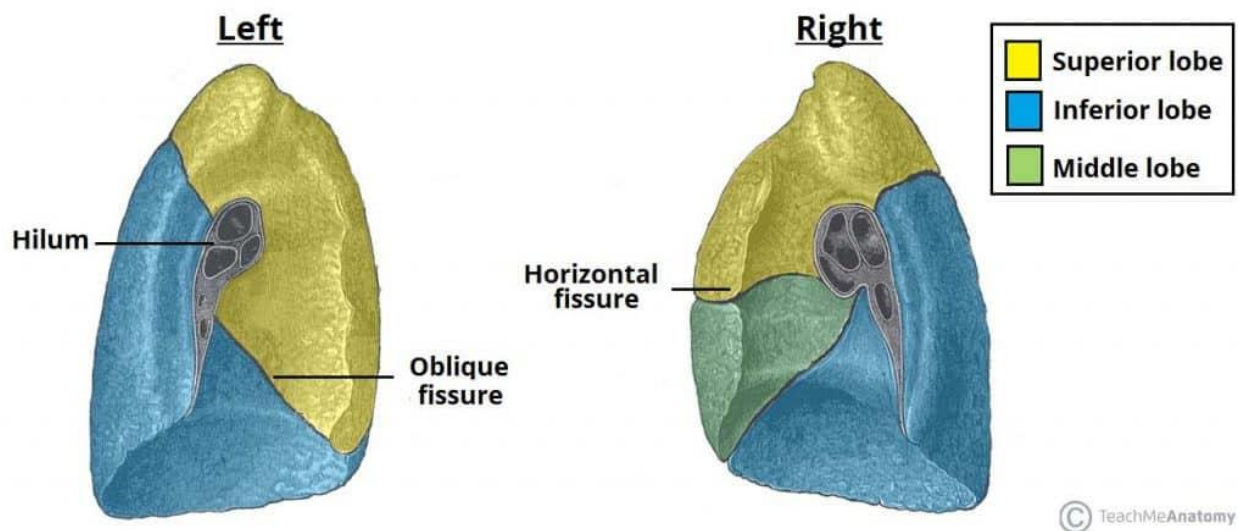
Figure 1.7: Sagittal views looking from the midline of the body of the left and right lungs, with typical lobe and fissure structure highlighted. Reproduced from the following website:

https://teachmeanatomy.info/thorax/organs/lungs/

The volume of the thoracic cavity is increased to trigger inspiration, and decreased to trigger expiration. During quiet respiration, the volume of the thoracic cavity is primarily modulated by the diaphragm, a dome-shaped sheet of muscle surrounding a central tendon located at the base of the thoracic cavity. When the diaphragm contracts, the dome of the diaphragm flattens and descends within the thorax, increasing the volume of the thoracic cavity and drawing air into the lungs. When the diaphragm relaxes, the dome becomes rounded again, decreasing the volume of the thoracic cavity and pushing out air from the lungs.

Motion of the lungs during respiration is nonlinear both in space and in time. The amplitude of motion is generally higher in the inferior regions of the lungs, which lie in close proximity to the diaphragm, than in the superior regions. Significant discontinuities can be observed at lobar fissures, at which the adjacent lung lobes may exhibit sliding behavior (17). Lung deformation during the breathing cycle also exhibits significant hysteresis, as a higher magnitude of pressure is required to increase lung volume than to decrease it (18,19).

1.3.2. Airway anatomy and gas exchange in the lungs

The tracheobronchial tree is a branching network of airways that transports air between the interior of the body and the surroundings (Fig. 1.8). The trachea divides into left and right main bronchi, which each divide into lobar bronchi. The lobar bronchi divide into segmental bronchi, and these divide into conducting bronchioles. Progressive subdivisions of the conducting bronchioles continue for approximately 16 branching generations after the segmental bronchi. The last generation of conducting bronchioles, called the terminal bronchioles, further branches into several generations of respiratory bronchioles. Each respiratory bronchiole divides into several alveolar ducts, which are each made up of several alveoli, thin-walled pouches that lie at the end of the branched respiratory bronchioles.
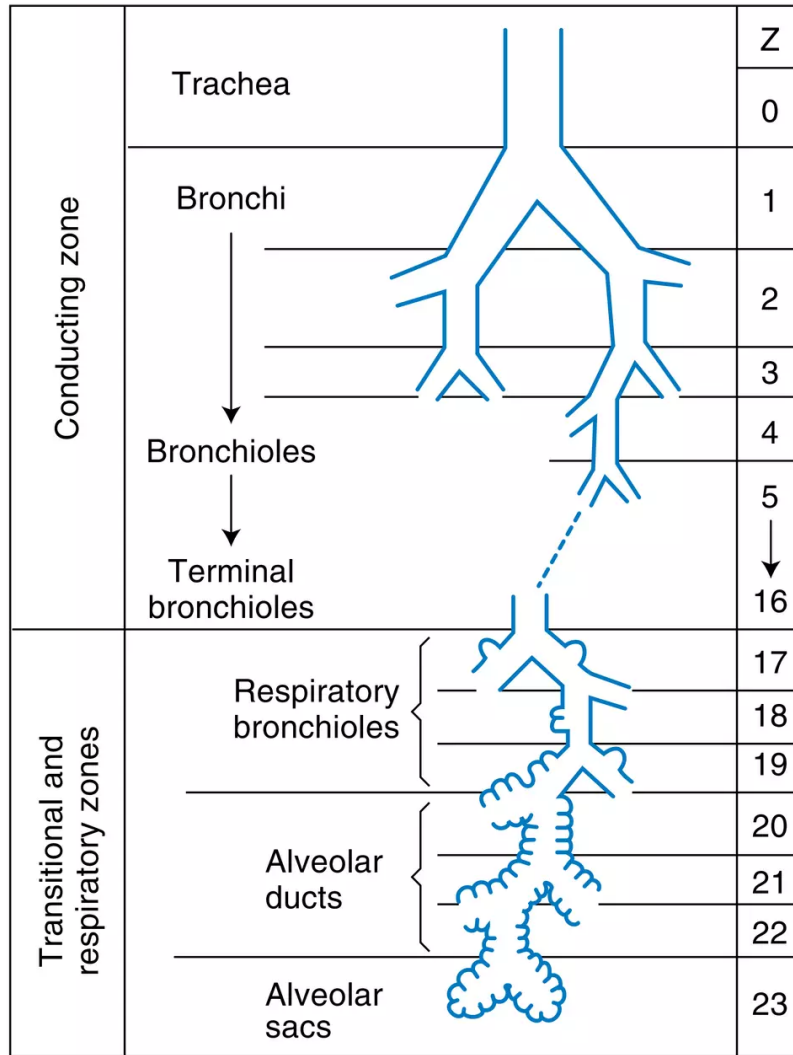
Figure 1.8: Diagram of the branching structure of the airways. Reproduced from West and Luks (20).

The pulmonary vasculature follows a similar pattern of branching to that of the airways, with each alveolus located in close proximity to several pulmonary capillaries. Gas exchange between the airways and the blood occurs at the alveoli via passive diffusion across the blood-air barrier between the alveoli and the capillaries, which is extremely thin (~0.2-2 μm in healthy individuals). During normal respiration, the partial pressure of oxygen is higher in inspired airthan in the pulmonary capillaries, and the partial pressure of carbon dioxide is higher in the capillaries than in inspired air. Pressure gradients drive oxygen across the alveolar membrane and into the blood, and carbon dioxide across the membrane and into the alveolar airspaces. The highly branched structure of the airways creates a large alveolar surface area over which gas exchange can occur (~100 m^2 in a typical healthy adult).

Various pulmonary pathologies impede the pulmonary gas exchange process. Emphysema is characterized by destruction and enlargement of alveoli that results in decreased alveolar surface area available for gas exchange. Fibrotic disorders such as idiopathic pulmonary fibrosis feature scarring and tissue buildup in the alveolar membrane that increases resistance of the membrane to passive gas diffusion. Acute respiratory distress syndrome is characterized by fluid buildup in the alveoli due to increased fluid permeability of the alveolar membrane, resulting in impaired gas exchange.

1.4. Lung MRI challenges and existing techniques

1.4.1. Proton MRI

The lung is a uniquely challenging environment for traditional ^{1}H MRI. The water density of functional tissue in the lung sits below 25%, far lower than in most other tissues in the body (21,22). Additionally, the high prevalence of air-tissue interfaces in the lung results in a T_2* of approximately 1-2 ms at 1.5 T, far lower than most other tissues in the body. Finally, the motion of the lungs during breathing and of the heart during the cardiac cycle threatens to induce significant motion artifacts in lung MR images. These issues have led to a nearly universal preference in the clinic for computed tomography (CT) imaging of the lung over lung MRI. However, the high radiation exposure inherent in CT imaging has motivated the development of lung MRI techniques that address one or more of the above issues.

Pulse sequences that utilize brief, non-selective RF pulses and minimal delays between RF excitation and readout of the k-space center can be used to maximize the acquired MR signal in the lungs, mitigating the low signal level and short T_2* by performing the readout of the k-space center prior to significant decay and/or dephasing of the transverse magnetization following excitation. For each readout, gradients are then used to trace spoke-radial lines to the k-space periphery, filling in the remainder of the k-space matrix. This approach, called ultrashort echo time (UTE) MRI, has been demonstrated using both spoiled UTE (23–26) and steady-state UTE approaches (22,27) for MRI of the lung, and has the added advantage of minimizing streaking artifacts due to motion as a result of the frequent sampling of low-frequency k-space regions (28,29).

Motion of the lungs during breathing can be managed by acquiring imaging data only during a single phase of the breathing cycle. This can be accomplished by imaging during a single breath-hold, or by using a prospective navigator (Fig. 1.9) to trigger image acquisition segments at a specific point in the breathing cycle during free breathing (22). While these approaches can produce useful results, the required speed of single-breath-hold imaging can necessitate significant compromises on image resolution, signal-to-noise ratio, and sampling density, while prospective triggering results in low sampling efficiency per time and therefore undesirably high scan times.
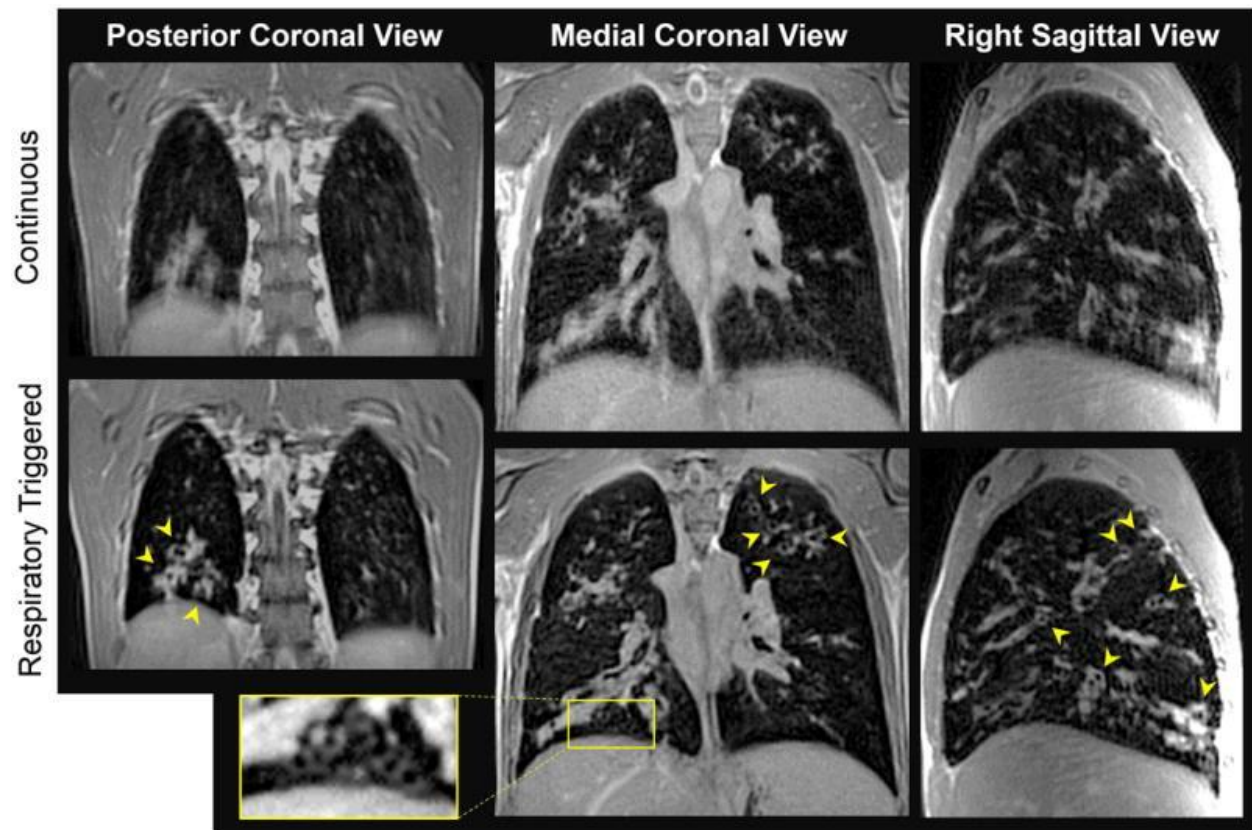
Figure 1.9: Coronal views from 3D ultra-short echo time proton lung MRI performed in an individual with cystic fibrosis, using a free-breathing acquisition with no motion compensation (top row) and a respiratory-triggered free breathing acquisition with acquisition segments triggered at end-of-exhalation (bottom row). Blurring due to motion apparent in free-breathing images is eliminated in the respiratory-triggered images. Yellow arrows indicate thickened airways characteristic of cystic fibrosis. Reproduced from Miller *et al (22)*.

An alternative approach to prospective motion management is the use of postprocessing techniques designed to alleviate motion and/or under-sampling artifacts in data collected during

free breathing (30). Commonly, these techniques use a retrospective navigator derived from the free-breathing image data to sort data into motion states, and then employ compressed sensing reconstruction algorithms to produce artifact-free images with high signal-to-noise ratio. These compressed sensing algorithms may include one or more regularizer terms that enforce minimization of differences between adjacent temporal pseudo-frames (26,31,32). Alternatively, highly under-sampled temporal frames can be maintained in their original temporal order and reconstructed using the aforementioned compressed sensing approaches, minimizing differences across actual temporal frames rather than motion-sorted pseudo-temporal frames (33–36). These reconstruction algorithms require significant computing power and time, but offer the important advantage of permitting constant data collection during free breathing.

1.4.2. Hyperpolarized gas MRI

MRI of hyperpolarized gas (HPG) is an alternative complement to proton lung MRI that permits assessment of various aspects of pulmonary structure and function (37–39). HPG MRI is performed using a radiofrequency coil tuned to the Larmor frequency of the gas of interest (either ^{3}He or ^{129}Xe), following inhalation of a prepared dose of the gas by the individual being imaged. Pulse sequences and reconstruction approaches similar to those used in anatomical proton MRI yield images of inhaled HPG in the lungs. The resulting images permit visualization of non-ventilated lung regions and region-resolved quantification of ventilation distribution (Fig. 1.10), and can be used to characterize burden of obstructive lung diseases such as asthma and chronic obstructive pulmonary disease (40–42).
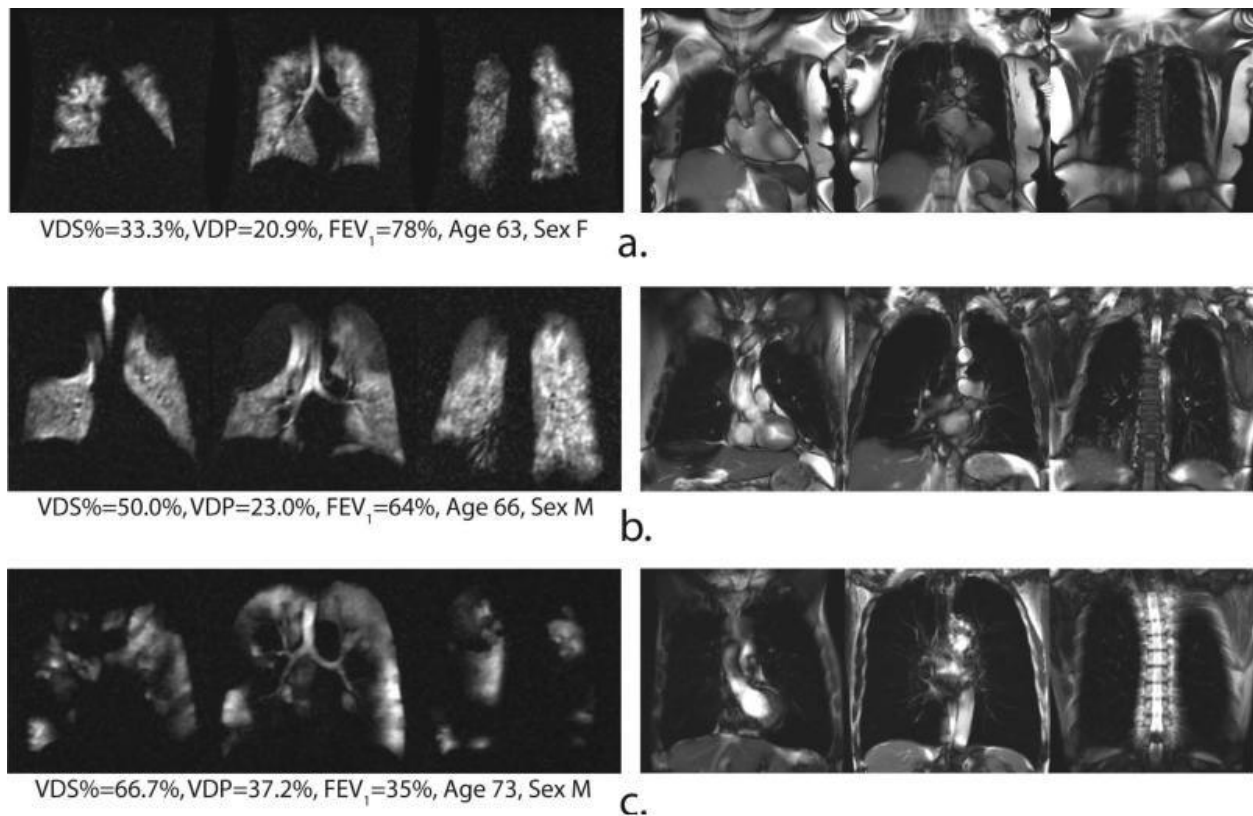
Figure 1.10: 2D coronal slices from hyperpolarized xenon-129 ventilation MRI (left) and proton anatomical images in three individuals with COPD. Regions of impaired ventilation, indicated by lack of xenon-129 signal in lung regions, are evident in all three individuals. Reproduced from Virgincar *et al (42)*.

HPG MRI can also be used to directly quantify motion of the lungs during the breathing cycle by performing grid-tagged excitation of the inhaled HPG at end-of-inspiration breath-hold and imaging the tagged HPG during expiration (43,44), as shown in Fig. 1.11. HPG tagging MRI has been demonstrated for two-phase 3D imaging (43) and multi-phase 2D imaging (45) during expiration and has been used to generate maps of lung kinematic quantities in healthy individuals and those with asthma and pulmonary fibrosis (46). This method is of interest for characterizing biomechanical differences between healthy and diseased individuals, as well as for validating 4D deformable image registration (DIR) models of lung deformation during breathing used to guide radiation therapy of thoracic tumors (47).
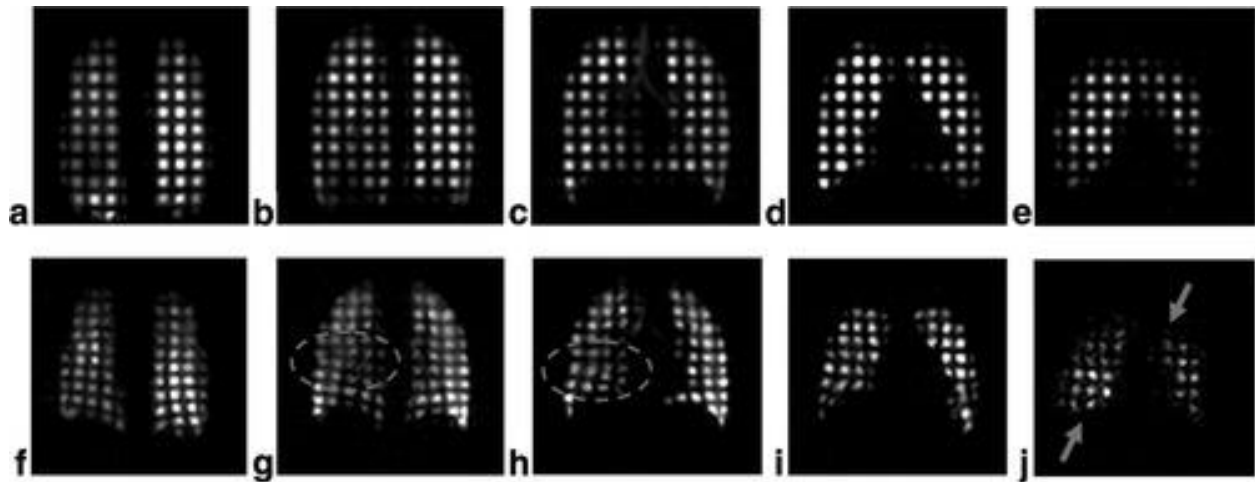
Figure 1.11: 2D coronal slices from hyperpolarized helium-3 tagging MRI in a healthy individual at **a-e)** end-of-inhalation and **f-j)** end-of-exhalation. Irregular motion is detected near a fissure in the right lung (dashed circle), and signal was lost in some peripheral regions due to motion of the lung tissue and helium-3 out of the imaging slice (arrows). Reproduced from Cai *et al (44)*.

The alveolar gas exchange process can also be visualized and quantified using HPG MRI (Fig. 1.12). ^{129}Xe, one of the two noble gas isotopes commonly used for HPG MRI, is soluble in alveolar tissue and binds to hemoglobin in red blood cells, following an uptake pathway akin to that of inhaled oxygen (48,49). ^{129}Xe displays distinct spectral peaks as a free gas, dissolved in alveolar tissue and blood plasma, and bound to hemoglobin (50). Spectroscopic MR techniques can therefore be used to quantify gas-exchange efficacy between alveoli and pulmonary capillaries, and readouts derived from these techniques display sensitivity to changes to the lung microstructure associated with fibrotic and other pulmonary disorders (51–55).
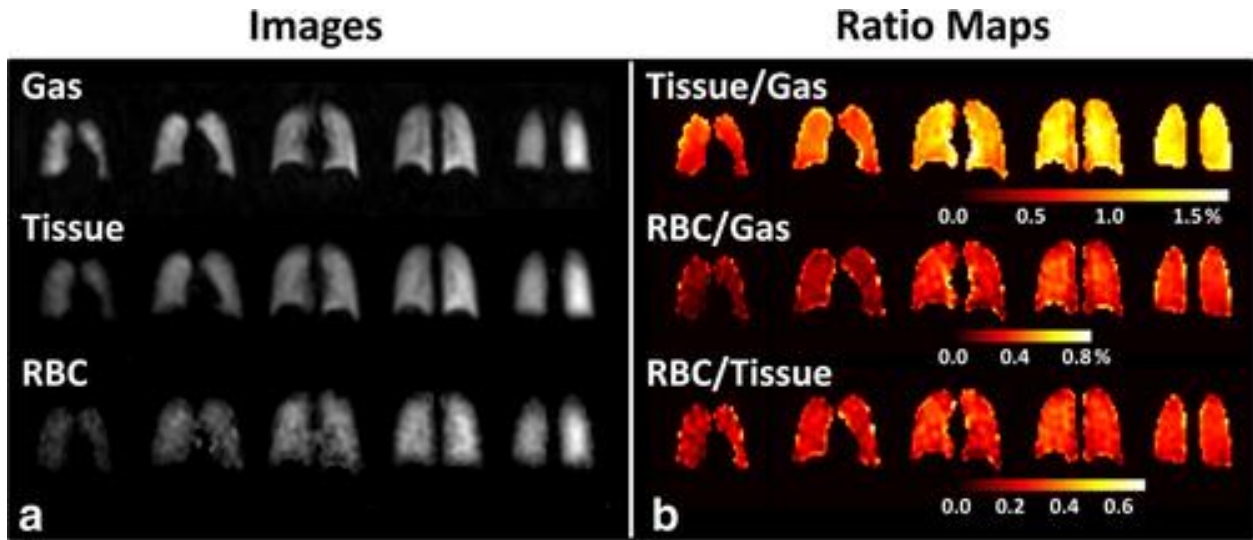
Figure 1.12: Coronal gas, tissue, and RBC images (left), as well as corresponding tissue/gas, RBC/gas, and RBC/tissue maps (right) from a healthy individual. Reproduced from Qing *et al (55)*.

1.5. Scope of the dissertation

This dissertation will describe technical advances and considerations relevant to various types of lung MRI. The specific aims of the dissertation are [1] to develop and demonstrate a method for performing 3D multi-phase hyperpolarized-gas tagging MRI of the lung during a single breathing maneuver; [2] to characterize repeatability and lung volume dependence of 3D dissolved-phase ^{129}Xe MRI of the lung in both health and smoking-related disease; and [3] to develop and demonstrate a method for performing 4D ultrashort echo time (UTE) balanced steady-state free precession (bSSFP) MRI of the lung during free breathing.

Chapter 2 presents a compressed-sensing based method to accelerate acquisition of 3D HPG tagging MR images (Aim 1), permitting collection of several 3D image frames within one breathing maneuver and thus facilitating more complete characterization of pulmonary biomechanics from HPG tagging MRI. This method takes advantage of the distinct and predictable distribution of k-space energy in the HPG tagging context in order to under-sample *k*-space heavily during image acquisition without sacrificing image quality. 3D multi-frame tagging MR image sets were collected in a small number of healthy subjects and used to generate time-resolved displacement, strain, and volumetric change maps for a single exhalation in each subject.

Chapter 3 presents a comprehensive study of the effect of lung volume differences on gas-uptake metrics derived from dissolved-phase ^{129}Xe MRI, in healthy individuals and in COPD patients, both within and across individuals (Aim 2). This study follows preliminary work suggesting that these metrics are sensitive to lung volume during measurement (56,57). The study comprehensively characterizes the effects of lung volume on gas-uptake metrics, compares and contrasts the observed lung volume dependence with models of similar quantitative imaging readouts of lung function in the literature, and assesses the effect of scan-to-scan lung volume differences on gas-uptake metrics derived from repeated measurements within individuals.

Chapter 4 presents a combined 4D UTE bSSFP spoke-radial pulse sequence with a GRASP-Pro-based reconstruction algorithm for high-resolution, high-signal, respiratory-phase-resolved MRI of the lung (Aim 3). This approach takes advantage of the high signal (even for short TR) inherent in bSSFP techniques and the natural sparsity of the sorted respiratory phase-binned image series in the respiratory-phase domain. Images collected using this sequence and reconstruction method are compared with images collected using a 4D UTE spoiled spoke-radial sequence, as well as respiratory-triggered 3D images collected using the UTE bSSFP readout.

1.6. References

1. Brown RW, Cheng YCN, Haacke EM, Thompson MR, Venkatesan R. Magnetic Resonance Imaging: Physical Principles and Sequence Design. 2nd ed. John Wiley & Sons, Incorporated; 2014. 1161 p.

2. Walker TG, Happer W. Spin-exchange optical pumping of noble-gas nuclei. Rev Mod Phys. 1997 Apr 1;69(2):629–42.

3. Mooney KE, Miller GW, Dolph PAM, Tobias WA, Nelyubin V, Singh J, et al. A 3-Liter Capacity, Hybrid Spin-Exchange 3He Polarizer for Medical Imaging. In: Proceedings of the 17th Annual Meeting of the International Society for Magnetic Resonance in Medicine. Honolulu, HI; 2009.

4. Hersman FW, Ruset IC, Ketel S, Muradian I, Covrig SD, Distelbrink J, et al. Large Production System for Hyperpolarized 129Xe for Human Lung Imaging Studies. Academic Radiology. 2008 Jun 1;15(6):683–92.

5. Block KT, Uecker M, Frahm J. Undersampled radial MRI with multiple coils. Iterative image reconstruction using a total variation constraint. Magnetic Resonance in Medicine. 2007;57(6):1086–98.

6. Lustig M, Donoho DL, Santos JM, Pauly JM. Compressed Sensing MRI. IEEE Signal Processing Magazine. 2008 Mar;25(2):72–82.

7. Lustig M, Donoho D, Pauly JM. Sparse MRI: The application of compressed sensing for rapid MR imaging. Magnetic Resonance in Medicine. 2007;58(6):1182–95.

8. Starck JL, Elad M, Donoho DL. Image decomposition via the combination of sparse representations and a variational approach. IEEE Trans Image Process. 2005 Oct;14(10):1570–82.

9. Lustig M, Santos JM, Donoho DL, Pauly JM. k-T SPARSE: High Frame Rate Dynamic MRI Exploiting Spatio-Temporal Sparsity.

10. Feng L, Srichai MB, Lim RP, Harrison A, King W, Adluru G, et al. Highly accelerated real-time cardiac cine MRI using k-t SPARSE-SENSE. Magn Reson Med. 2013 Jul;70(1):64–74.

11. Fletcher R, Reeves CM. Function minimization by conjugate gradients. The Computer Journal. 1964 Jan 1;7(2):149–54.

12. Dai YH, Yuan Y. A Nonlinear Conjugate Gradient Method with a Strong Global Convergence Property. SIAM J Optim. 1999 Jan;10(1):177–82.

13. Boyd S. Distributed Optimization and Statistical Learning via the Alternating Direction Method of Multipliers. FNT in Machine Learning. 2010;3(1):1–122.

14. Armijo L. Minimization of functions having Lipschitz continuous first partial derivatives. Pacific Journal of Mathematics. 1966 Jan;16(1):1–3.

15. Raasch BN, Carsky EW, Lane EJ, O'Callaghan JP, Heitzman ER. Radiographic anatomy of the interlobar fissures: a study of 100 specimens. AJR Am J Roentgenol. 1982 Jun;138(6):1043–9.

16. West CT, Slim N, Steele D, Chowdhury A, Brassett C. Are textbook lungs really normal? A cadaveric study on the anatomical and clinical importance of variations in the major lung fissures, and the incomplete right horizontal fissure. Clinical Anatomy. 2021;34(3):387–96.

17. Amelon RE, Cao K, Reinhardt JM, Christensen GE, Raghavan ML. A measure for characterizing sliding on lung boundaries. Ann Biomed Eng. 2014 Mar;42(3):642–50.

18. Brusasco V, Pellegrino R. Hysteresis of airways and lung parenchyma. Respiratory Medicine. 1995 May 1;89(5):317–22.

19. White B, Zhao T, Lamb J, Wuenschel S, Bradley J, El Naqa I, et al. Distribution of lung tissue hysteresis during free breathing. Med Phys. 2013 Apr;40(4):043501.

20. West JB, Luks AM. West's Respiratory Physiology: The Essentials. 10th ed. Philadelphia, PA: Wolters Kluwer; 2016. 238 p.

21. Theilmann RJ, Arai TJ, Samiee A, Dubowitz DJ, Hopkins SR, Buxton RB, et al. Quantitative MRI measurement of lung density must account for the change in T with lung inflation. Journal of Magnetic Resonance Imaging. 2009;30(3):527–34.

22. Miller GW, Mugler III JP, Sá RC, Altes TA, Prisk GK, Hopkins SR. Advances in functional and structural imaging of the human lung using proton MRI. NMR in Biomedicine. 2014;27(12):1542–56.

23. Higano NS, Hahn AD, Tkach JA, Cao X, Walkup LL, Thomen RP, et al. Retrospective respiratory self-gating and removal of bulk motion in pulmonary UTE MRI of neonates and adults. Magn Reson Med. 2017 Mar;77(3):1284–95.

24. Delacoste J, Chaptinel J, Beigelman-Aubry C, Piccini D, Sauty A, Stuber M. A double echo ultra short echo time (UTE) acquisition for respiratory motion-suppressed high resolution imaging of the lung. Magn Reson Med. 2018 Apr;79(4):2297–305.

25. Bae K, Jeon KN, Hwang MJ, Lee JS, Ha JY, Ryu KH, et al. Comparison of lung imaging using three-dimensional ultrashort echo time and zero echo time sequences: preliminary study. Eur Radiol. 2019 May 1;29(5):2253–62.

26. Zhu X, Chan M, Lustig M, Johnson K, Larson P. Iterative Motion Compensation reconstruction ultra-short TE(iMoCo UTE) for high resolution free breathing pulmonary MRI. Magn Reson Med. 2020 Apr;83(4):1208–21.

27. Bauman G, Bieri O. Balanced steady-state free precession thoracic imaging with half-radial dual-echo readout on smoothly interleaved archimedean spirals. Magnetic Resonance in Medicine. 2020;84(1):237–46.

28. Bergin CJ, Pauly JM, Macovski A. Lung parenchyma: projection reconstruction MR imaging. Radiology. 1991 Jun;179(3):777–81.

29. Glover GH, Pauly JM. Projection Reconstruction Techniques for Reduction of Motion Effects in MRI. Magnetic Resonance in Medicine. 1992;28(2):275–89.

30. Feng L, Benkert T, Block KT, Sodickson DK, Otazo R, Chandarana H. Compressed sensing for body MRI. Journal of Magnetic Resonance Imaging. 2017;45(4):966–87.

31. Feng L, Axel L, Chandarana H, Block KT, Sodickson DK, Otazo R. XD-GRASP: Golden-angle radial MRI with reconstruction of extra motion-state dimensions using compressed sensing. Magnetic Resonance in Medicine. 2016;75(2):775–88.

32. Rank CM, Heußer T, Buzan MTA, Wetscherek A, Freitag MT, Dinkel J, et al. 4D respiratory motion-compensated image reconstruction of free-breathing radial MR data with very high undersampling. Magnetic Resonance in Medicine. 2017;77(3):1170–83.

33. Chen L, Liu D, Zhang J, Xie B, Zhou X, Grimm R, et al. Free-Breathing Dynamic Contrast-Enhanced MRI for Assessment of Pulmonary Lesions Using Golden-Angle Radial Sparse Parallel Imaging. J Magn Reson Imaging. 2018 Aug;48(2):459–68.

34. Ong F, Zhu X, Cheng JY, Johnson KM, Larson PEZ, Vasanawala SS, et al. Extreme MRI: Large-scale volumetric dynamic imaging from continuous non-gated acquisitions. Magn Reson Med. 2020 Oct;84(4):1763–80.

35. Miller Z, Torres L, Fain S, Johnson K. Motion Compensated Extreme MRI: Multi-Scale Low Rank Reconstructions for Highly Accelerated 3D Dynamic Acquisitions (MoCo-MSLR) [Internet]. arXiv; 2022 [cited 2023 Aug 31]. Available from: http://arxiv.org/abs/2205.00131

36. Feng L, Liu F. High spatiotemporal resolution motion-resolved MRI using XD-GRASP-Pro. In: Proc Intl Soc Mag Reson Med 28. 2020. p. 597.

37. Roos JE, McAdams HP, Kaushik SS, Driehuys B. Hyperpolarized Gas MRI: Technique and Applications. Magn Reson Imaging Clin N Am. 2015 May;23(2):217–29.

38. Mugler JP, Altes TA. Hyperpolarized 129Xe MRI of the human lung. J Magn Reson Imaging. 2013 Feb;37(2):313–31.

39. Niedbalski PJ, Hall CS, Castro M, Eddy RL, Rayment JH, Svenningsen S, et al. Protocols for multi-site trials using hyperpolarized 129Xe MRI for imaging of ventilation, alveolar-airspace size, and gas exchange: A position paper from the 129Xe MRI clinical trials consortium. Magnetic Resonance in Medicine. 2021;86(6):2966–86.

40. Altes TA, Powers PL, Knight-Scott J, Rakes G, Platts-Mills TAE, de Lange EE, et al. Hyperpolarized 3He MR lung ventilation imaging in asthmatics: Preliminary findings. Journal of Magnetic Resonance Imaging. 2001;13(3):378–84.

41. He M, Driehuys B, Que LG, Huang YCT. Using Hyperpolarized 129Xe MRI to Quantify the Pulmonary Ventilation Distribution. Academic Radiology. 2016 Dec 1;23(12):1521–31.

42. Virgincar RS, Cleveland ZI, Kaushik SS, Freeman MS, Nouls J, Cofer GP, et al. Quantitative analysis of hyperpolarized 129Xe ventilation imaging in healthy volunteers and subjects with chronic obstructive pulmonary disease. NMR Biomed. 2013 Apr;26(4):424–35.

43. Cai J, Miller GW, Altes TA, Read PW, Benedict SH, de Lange EE, et al. Direct measurement of lung motion using hyperpolarized helium-3 MR tagging. Int J Radiat Oncol Biol Phys. 2007 Jul 1;68(3):650–3.

44. Cai J, Altes TA, Miller GW, Sheng K, Read PW, Mata JF, et al. MR grid-tagging using hyperpolarized helium-3 for regional quantitative assessment of pulmonary biomechanics and ventilation. Magn Reson Med. 2007 Aug;58(2):373–80.

45. Cai J, Sheng K, Benedict SH, Read PW, Larner JM, Mugler JP, et al. Dynamic MRI of grid-tagged hyperpolarized helium-3 for the assessment of lung motion during breathing. Int J Radiat Oncol Biol Phys. 2009 Sep 1;75(1):276–84.

46.   Tustison NJ, Awate SP, Cai J, Altes TA, Miller GW, de Lange EE, et al. Pulmonary kinematics from tagged hyperpolarized helium-3 MRI. J Magn Reson Imaging. 2010 May;31(5):1236–41.

47.   Cui T, Miller GW, Mugler JP, Cates GD, Mata JF, de Lange EE, et al. An initial investigation of hyperpolarized gas tagging magnetic resonance imaging in evaluating deformable image registration-based lung ventilation. Med Phys. 2018 Dec;45(12):5535–42.

48.   Martin CC, Williams RF, Gao JH, Nickerson LDH, Xiong J, Fox PT. The pharmacokinetics of hyperpolarized xenon: Implications for cerebral MRI. Journal of Magnetic Resonance Imaging. 1997;7(5):848–54.

49.   Peled S, Jolesz FA, Tseng CH, Nascimben L, Albert MS, Walsworth RL. Determinants of tissue delivery for 129Xe magnetic resonance in humans. Magnetic Resonance in Medicine. 1996;36(3):340–4.

50.   Miller KW, Reo NV, Schoot Uiterkamp AJ, Stengle DP, Stengle TR, Williamson KL. Xenon NMR: chemical shifts of a general anesthetic in common solvents, proteins, and membranes. Proceedings of the National Academy of Sciences. 1981 Aug;78(8):4946–9.

51.   Cleveland ZI, Cofer GP, Metz G, Beaver D, Nouls J, Kaushik SS, et al. Hyperpolarized 129Xe MR Imaging of Alveolar Gas Uptake in Humans. PLOS ONE. 2010 Aug 16;5(8):e12192.

52.   Mugler JP, Altes TA, Ruset IC, Dregely IM, Mata JF, Miller GW, et al. Simultaneous magnetic resonance imaging of ventilation distribution and gas uptake in the human lung using hyperpolarized xenon-129. Proceedings of the National Academy of Sciences. 2010 Dec 14;107(50):21707–12.

53.   Wang JM, Robertson SH, Wang Z, He M, Virgincar RS, Schrank GM, et al. Using hyperpolarized 129Xe MRI to quantify regional gas transfer in idiopathic pulmonary fibrosis. Thorax. 2018 Jan 1;73(1):21–8.

54.   Weatherley ND, Stewart NJ, Chan HF, Austin M, Smith LJ, Collier G, et al. Hyperpolarised xenon magnetic resonance spectroscopy for the longitudinal assessment of changes in gas diffusion in IPF. Thorax. 2019 May 1;74(5):500–2.

55.   Qing K, Ruppert K, Jiang Y, Mata JF, Miller GW, Shim YM, et al. Regional mapping of gas uptake by blood and tissue in the human lung using hyperpolarized xenon-129 MRI. Journal of Magnetic Resonance Imaging. 2014;39(2):346–59.

56.   Inati SJ, Hansen MS, Kellman P. A fast optimal method for coil sensitivity estimation and adaptive coil combination for complex images. In: Proc Intl Soc Mag Reson Med 22. 2014. p. 4407.

57.   Hahn AD, Kammerman J, Evans M, Zha W, Cadman RV, Meyer K, et al. Repeatability of regional pulmonary functional metrics of Hyperpolarized 129Xe dissolved-phase MRI. Journal of Magnetic Resonance Imaging. 2019;50(4):1182–90.

Chapter 2: 3D multi-phase hyperpolarized-gas tagging lung MRI

2.1. Introduction

Image-based quantification of lung deformation during the breathing cycle is of potential use for time-resolved and region-resolved characterization of lung biomechanics. Pulmonary compliance, a measure of the lung's tendency to expand and contract in response to changes in intrapleural pressure, is observed to be elevated in emphysema (1) and chronic asthma (2), and lessened in pulmonary fibrosis (3), acute respiratory distress syndrome (4), and pneumococcal pneumonia (5). It has been suggested that image-based characterization of mechanical abnormalities associated with these pulmonary diseases might improve disease diagnosis and, in some cases, predict likelihood of treatment efficacy (6,7).

Hyperpolarized gas (HPG) tagging MRI has been demonstrated as a non-invasive imaging technique for directly assessing lung deformation during the breathing cycle (7–12). This technique is promising as a method for directly measuring volume change during the breathing cycle (a component of pulmonary compliance) on both a global and regional basis, for quantifying other lung biomechanical quantities related to compliance, such as regional strain values, and for visualizing and assessing global and regional biomechanical abnormalities. HPG tagging MRI has also been investigated as a method for validating 4D deformable image registration (DIR) models of lung motion during the breathing cycle that are used to guide 4D radiation therapy for lung tumors (11).

To date, this technique has been limited by constraints on imaging time imposed by depolarization of the gas in vivo ($T_1 \approx 20$ s), diffusion and dissolution of the tag elements, and the finite amount of time over which a normal exhalation can occur in a human subject (13–17). Due to these limitations, prior HPG tagging MRI has only been used to collect two 3D frames (7,11,12), or several 2D frames (10), within a single exhalation. The purpose of the work presented in this chapter was to develop a compressed-sensing based method to accelerate acquisition of 3D HPG tagging MR images, permitting collection of several 3D image frames within one breathing maneuver and thus facilitating a more complete characterization of

pulmonary biomechanics from HPG tagging MRI. The proposed approach takes advantage of the distinct and predictable distribution of *k*-space energy in the HPG tagging context in order to under-sample *k*-space heavily during image acquisition without sacrificing image quality (18,19).

2.2. Methods

2.2.1. *k*-space layout and corresponding under-sampling approach

Applying tagging radiofrequency (RF) pulses to inhaled hyperpolarized gas results in predictably and sparsely distributed signal intensity, both in image space and in *k*-space. Tag width and center-to-center distance are directly determined by parameters of the tagging pulse sequence, as described in the Appendix, and virtually all image signal is confined to a region defined by the boundary of the lung. The image-space representation of the tagged HPG gas image can therefore be roughly approximated as the convolution of a small rect function (corresponding to an individual tag) with a comb function (corresponding to the tag spacing), multiplied by a large rect function (corresponding to the spatial extent of the lungs as a whole). This approximation can be written as follows:

$$
\begin{aligned}
I(x,y,z) = A \cdot \Pi &\left(\frac{x}{w_{tag,x}}, \frac{y}{w_{tag,y}}, \frac{z}{w_{tag,z}}\right) * III\left(\frac{x}{\Delta x_{tag}}, \frac{y}{\Delta y_{tag}}, \frac{z}{\Delta z_{tag}}\right) \cdot \\
&\Pi\left(\frac{x}{w_{lung,x}}, \frac{y}{w_{lung,y}}, \frac{z}{w_{lung,z}}\right)
\end{aligned}
\tag{2.1}
$$

where I is the image; $w_{tag,x}$, $w_{tag,y}$, and $w_{tag,z}$ are the user-specified tag widths along the *x*-, *y*-, and *z*-axes, respectively; Δx_{tag}, Δy_{tag}, and Δz_{tag} are the user-specified tag spacings along the *x*-, *y*-, and *z*-axes, respectively; $w_{lung,x}$, $w_{lung,y}$, and $w_{lung,z}$ are the approximate size of the ventilated regions of the lungs along the *x*-, *y*-, and *z*-axes, respectively; and A is an arbitrary scale factor.

The corresponding *k*-space data can then be approximated as the Fourier transform of the approximate image, as follows:

$$
\begin{aligned}
\hat{I}(k_x, k_y, k_z) = \hat{A} \cdot &sinc\left(w_{tag,x}k_x, w_{tag,y}k_y, w_{tag,z}k_z\right) \\
&\cdot III\left(\Delta x_{tag}k_x, \Delta y_{tag}k_y, \Delta z_{tag}k_z\right) \\
&* sinc\left(w_{lung,x}k_x, w_{lung,y}k_y, w_{lung,z}k_z\right)
\end{aligned}
\tag{2.2}
$$

This a priori insight into *k*-space energy distribution can be exploited to generate a pseudo-random, variable-density under-sampling pattern that significantly reduces scan time, while still sampling the large majority of signal present in *k*-space. Based on the expected distribution above, the following likelihood function is used to determine whether a given phase-encode line is sampled (Cartesian readout lines are fully sampled along *k*$_x$, the readout direction):

$$p(k_y, k_z) = sinc(w_{tag,y}k_y, w_{tag,z}k_z) \cdot III(\Delta y_{tag}k_y, \Delta z_{tag}k_z)$$
$$* \exp\left(-\frac{k_y^2}{2\sigma_{ky}^2} - \frac{k_z^2}{2\sigma_{kz}^2}\right) \tag{2.3}$$

where σ_{ky} and σ_{kz} are the Gaussian root mean square (RMS) widths of the Gaussian function described by the exponential term along the *k*$_y$- and *k*$_z$-axes, respectively. A Gaussian function was chosen for this part of the sampling likelihood function (rather than a sinc function) in order to maintain relatively even and dense sampling at each *k*-space peak.

The Gaussian RMS widths were the primary floating parameter used to adjust the area under the sampling likelihood function (and thus the total number of collected samples), as the other parameters in the function were dictated by the tag width and spacing. The area under the Gaussian function was modified by changing the RMS widths, rather than the amplitude, in order to ensure that *k*-space peaks near the center of *k*-space were always densely sampled. For this study, these parameters were chosen such that the total number of lines sampled would equal approximately one-seventh of the entire *k*-space matrix.

An example tagging image, *k*-space data corresponding to the image, the sampling likelihood function described above, and an example sampling pattern generated using the sampling likelihood function are depicted in Fig. 2.1.
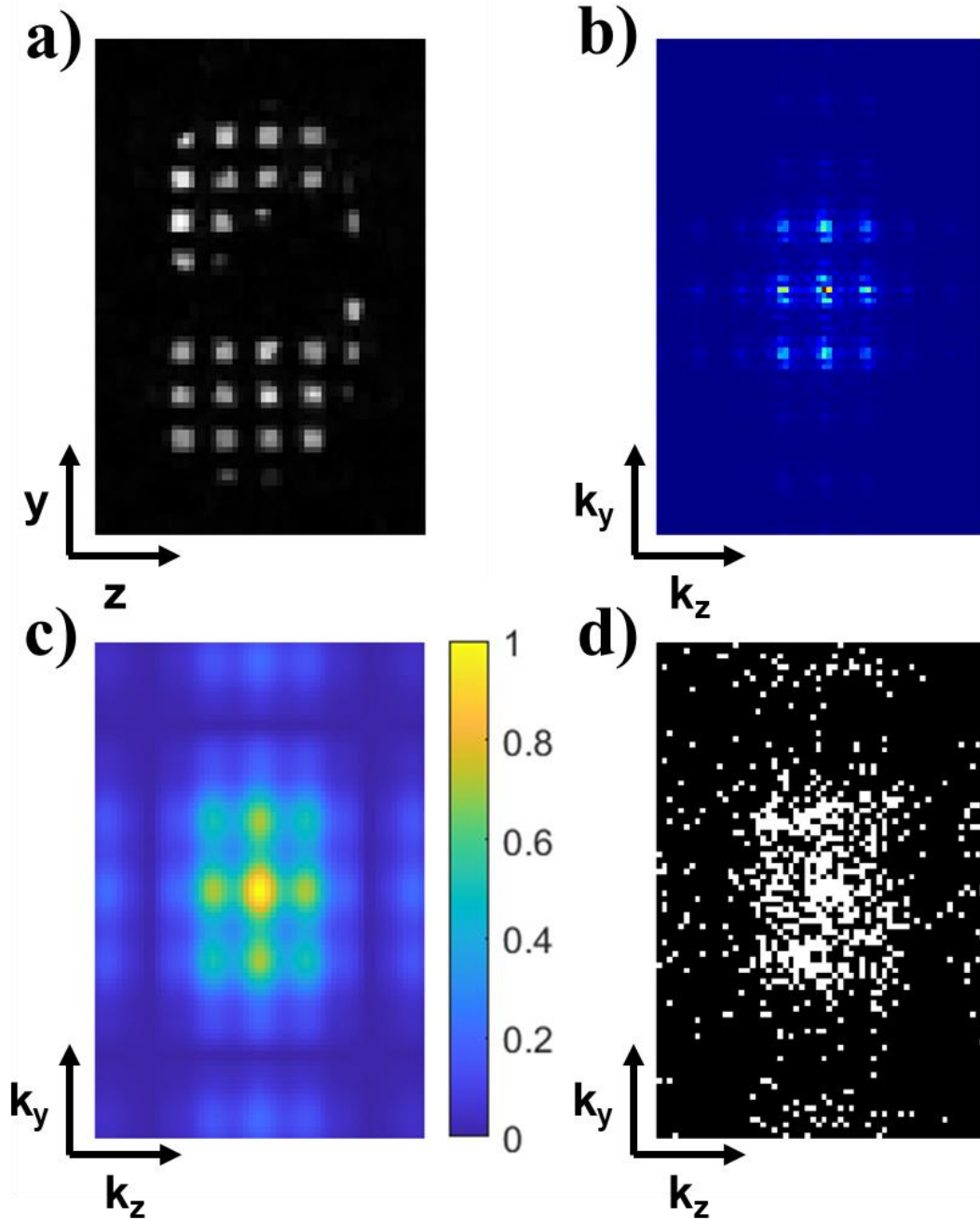
Figure 2.1: **a)** Axial slice taken from a 3D hyperpolarized gas (HPG) tagging image collected in the manner described in this text. **b)** Central 2D plane extracted from 3D k-space data corresponding to the HPG tagging image in a). **c)** Two-dimensional sampling likelihood function described in Eq. 2.3. The color scale corresponds to the likelihood of sampling a given Cartesian line (which is orthogonal to the plane shown) during a particular 3D acquisition. Lines equal to one are always sampled, and lines equal to zero are never sampled. **d)** Example sampling pattern generated using the sampling likelihood function shown in b). In panels b-d), the through-plane direction is the k_x direction, which is fully sampled along each sampled (k_y, k_z) coordinate.

2.2.2. Pulse sequence

Prior to the start of the imaging pulse sequence, 3D square tagging grids were created by applying sinc-modulated RF pulse trains, each followed by a large spoiler gradient consecutively along each of the three principal axes, with a composite flip angle of 90° specified for each pulse train (8,20). The theory of the sinc-modulated RF tagging pulse sequence is described more fully in Appendix 2.5.1. Tag width and center-to-center spacing were 12 and 26 mm, respectively, in each principal direction.

It has been observed previously that the ^{3}He RF coil used in the study did not produce a uniform flip angle across the entire field of view (8,21). The tagging RF pulse train produces incomplete cancellation of magnetization in the tag troughs, and therefore less distinct separation between tags, for flip angles less than the specified 90°. This problem can be prospectively addressed by repeating the tagging RF pulse train, resulting in fuller cancellation of magnetization within the tag troughs (Fig. 2.2). The longitudinal magnetization $M_{\parallel}$ in the tag troughs after N_g repetitions for an effective flip angle θ_{eff} and starting magnetization M_0 is as follows:

$$M_{\parallel} = M_0 \left(\cos \theta_{eff} \right)^{N_g} \tag{2.4}$$

In this work, the tagging pulse train was repeated a total of $N_g = 5$ times along each of the three axes.
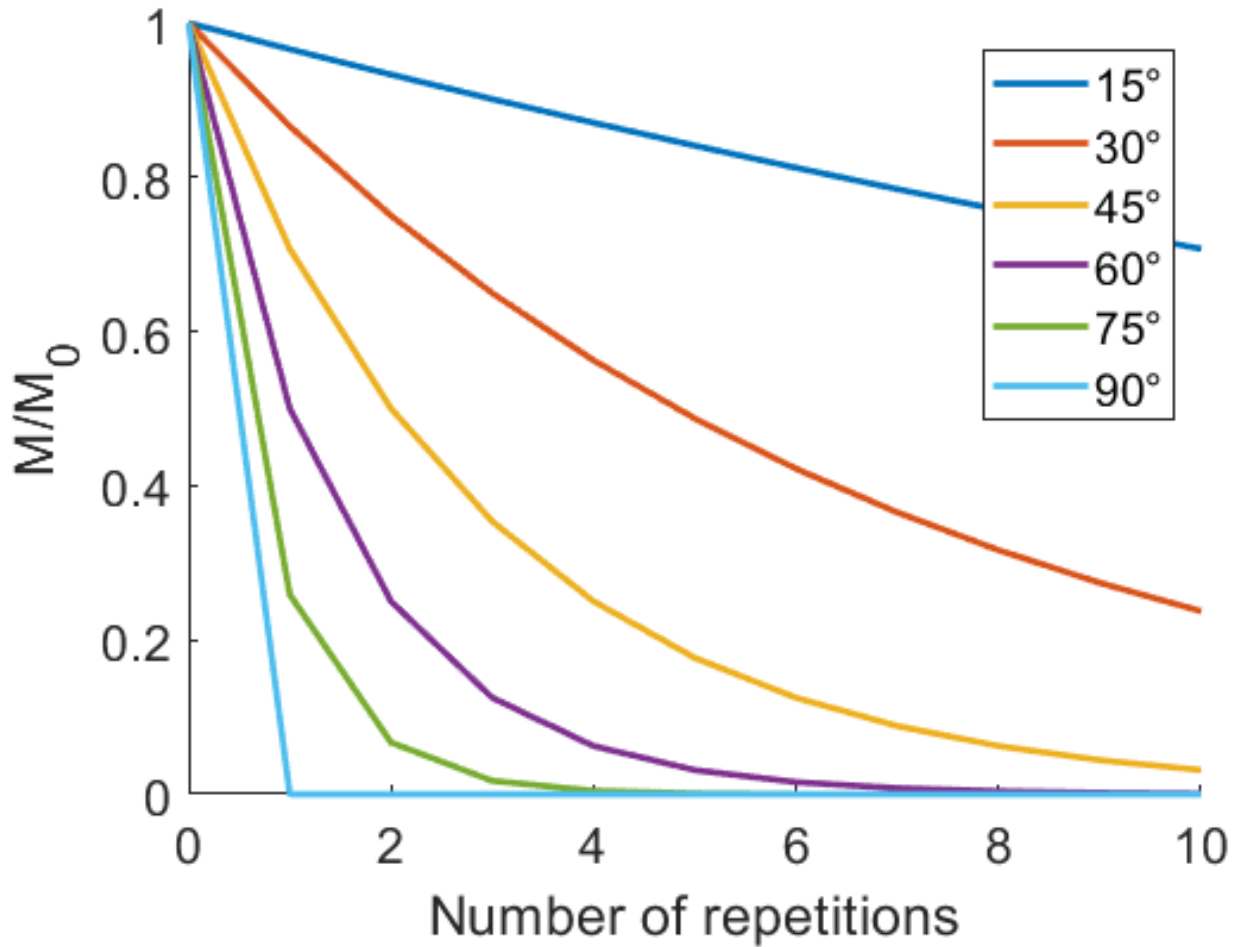
Figure 2.2: Remaining longitudinal magnetization in the tag troughs vs. number of repetitions of the tagging RF pulse train for different effective flip angles.

Imaging was performed using a balanced steady-state free precession (bSSFP) pulse sequence to maximize the limited and transient signal of the inhaled hyperpolarized ^{3}He gas (22). This sequence avoids spoiling transverse magnetization and thus preserves polarization for as long as possible, an important consideration in the HPG tagging context. A 3D Cartesian readout scheme was chosen in light of the Cartesian arrangement of energy peaks in *k*-space described above. Fig. 2.3 depicts the tagging and imaging pulse sequences.
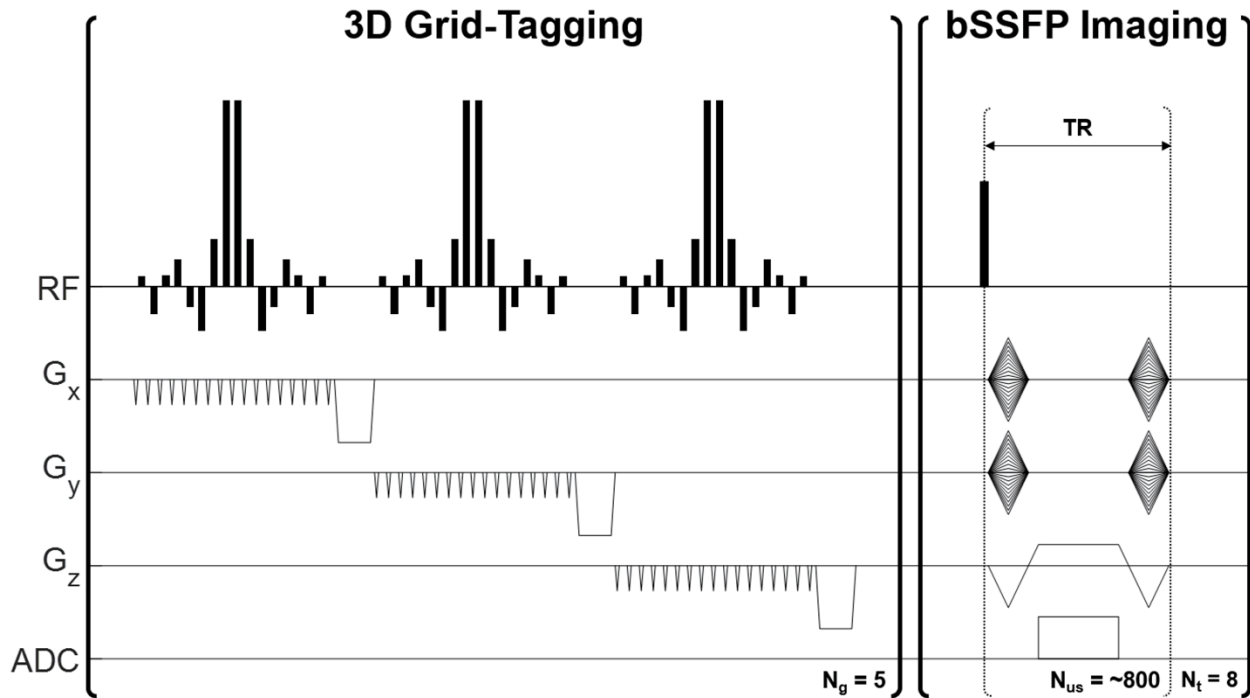
Figure 2.3: Diagram of the pulse sequence used to perform 3D grid tagging and balanced SSFP (bSSFP) imaging. The grid-tagging portion of the sequence was performed $N_g = 5$ times before the start of imaging, to ensure full signal cancellation in the tag troughs. Approximately $N_{us} = 800$ lines per frame were read using the bSSFP readout sequence, and $N_t = 8$ temporal frames were collected per breathing maneuver.

2.2.3. Multi-phase ^{3}He tagging MRI

This study complied with the Health Insurance Portability and Accountability Act and was approved by the University of Virginia Institutional Review Board, and all subjects provided written, informed consent. MRI was performed in three healthy individuals using a 1.5T whole-body scanner (Avanto; Siemens; Erlangen, DE). Subjects were positioned feet-first supine inside the scanner, and standard proton localizer imaging was performed once subjects were positioned to guide selection of a field-of-view that would fully encompass the lungs.

^{3}He gas was polarized via spin-exchange optical pumping to approximately 60% using a home-built system (23–25). For each ^{3}He tagging scan, a Tedlar bag (Jensen Inert Products; Coral Springs, FL) was filled with about 600 ml of hyperpolarized ^{3}He. When ready to begin the ^{3}He tagging scan, subjects were instructed to exhale as far as comfortable. After exhalation, subjects

inhaled the contents of the bag, then additionally inhaled room air to total lung capacity. Following inhalation, subjects were instructed to hold their breath, and 3D tagging grids were created using the tagging pulse sequence described above. Tag width and center-to-center spacing were 12 and 26 mm, respectively, in each principal direction. After creation of the tagging grids, subjects exhaled to residual volume during the imaging procedure. Images were collected at $N_t = 8$ timepoints from end-of-inhalation to end-of-exhalation, using the bSSFP pulse sequence described above. Sequence parameters included: resolution = 3.3 mm isotropic, flip angle = 6°, TR = 1.84 ms, TE = 0.92 ms, readout bandwidth = 1440 Hz/pixel, matrix size = 90 × 112 × 60, time per image = 1.3 s, and total imaging series time = 10.4 s. Subjects were coached to exhale slowly, so that exhalation would begin after the first tagging frame was collected and would last for as close to the total imaging time as possible.

2.2.4. Compressed sensing reconstruction of under-sampled data

Under-sampled images were reconstructed by minimizing the following objective function:

$$\Phi(x) = \|F_u x - y\|_2 + \lambda_1 \|\Psi x\|_1 + \lambda_2 TV(x) \qquad (2.5)$$

where x is the reconstructed image-space image, y is the collected k-space data, F_u is the under-sampled Fourier transform, Ψ is the chosen wavelet transform, TV is the total variation computed via first-order finite differences, and λ_1 and λ_2 are weights that determine the relative importance of the three terms that comprise the objective function (26,27). Nonlinear conjugate gradient with backtracking line search was used as the optimization method (28). The fully-sampled readout direction was taken as the slice direction, and the optimization was performed independently for each 2D slice. A 2D Cohen–Daubechies–Feauveau 9/7 wavelet was used as the sparsifying wavelet transform (29). Weighting coefficient values were $\lambda_1 = 0.003$ and $\lambda_2 = 0.001$.

2.2.5. Displacement map generation from tagged ^{3}He images

To determine tag locations in the first 3D tagged image frame from each subject, a search grid was generated by performing a peak-finding operation on 1D projections of the image data along all three principal dimensions, as shown in Fig. 2.4. The summed signal intensity within the

48

7×7×7 box of voxels centered at each grid point (corresponding to a region slightly smaller than the center-to-center initial tag spacing) was then calculated. The distribution of these intensities was bimodal, characterized by a high, sharp peak centered only slightly above zero (corresponding to boxes without tags) and a low, wide peak centered far from zero (corresponding to boxes with tags). The rightmost edge of the first peak was identified manually and taken to be the threshold indicating tag presence or absence, and boxes with total intensity above this threshold were judged to contain a tag. The centroid of each high-intensity box was then found and taken to be the initial location of each tag.
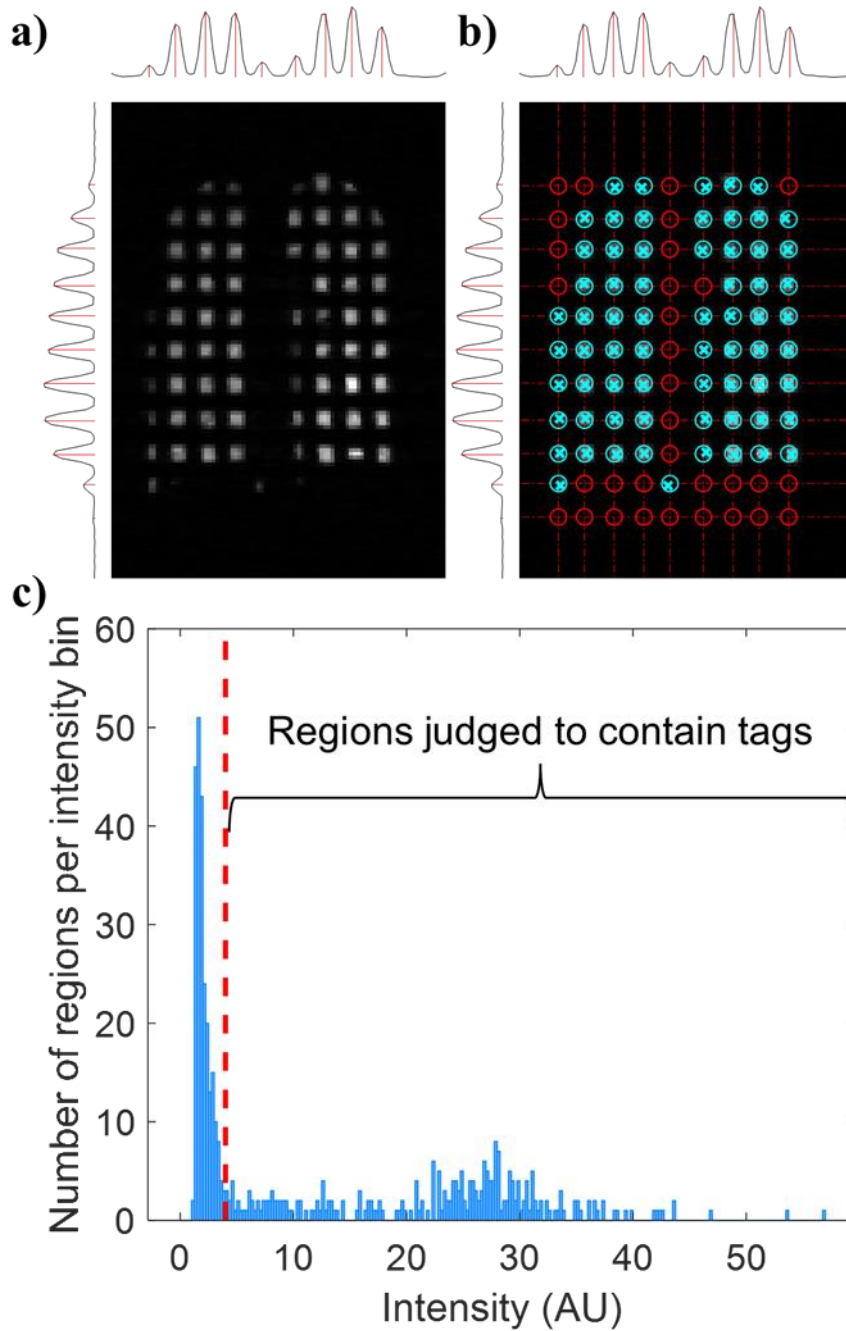
Figure 2.4: **a)** Coronal plane from the first frame of a tagged hyperpolarized gas lung image acquired in Subject 1 using the methods described herein, with 1D projections taken along the two in-plane axes depicted. Red lines indicate locations of peaks of the 1D projections. **b)** Peaks of the 1D projections generated in a) are used to create a grid, and intersection points in the grid are used as initial search points for tags. Locations with sufficient summed intensity to be considered to hold tags are marked with cyan circles, and locations without sufficient intensity are marked with red circles. The centroid of each location holding a tag is then found, and these centroids are taken as the initial tag central locations. Centroids are indicated with cyan crosses. All above-described operations are also

50

performed along the depicted through-plane axis. **c)** Example histogram of intensities at each prospective tag location in the 3D image frame. The rightmost edge of the first peak (corresponding to locations without tags) is identified manually and used as a threshold, with this value indicated by the dashed red line, and all prospective tag locations with summed intensity above this threshold are judged to contain tags.

The following process was then used to identify tag locations in subsequent frames. First, the rectangular cuboid enclosing all of the tags in each frame was found by using a morphological closing operation to fill gaps between tags in each frame, performing a grayscale thresholding operation using Otsu's method (30) to produce binary lung masks, and identifying the smallest rectangular cuboid that would completely enclose each lung mask. These cuboids were then used to produce an approximate bulk motion of the lungs between consecutive frames, by identifying the affine transformation (consisting of a scaling operation and a translation operation) that would warp the cuboid from the earlier frame to that of the later frame, and applying this affine transformation to the tag centroid locations in the earlier frame. The process of producing these cuboids is depicted in Fig. 2.5.
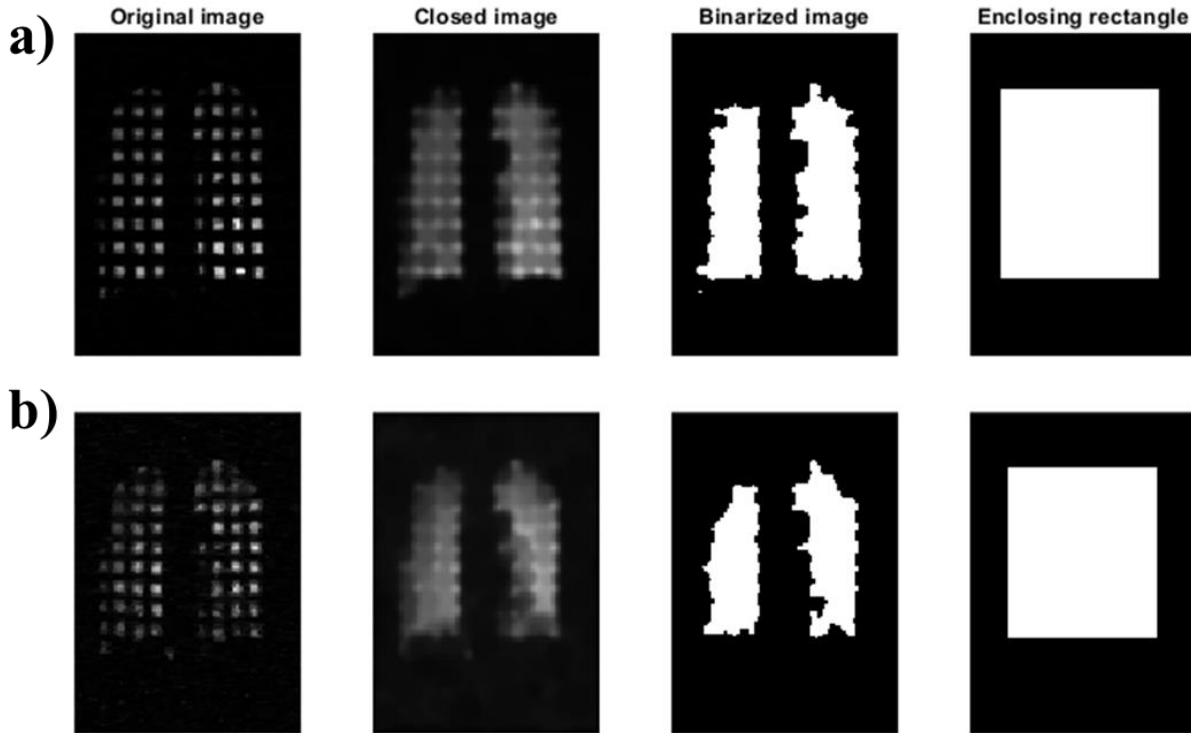
Figure 2.5: Coronal slice from a tagging image (first column from left), the image after performing morphological closing (second column from left), the closed image after binarization (third column from left), and the rectangular cuboid enclosing the binarized image, in **a)** a tagging frame at end-of-inspiration and **b)** a tagging frame at an intermediate point in the breathing cycle from the same scan. Once these rectangular cuboids were identified for each frame, an affine transformation relating the cuboids corresponding to consecutive frames was used to produce starting search locations for each tag in the later frame, by applying the deformation field defined by the affine transformation to each of the tag centroids from the previous frame.

After this operation was complete, the tag centroid locations after affine transformation were used as seeds to search for the true tag locations in the next frame. For each tag, the true location of the centroid was found by identifying the center of mass of the image patch consisting of all voxels that were less than a distance of three voxels away from the associated tag centroid seed produced as described above. The differences in tag locations from one frame to the next were calculated and taken to be the tag displacements between the two frames.

Calculated displacement maps were assessed visually, and occasional manual intervention was applied to rectify visually obvious errors in the tag locations found by the algorithm. Possible interventions included manually specifying tag search locations for one or more tags in a row or column or manually removing tags that had degraded beyond the point of remaining clearly

identifiable in the current and subsequent frames.

2.2.6. Lobar segmentation from tag displacement maps

Lobar segmentation was performed by first manually separating the tag population into left and right lungs, and then performing a two-cluster k-means clustering separately on the tag populations within each lung, using the squared Euclidean distance metric and the k-means++ algorithm for initialization of cluster centers (31,32). The input to the k-means clustering was the set of displacement profiles of each tag from frame to frame, rather than the positions of the tags.

Typically, the left lung consists of an upper and a lower lobe, while the right lung consists of an upper, a middle, and a lower lobe. In the left lung, the lobes are divided by an oblique fissure, while in the right lung, the upper and middle lobes are divided by a horizontal fissure, and the upper/middle and lower lobes are divided by an oblique fissure. Initially, a three-cluster k-means lobar segmentation was attempted for segmentation of the three lobes typically comprising the right lung. However, this segmentation did not produce robust or anatomically plausible segmentations, possibly due to incomplete or nonexistent horizontal fissures in imaged subjects (33). In light of this, a two-cluster segmentation was used in the right lung, similar to that used in the left lung. This segmentation can be understood to divide the right lung at the oblique fissure, separating it into a combined upper/middle "lobe" and a lower lobe.

2.2.7. Strain and fractional volume change calculation from tag displacement maps

Regional normal strains, shear strains, and fractional volume change were calculated from tag displacement fields using a finite element model, using tag centers-of-mass as finite element nodes. Tetrahedral elements were defined throughout the lung using sets of four neighboring nodes (i.e., tags), with the shape of each element at the start of the exhalation maneuver corresponding approximately to a trirectangular tetrahedron. Each node was used as a component of every tetrahedral element to which it could belong, meaning that tetrahedral elements often partially overlapped.

Regional normal strains ε_x, ε_y and ε_z, which represent the fractional change in distance between elements along the left–right axis, anterior–posterior axis and superior–inferior axis, respectively, and shear strains γ_{yz}, γ_{zx} and γ_{xy}, which represent the fractional change in shape of strain elements within the plane normal to the left–right axis, anterior–posterior axis, and the superior–inferior axis, respectively, were computed from each pair of consecutive frames, and over the entire breathing maneuver (i.e., between the first frame and the final frame) for each subject. Details of strain calculation are provided in Appendix 2.5.2.

Fractional volume change with respect to volume at full inspiration was calculated as follows:

$$\Delta V = \frac{V_1 - V_j}{V_1} \tag{2.6}$$

where V_1 is the volume of a given tetrahedral element at full inspiration (during the first frame), and V_j is the volume of the same element at temporal frame j ($2 \leq j \leq N_t$, where N_t is the total number of temporal frames collected during the acquisition). Volumes were calculated using the expression given in Appendix 2.5.2 for volume of an irregular tetrahedron.

Average frame-to-frame strains and fractional volume changes within each segmented lobe were calculated by averaging the strains and fractional volume changes measured within all tetrahedral elements contained entirely within a given lobe, and average strains over the entire lung were calculated by averaging the strains measured within all such elements contained entirely within any one of the four lobes. Elements spanning a lobar boundary were not used for regional average strain and fractional volume change quantification.

2.3. Results

2.3.1. Reconstructed HPG tagging images from under-sampled data

Figs. 2.6 and 2.7 depict coronal and sagittal slices from dynamic 3D grid-tagged lung images obtained in Subject 1, respectively. Figs. 2.8 and 2.9 depict coronal and sagittal slices from dynamic 3D grid-tagged lung images obtained in Subject 2, respectively. Figs. 2.10 and 2.11

depict coronal and sagittal slices from dynamic 3D grid-tagged lung images obtained in Subject 3, respectively.

In all subjects, an easily discernible grid pattern is maintained for several time points, despite the expected loss in tag definition due to signal decay and gas diffusion over the course of the imaging procedure. No distinct coherent artifacts were observed in reconstructed images, but SNR decreased over the course of the breathing maneuver for all subjects, and this decrease was most pronounced in the apices of the lungs. Additionally, SNR was noticeably lower in the lung apices than in the rest of the lung in Subjects 1 and 3 (Figs. 2.7 and 2.11, respectively), likely due to reduced flip angle in these locations as a result of the uneven coil sensitivity mentioned in Section 2.2.2. Sliding motion between upper and lower lung lobes was readily apparent in Subject 1 (Fig. 2.7), but not in Subjects 2 and 3.
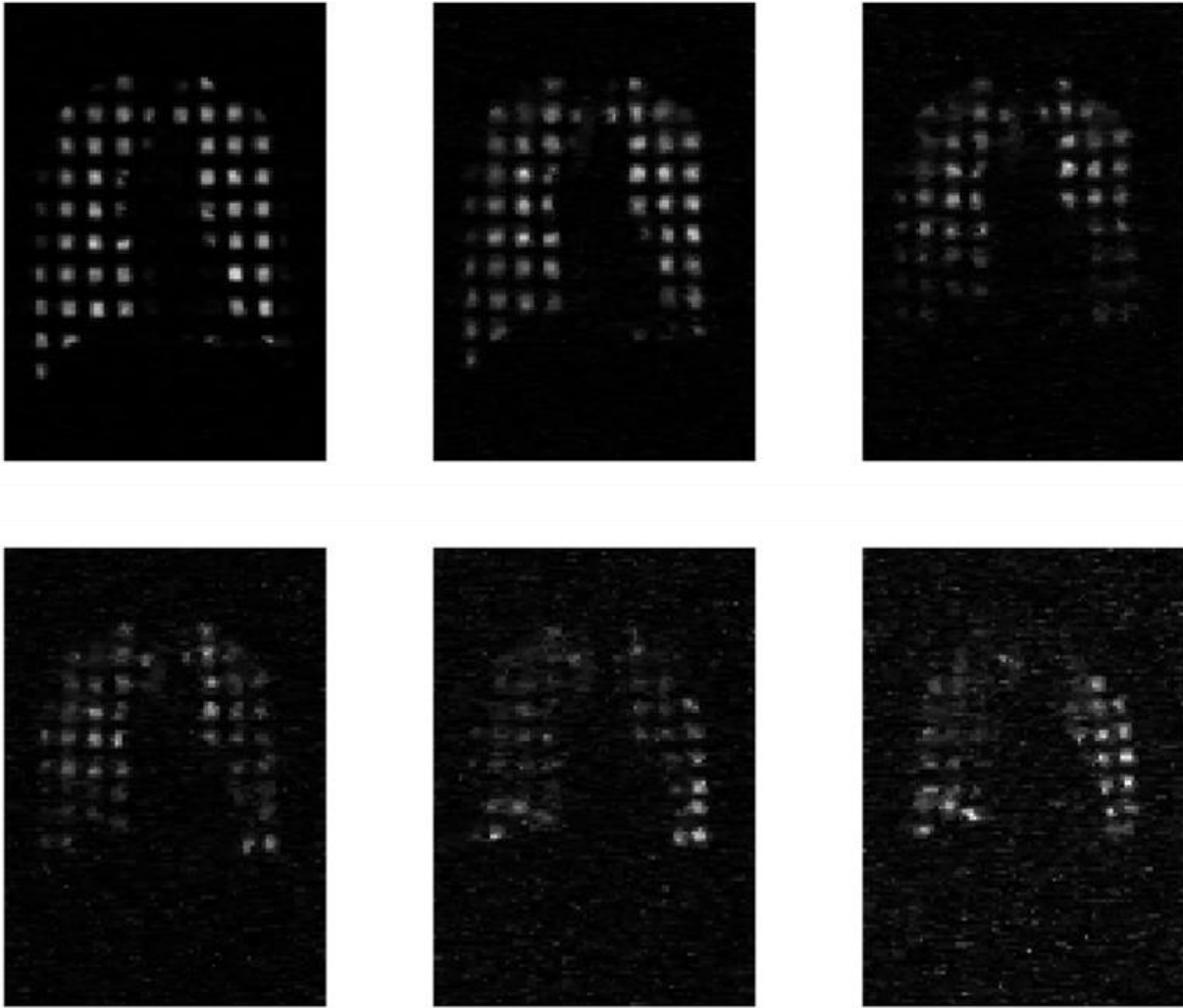
Figure 2.6: Coronal slices of serial tagged HPG images from Subject 1 at timepoints 1-3 (top row, left to right) and timepoints 4-6 (bottom row, left to right).
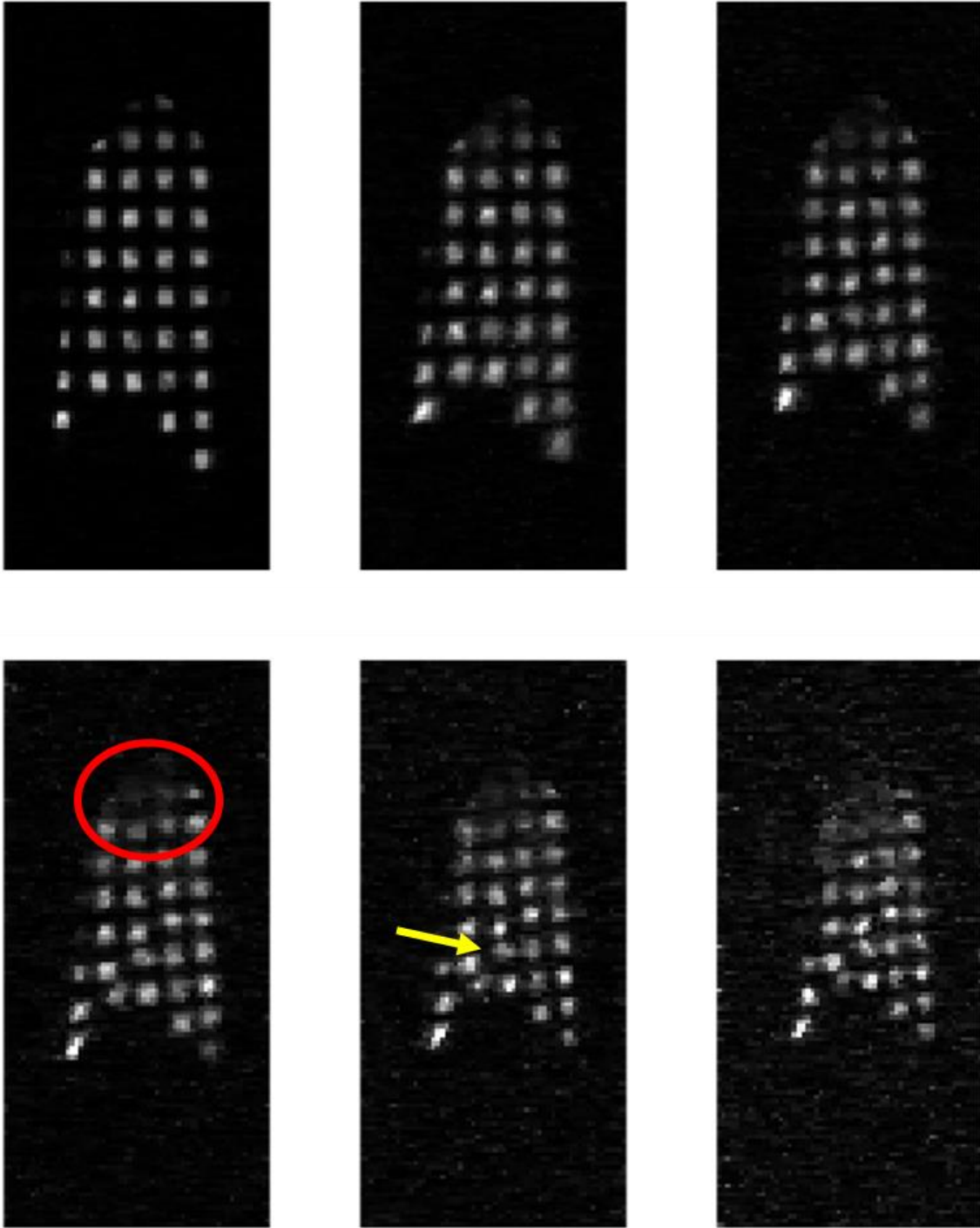
Figure 2.7: Sagittal slices of serial tagged HPG images from Subject 1 at timepoints 1-3 (top row, left to right) and timepoints 4-6 (bottom row, left to right). Apparent SNR in the lung apices was lower than in other regions of the lung in this subject, as indicated by the red circle at timepoint 4. Apparent lobar shearing can be seen in the final three frames, at the location indicated by the yellow arrow at timepoint 5.
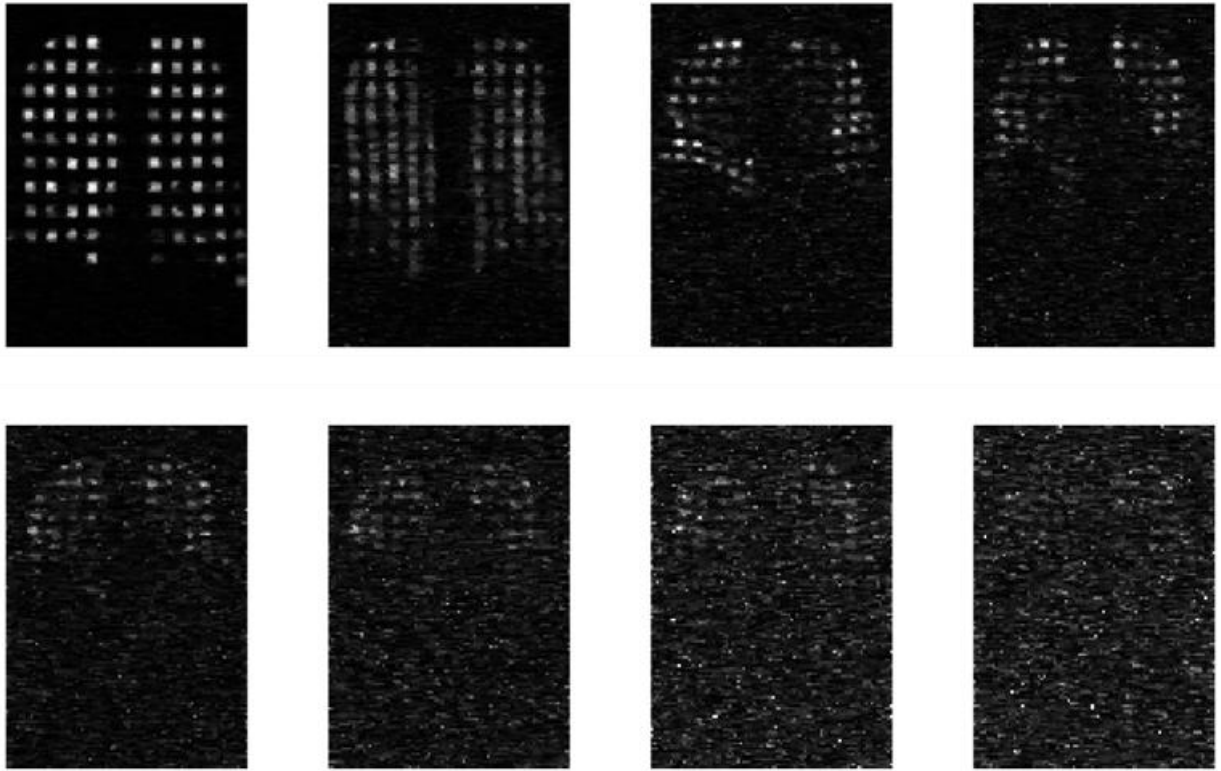
Figure 2.8: Coronal slices of serial tagged HPG images from Subject 2 at timepoints 1-4 (top row, left to right) and timepoints 5-8 (bottom row, left to right). The rapid exhalation in this subject resulting in decreased SNR and reduced ability to resolve individual tags at later timepoints, as well as a high degree of blurring in the second timepoint, during which most motion due to exhalation apparently occurred.
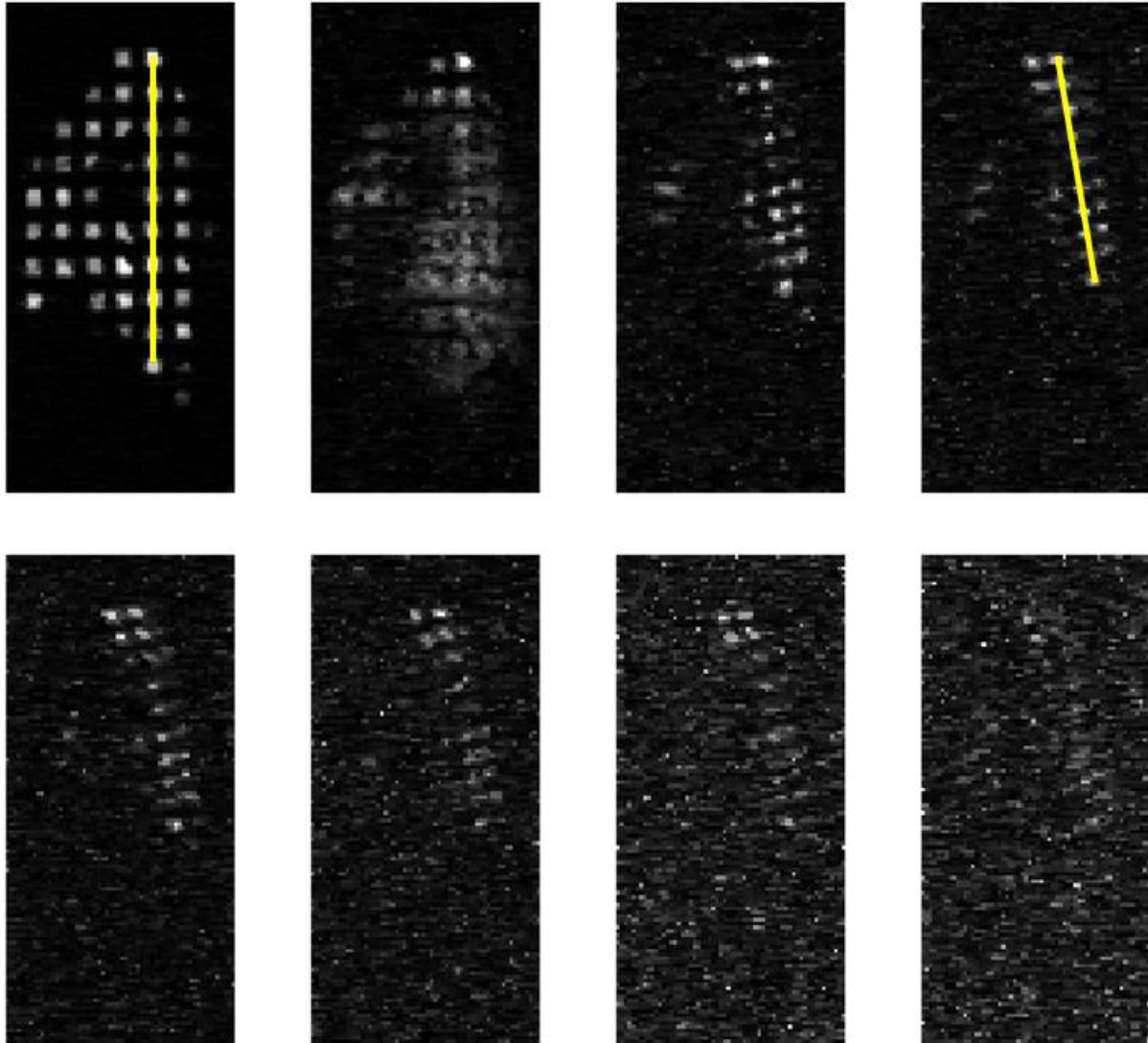
Figure 2.9: Sagittal slices of serial tagged HPG images from Subject 2 at timepoints 1-4 (top row, left to right) and timepoints 5-8 (bottom row, left to right). As with the coronal slices shown in Fig. 2.8, blurring due to rapid exhalation is apparent at the second timepoint. Apparent posterior-to-anterior motion of the superior regions of the lung is also evident in this subject, as illustrated by the yellow lines at timepoints 1 and 4.
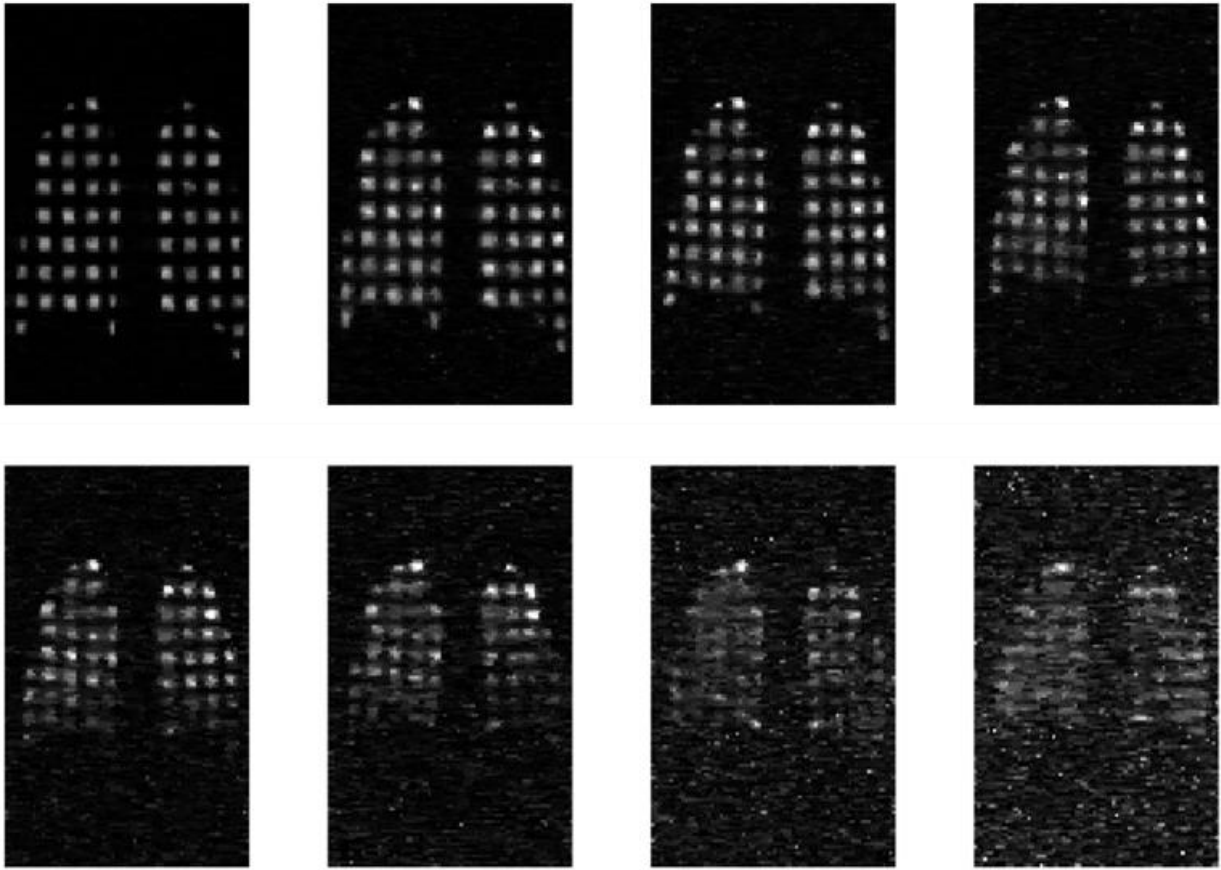
Figure 2.10: Coronal slices of serial tagged HPG images from Subject 3 at timepoints 1-4 (top row, left to right) and timepoints 5-8 (bottom row, left to right). Loss of tag definition at later timepoints in this subject appeared to be driven primarily by gas depolarization and diffusion, as exhalation appeared to be relatively slow throughout the imaging procedure.
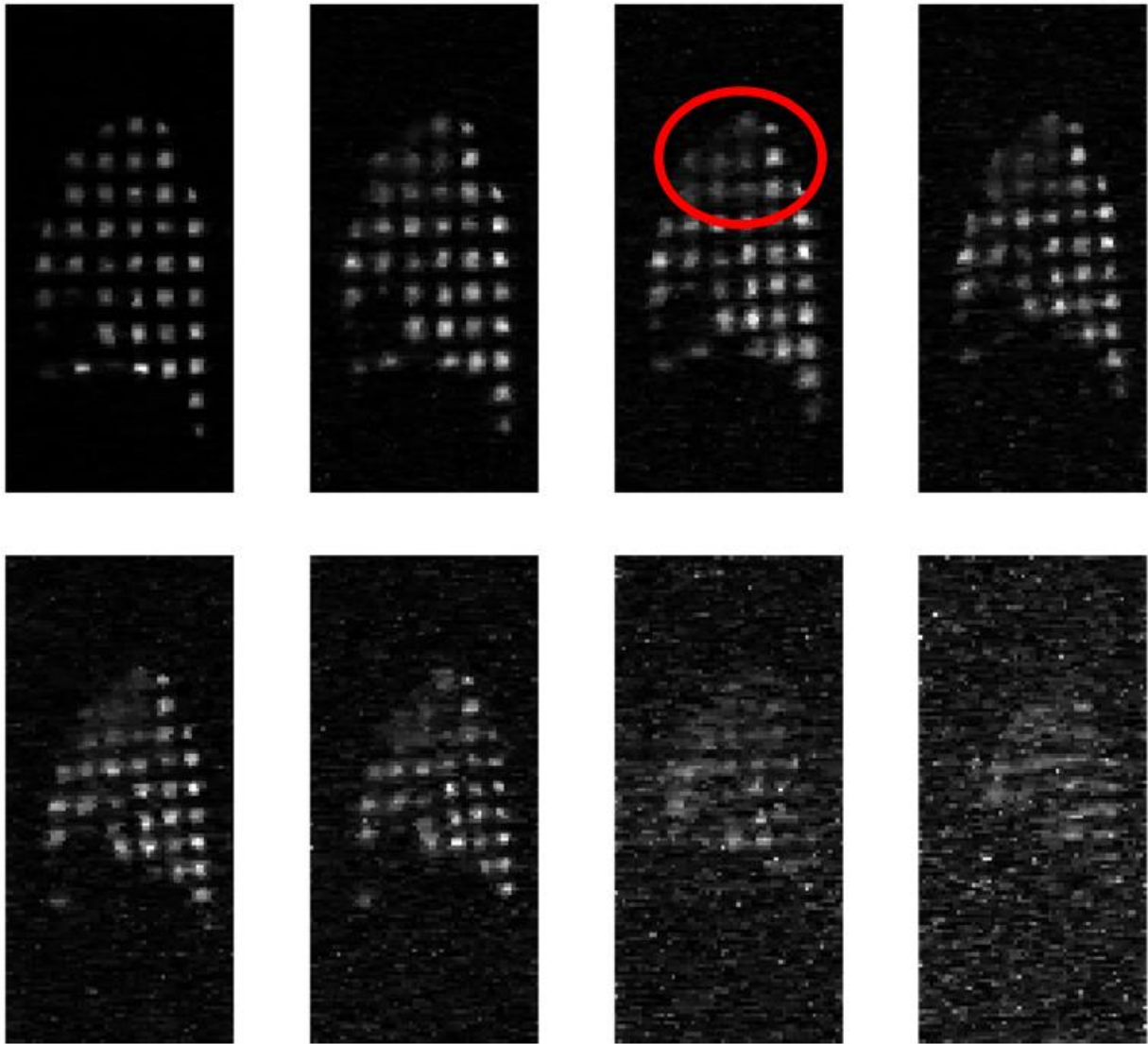
Figure 2.11: Sagittal slices of serial tagged HPG images from Subject 3 at timepoints 1-4 (top row, left to right) and timepoints 5-8 (bottom row, left to right). As with Subject 1, apparent SNR in the lung apices was lower than in other regions of the lung in this subject, as indicated by the red circle at timepoint 3.

2.3.2. Displacement maps

Two- and three-dimensional displacement maps are shown for Subject 1 in Fig. 2.12, and two-dimensional coronal and sagittal displacement maps are shown for Subjects 2 and 3 in Fig. 2.13. Tags remained distinct enough for semi-automated tracking for six 3D frames in Subject 1, four frames in Subject 2, and five frames in Subject 3, as judged visually during image analysis. In Subject 1, motion trajectories of the tags displayed significant temporal and spatial nonlinearity. Motion appeared to be straighter and faster at an earlier stage during the breathing maneuver, similar to behavior observed in previous work (10). Spatial nonlinearities are particularly evident at the apices of the lung, with tags located near the front of the lung moving primarily along the anterior-posterior axis, and tags located near the back of the lung moving primarily along the superior-inferior axis. In Subject 2, motion occurred almost entirely between the first and third image frame, while in Subject 3, motion was more evenly distributed temporally across all frames. However, because only five frames were collected in Subject 3 before tags became were judged too indistinct to track, full exhalation may not have been characterized. Both Subject 2 and Subject 3 displayed similar spatial nonlinearity patterns to Subject 1. In all subjects, motion in the anterior-posterior direction occurred primarily at the anterior edges of the lungs, motion in the left-right direction occurred primarily at the lateral edges of the lungs, and motion in the superior-inferior direction was greater in the inferior regions of the lungs than the superior regions, and greater in the posterior regions of the lungs than in the anterior regions.
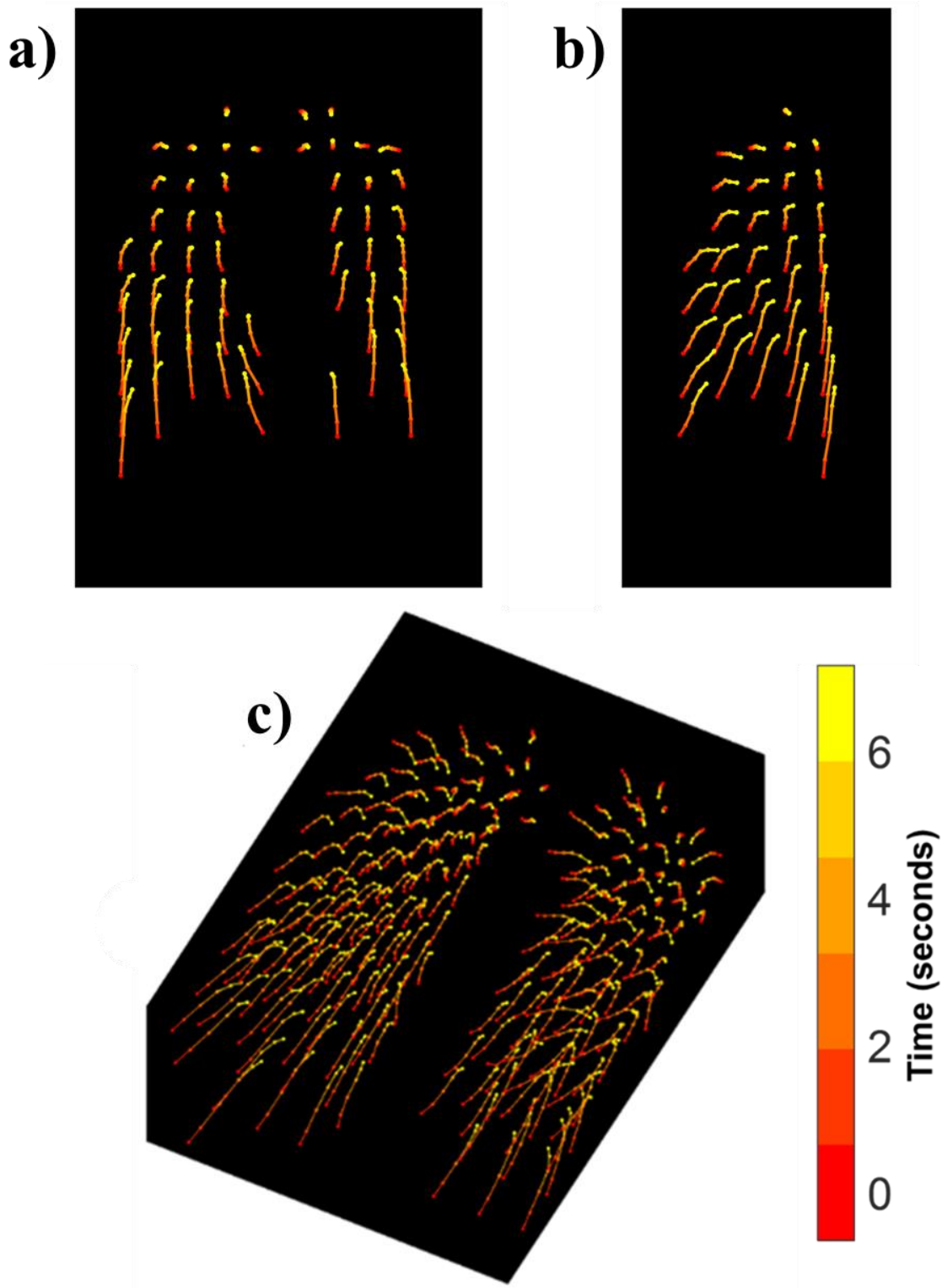
Figure 2.12: 2D displacement maps corresponding to the **a)** coronal and **b)** sagittal slices shown for Subject 1 in Figs. 2.6 and 2.7, and **c)** 3D displacement map for Subject 1. Six frames were used to form displacement maps.
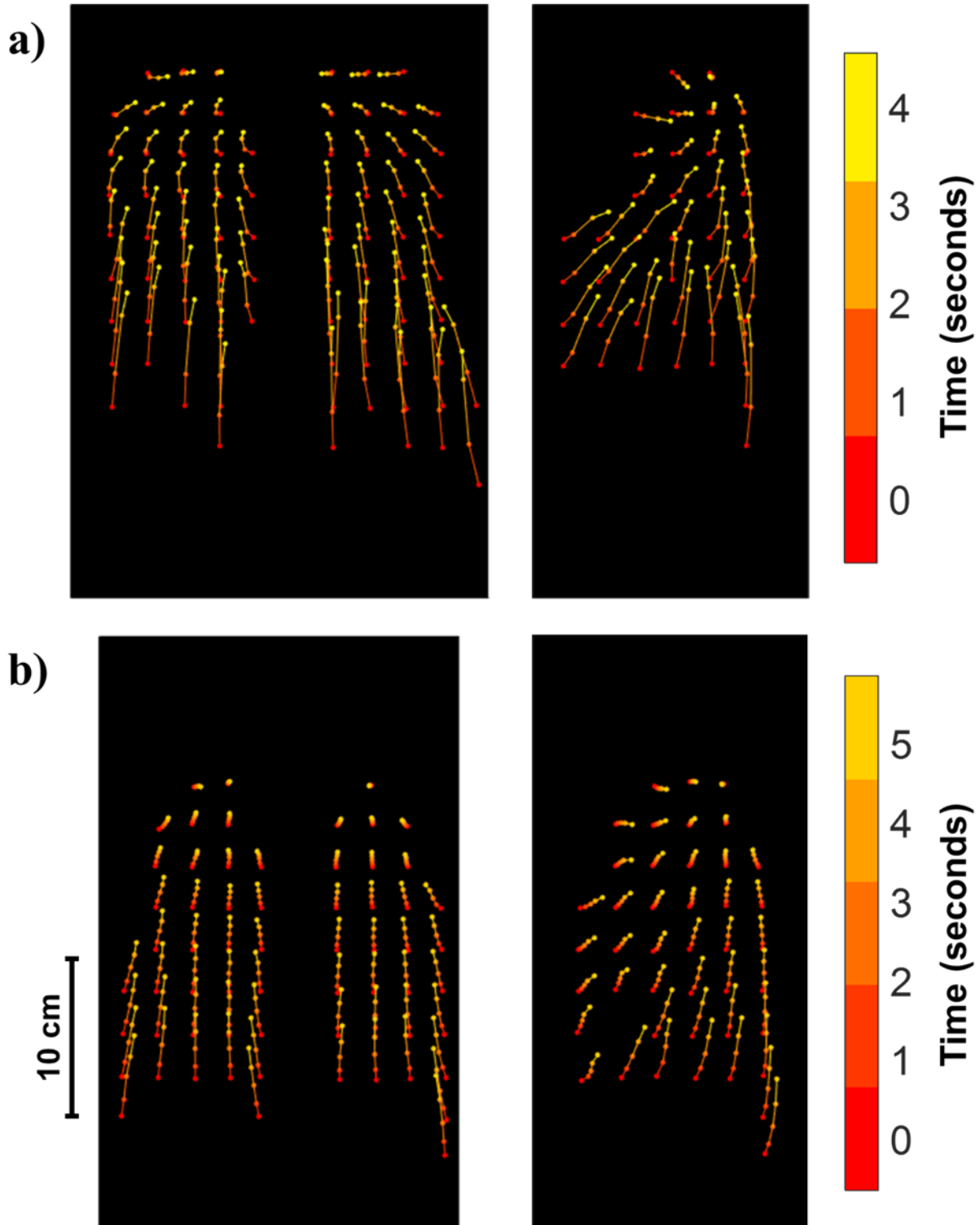
Figure 2.13: 2D coronal (left column) and sagittal (right column) displacement maps produced from HPG tagging images in **a)** Subject 2 and **b)** Subject 3. Four tagging frames were used to produce displacement maps in Subject 2, and five tagging frames were used to produce displacement maps in Subject 3.

2.3.3. Strain and fractional volume change

Maps of cumulative normal strain in the superior-inferior direction and shear strain normal to the anterior-posterior axis in Subject 1 are shown in a sagittal plane through the right lung in Fig. 2.14. As might be expected, virtually all normal strain components are compressive, and normal strain is most prevalent in the superior-inferior direction. Anomalously large apparent strain values are seen at the expected location of a lobar boundary, indicating likely sliding and/or shearing behavior occurring at this boundary. Fractional volume change maps through this same slice in Subject 1 are also shown in Fig. 2.14. Fractional volume change appears relatively homogenous, except for elements spanning the lobar boundary.
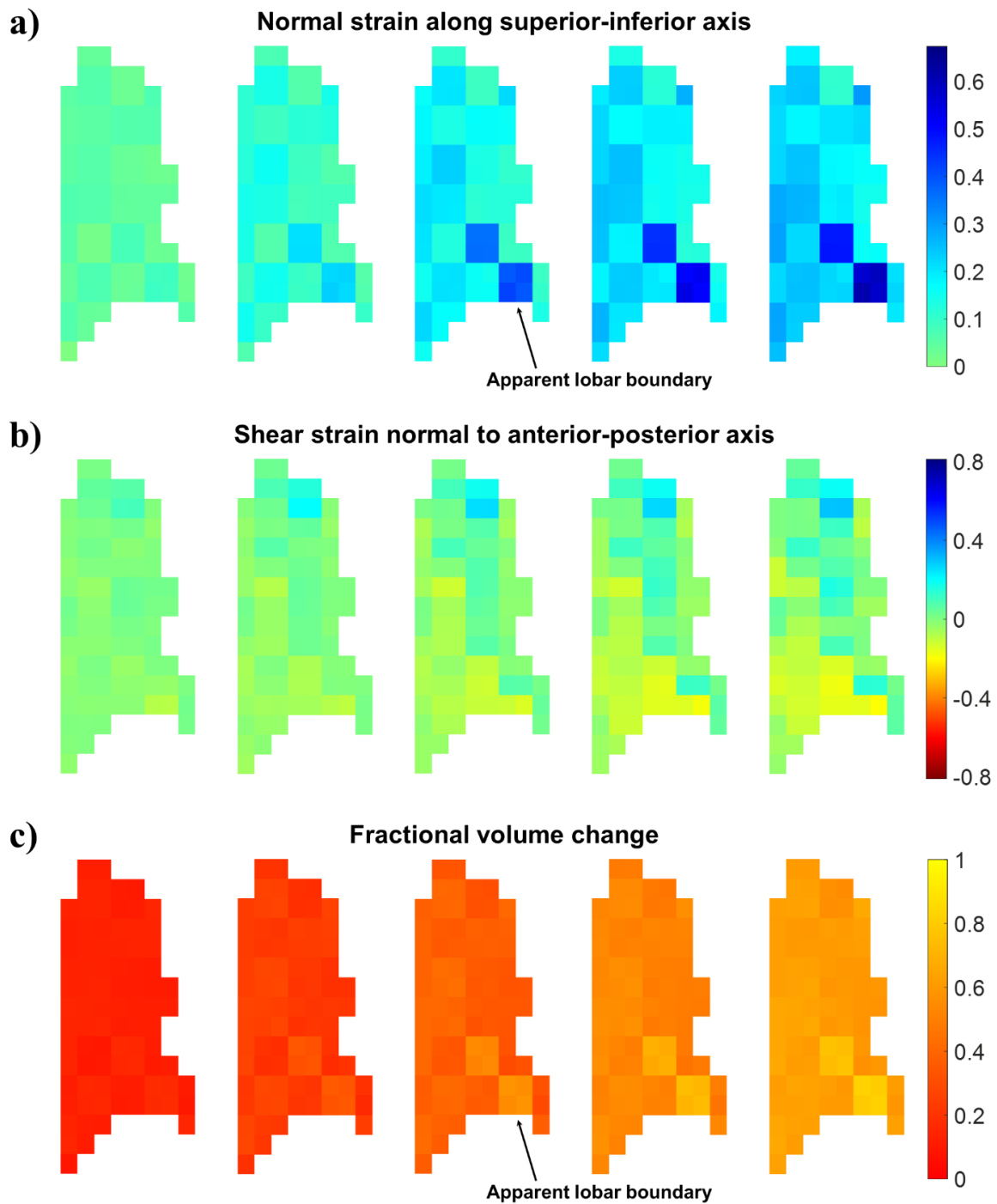
Figure 2.14: Maps of **a)** cumulative normal strain along the superior-inferior axis, **b)** cumulative shear strain normal to the anterior-posterior axis, and **c)** cumulative fractional volume change, during exhalation in a sagittal slice through the right lung in Subject 1. Positive numbers correspond to compressive strain in normal strain maps. An apparent lobar boundary can be seen in a) and c), characterized by regions of anomalously high normal strain and fractional volume change.

2.3.4. Lobar segmentation and average regional strains and volume changes

Results of lobar segmentation of tag data and lobar and whole-lung frame-to-frame average regional strains for Subject 3 are shown in Fig. 2.15. The segmented locations of the oblique fissures in the lungs match typical anatomy. The regional strain plots demonstrate that in this subject, motion and normal strain in the superior-inferior direction are predominant early in the exhalation maneuver, while motion and normal strain in the other two principal directions predominate later. Shear strains were of smaller magnitude than normal strains in this subject, and generally hovered near zero, except in the case of shear strain normal to the left-right axis (i.e. coplanar to the sagittal plane).
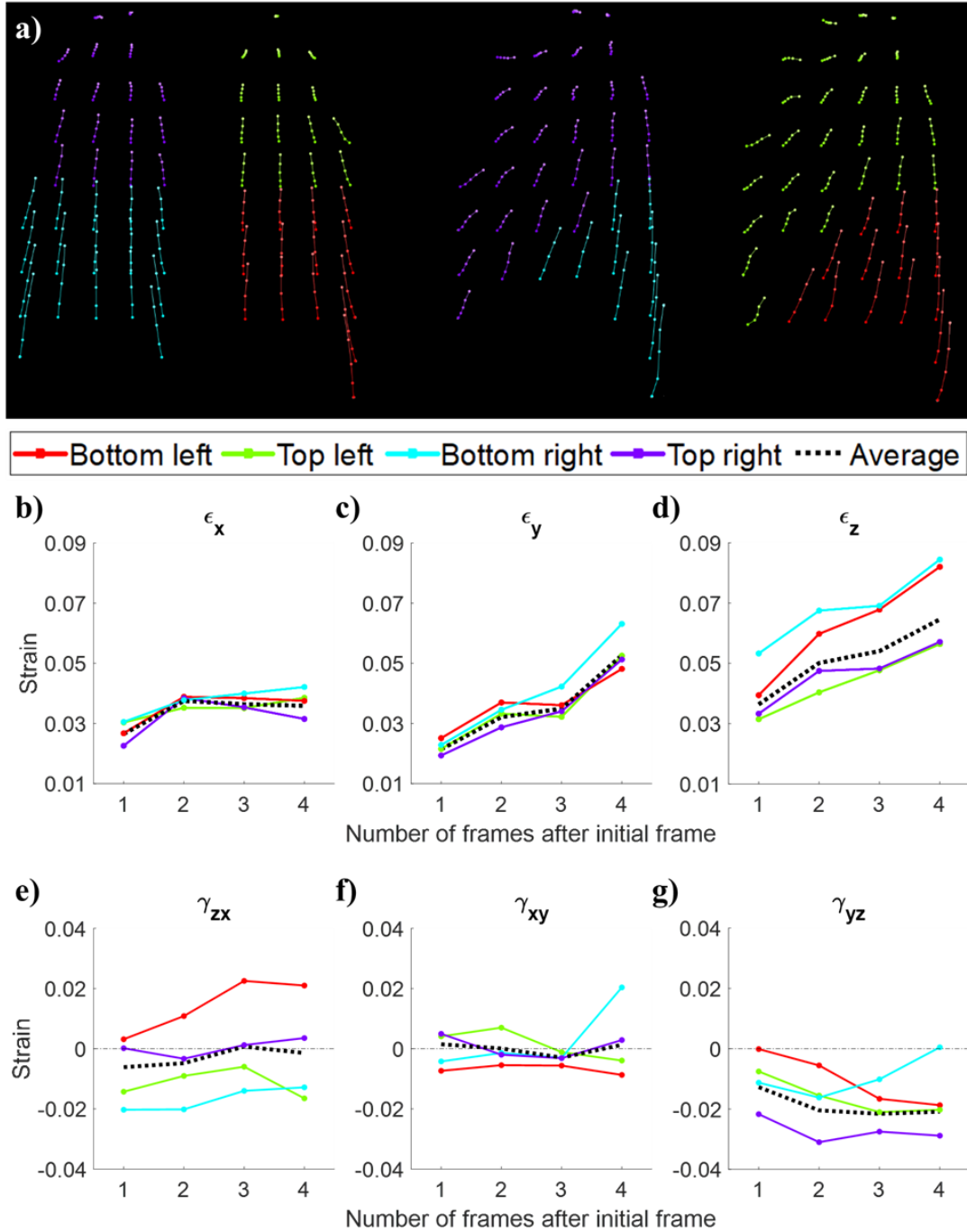
Figure 2.15: **a)** Dynamic displacement maps of selected tag planes, depicting results of regional (lobar) segmentation in Subject 3. From left to right, the panel depicts: a coronal plane through both lungs, a sagittal plane through the right lung, and a sagittal plane through the left lung. **b-g)** Plots depicting average frame-by-frame normal and shear strains within each of the four segmented lung lobes in Subject 3, as well as average strains across all four segmented lung lobes. Positive numbers correspond to compressive strain for all normal strain plots. Subscripts x, y, and z refer to the left-right direction, the anterior-posterior direction, and the superior-inferior direction, respectively.

Lobar cumulative fractional volume change is shown for all three subjects in Fig. 2.16. Strong bilateral symmetry is evident in all three subjects. In Subject 1, there is no apparent vertical gradient, while in Subjects 2 and 3, the two lower lobes exhibit higher fractional volume change over the span of the breathing maneuver than the two upper lobes. Fractional volume change is relatively linear across the breathing maneuver in Subjects 1 and 3, but undergoes a rapid increase between the second and third temporal frames in Subject 2, consistent with the appearance of the corresponding tagged gas images.
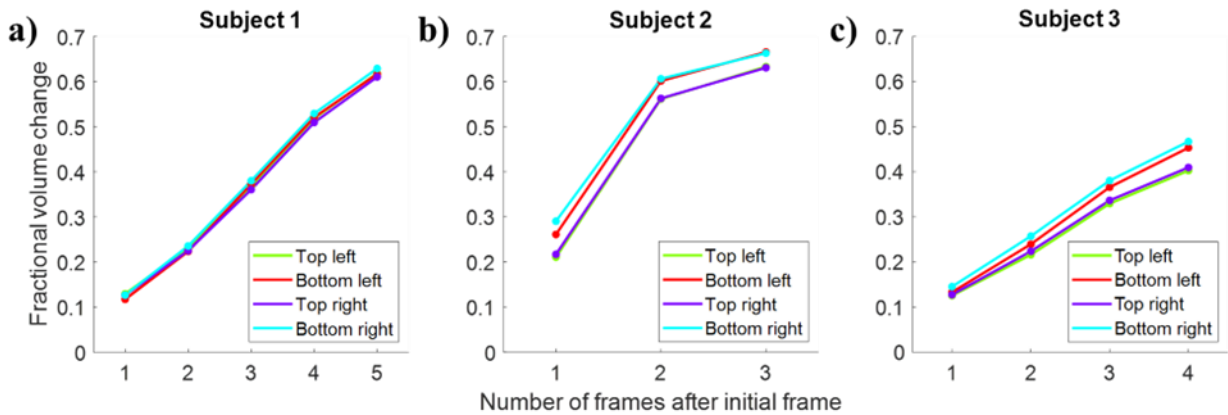
Figure 2.16: Plots depicting average cumulative fractional volume change within each of the four segmented lung lobes in **a)** Subject 1, **b)** Subject 2, and **c)** Subject 3.

2.4. Discussion

Our results demonstrate that tagged HPG MRI of the lung is a promising method for studying pulmonary kinematics and for characterizing complex deformation during the breathing cycle. Previously, time constraints imposed by *k*-space sampling requirements, tag diffusion, and gas signal decay had limited the use of HPG tagging to collecting either two 3D images or multiple 2D images within a single breathing cycle. We present a technique that allows collection of serial 3D tagged hyperpolarized gas lung images within a single breathing cycle, using variable-density *k*-space under-sampling – matched to the predicted layout of signal within *k*-space – and compressed-sensing reconstruction of the under-sampled data. We additionally demonstrate calculation of time-resolved 3D strain and specific ventilation maps and regional strain and specific ventilation profiles using these tagged images.

These data provide initial insight into the number of 3D tagged frames that might be acquired in a single breathing maneuver. In these individuals, 4–6 frames, acquired over a span of approximately 6–8 s, were successfully acquired before tags were judged too indistinct to permit successful tag registration for subsequent frames. At this acquisition speed, the technical focus of the basic hyperpolarized-gas tagging technique shifts from simply acquiring two 3D frames (at end-of-inhalation and end-of-exhalation) within a single breath-hold maneuver to acquiring as many intermediate 3D frames as practical in order to create the fullest characterization of pulmonary kinematics possible. The increased acquisition speed could also offer the opportunity to use finer tag spacing and imaging resolution, allowing higher-detail displacement maps to be calculated and potentially facilitating robust detection of lobar fissures.

These scans were performed in healthy individuals, with strain and fractional volume-change results generally matching those shown in previous imaging studies in healthy individuals using CT (34,35). It should be straightforward to apply the same techniques in individuals with lung diseases known to cause heterogeneities in regional pulmonary compliance, such as idiopathic pulmonary fibrosis (3), or individuals with neuromuscular disease affecting respiratory muscle strength and lung biomechanics (36–38). Should such work demonstrate the ability of tagged HPG MRI to resolve disease-related regional disturbances in lung biomechanics, it would serve as powerful validation of the technique's efficacy and potential as a tool for pulmonary disease research.

Prior HPG tagging workflows have been investigated as a method for validating 4D deformable image registration (DIR) models of lung motion during the breathing cycle that are used to guide 4D radiation therapy for lung tumors (8,10–12). While promising, this technique has previously been limited in its ability to directly compare with 4D DIR models, due to the lack of tagging data at intermediate points in the breathing cycle. The ability to serially collect 3D images within a single breathing cycle significantly advances the applicability of tagged HPG imaging of the lung for this purpose, by allowing the tagging-based validation of DIR models to be performed at intermediate points in the breathing cycle in addition to the two extremes.

Loss of tag integrity in later frames can be largely attributed to tag diffusion and gas signal decay. Tag diffusion is driven by the long-range diffusivity (i.e., diffusion beyond the bounds of individual acinar airways) of the hyperpolarized gas, which drives signal-rich hyperpolarized gas

into regions of low signal between tags, causing boundaries between tags to become less distinct and eventually causing tags to bleed together entirely. This behavior has been characterized using techniques designed to measure long-time-scale ^{3}He diffusion in vivo, with long-time-scale apparent diffusion coefficient (ADC) values of roughly 0.02 cm^2/s observed for ^{3}He in healthy individuals (13–15,39). In individuals with lung pathologies such as emphysema, the ADC of ^{3}He is generally higher than in healthy individuals (14,15,39). Acceleration of the tagging sequence will thus only become more important in these contexts, as tags would be expected to diffuse and dissolve even more rapidly.

The effect of tag diffusion might be drastically mitigated by using ^{129}Xe as an inhaled hyperpolarized gas instead of ^{3}He, as the diffusivity of ^{129}Xe is several-fold smaller than that of ^{3}He. Moreover, the abundant natural supply of ^{129}Xe relative to ^{3}He means that any future clinical (or research) applications of HPG tagging MRI will almost certainly use ^{129}Xe. Two-phase 3D grid tagging has been successfully demonstrated using ^{129}Xe (11,12) and the developments presented here should be equally applicable to ^{129}Xe.

One drawback of the technique presented here is that the energy peaks in k-space move further apart and become slightly wider over the course of the imaging procedure as a result of the decreasing separation between tags during exhalation, while the peaks of the sampling likelihood function were not adjusted to account for this. This limitation could potentially be mitigated in the future by increasing the width of the peaks of the sampling density function (and by doing so, increasing the total number of sampled lines per frame) over the course of the breathing maneuver. This approach would ensure that peaks are sampled densely in all frames, and would also mitigate the decrease in SNR over the course of the breathing maneuver due to gas depolarization. Alternatively, prior to the start of each 3D tagging frame, 1D navigators could be applied along each of the three principal directions and used to estimate current locations of k-space energy centers. The sampling pattern for the corresponding frame would then be adjusted in real time in order to account for the new distribution of k-space energy.

An undersampled Cartesian readout scheme was chosen for this study in order to take advantage of the initial Cartesian layout of k-space energy peaks in the tagging context. An alternative approach might be to design a 3D radial readout scheme with preferential sampling of radial lines oriented through the expected locations of k-space energy peaks. Such an approach could

mitigate the aforementioned issue posed by motion of the peaks in *k*-space during breathing, as this motion occurs principally along a radial path with respect to the *k*-space center. The traditional advantages offered by a radial sampling scheme relative to Cartesian sampling – higher *k*-space sampling rate per unit time, shorter TR and TE, and naturally noise-like undersampling artifacts – would all potentially improve HPG tagging MRI. Previous work has demonstrated 2D radial sampling in dynamic HPG tagging MRI (10), and this approach would be straightforward to adapt to 3D.

A limitation of all HPG tagging implementations to date, including the one described here, is that imaging occurs only during exhalation. An interesting direction for future work would be development of a combined inhalation/exhalation acquisition, with an eye toward directly calculating regional lung hysteresis and fractional volume change. Successful implementation would require the tags to remain distinct throughout both exhalation and inhalation, but the imaging acceleration techniques demonstrated here could help in this regard. Using ^{129}Xe instead of ^{3}He would also likely facilitate longer tag preservation due to the lower diffusivity of ^{129}Xe compared with ^{3}He, as mentioned previously.

Another interesting future direction would be the use of a fully automated tag tracking algorithm, as this work used a semi-automated tracking and registration approach that required an operator to assess displacement map fidelity and occasionally intervene manually in instances of apparent tag misregistration. Previous work has demonstrated automated tag tracking in two-phase 3D HPG tagging MRI (7), and such a method could be tested in the multi-phase context as well. Alternatively, novel reconstruction approaches for under-sampled 4D MR image data that include estimations of frame-to-frame motion as part of the reconstruction might be of significant interest in the tagging MRI context (40,41).

In this study, we described a CS-based method for multiframe 3D MRI of grid-tagged HPG in the lung during exhalation, taking advantage of the predictable distribution of *k*-space energy imposed by using an RF pulse train to apply a grid pattern to inhaled hyperpolarized ^{3}He. We collected high-quality dynamic images of grid-tagged ^{3}He during exhalation using the described technique. Finally, we demonstrated calculation of multiple-time-point displacement and strain maps and lobar strain profiles from resulting images of grid-tagged ^{3}He. These maps readily capture and demonstrate the 4D nature of lung motion during the breathing cycle, and highlight a

potential role for HPG-tagging MRI data as an accurate biomarker of spatially resolved pulmonary biomechanics.

2.5. Appendix

2.5.1. Tagging grid creation using a sinc-modulated RF pulse train

The excitation k-space description of the creation of a tagging grid using a sinc-modulated RF pulse train is given below. The given description is for tagging along a single dimension, but a tag pattern can be applied along any direction by altering the direction of the gradient, or along several dimensions for one scan by repeating the tagging pulse sequence with the gradient oriented along each of the desired dimensions. This description draws heavily from Wu *et al* (20), Pauly *et al* (42), and chapter 16 of *Magnetic Resonance Imaging: Physical Principles and Sequence Design* by Brown *et al* (43).

The Bloch equation (Eq. 1.15) with T_1 and T_2 neglected is as follows:

$$\frac{d\vec{M}}{dt} = \gamma \vec{M} \times \vec{B} \tag{2.7}$$

During application of a circularly-polarized RF field $\vec{B}_1$ and a gradient $\vec{G}$, the total magnetic field applied to the sample is as follows:

$$\vec{B} = B_0 \hat{z} + \vec{B}_1 + (\vec{G} \cdot \vec{r}) \hat{z} \tag{2.8}$$

When the sample is considered in the rotating frame, the B_0 term can be eliminated. Assuming that the B_1 field is zero along the z-axis (i.e., $B_{1,z} = 0$), Eq. 2.8 can be written in terms of the magnetization components as follows:

$$\begin{pmatrix} dM_x/dt \\ dM_y/dt \\ dM_z/dt \end{pmatrix} = \gamma \begin{pmatrix} 0 & \vec{G} \cdot \vec{r} & -B_{1,y} \\ -\vec{G} \cdot \vec{r} & 0 & B_{1,x} \\ B_{1,y} & -B_{1,x} & 0 \end{pmatrix} \begin{pmatrix} M_x \\ M_y \\ M_z \end{pmatrix} \tag{2.9}$$

By using the small-tip-angle approximation, combining M_x and M_y into a complex transverse magnetization component:

$$M_+ = M_x + iM_y \tag{2.10}$$

and doing likewise with $B_{1,x}$ and $B_{1,y}$:

$$B_{1+} = B_{1,x} + iB_{1,y} \tag{2.11}$$

the equation of motion can be reduced to the following:

$$\frac{dM_+}{dt} = -i\gamma(\vec{G} \cdot \vec{r})M_+ + i\gamma B_{1+}M_0 \tag{2.12}$$

Solving Eq. 2.12 yields the following expression for the transverse magnetization at the end of the RF pulse sequence as a function of position $\vec{r}$ and RF pulse profile $B_{1+}(t)$:

$$M_+\left(\vec{r}, \tau_{rf}/2\right) = i\gamma M_0 \int_{-\tau_{rf}/2}^{\tau_{rf}/2} B_{1+}(t)e^{-i2\pi\vec{k}(t)\cdot\vec{r}}dt \tag{2.13}$$

where k is defined as a function of the gradient G as follows:

$$\vec{k}(t) = \frac{\gamma}{2\pi} \int_{t}^{\tau_{rf}/2} \vec{G}(s)ds \tag{2.14}$$

for an RF pulse or series of pulses defined over a time interval of length τ_{rf} centered at $t = 0$.

For a gradient of constant amplitude G throughout the RF window, oriented along the x-axis, the expression simplifies as follows:

$$M_+\left(x, \tau_{rf}/2\right) = i\gamma M_0 e^{-i\gamma Gx\tau_{rf}/2} \int_{-\tau_{rf}/2}^{\tau_{rf}/2} B_{1+}(t)e^{i\gamma Gxt}dt$$
$$= i\gamma M_0 e^{-i\gamma Gx\tau_{rf}/2}\mathcal{F}^{-1}\left(B_{1+}(t)\right) \tag{2.15}$$

In words, this indicates that the transverse magnetization as a function of space can be approximated as the inverse Fourier transform of the RF pulse as a function of time, assuming that the RF pulse occurs during application of a constant gradient.

We can use this relationship to identify that a sinc-modulated RF pulse train is approximately suitable for grid tagging. Such a pulse train can be described by the following functional form:

$$B_{1+}(t) = sinc\left(\frac{\pi t}{\Delta t_1}\right) \times comb(t, \Delta t_2) \tag{2.16}$$

where Δt_1 is the time of the first zero crossing of the sinc function, and Δt_2 is the spacing of the comb function.

The desired transverse magnetization following RF excitation can then be described using the following function:

$$M_+\left(x, \tau_{rf}/2\right) = rect\left(\frac{\gamma}{2\pi}G\Delta t_1 x\right) \otimes comb\left(x, \frac{1}{\frac{\gamma}{2\pi}G\Delta t_2}\right) \tag{2.17}$$

where $\otimes$ denotes convolution. In practice, it is not possible to perform RF pulses of infinitesimal width as described above. Assuming that each individual RF pulse will take a time Δt_3 to occur, the true expression for the sinc-modulated RF pulse train is as follows:

$$B_{1+}(t) = \left(sinc\left(\frac{\pi t}{\Delta t_1}\right) \times comb(t, \Delta t_2)\right) \otimes rect\left(\frac{t}{\Delta t_3}\right) \tag{2.18}$$

and the transverse magnetization profile will then be as follows:

$$M_+\left(x, \tau_{rf}/2\right) = \left(rect(\gamma G\Delta t_1 x) \otimes comb\left(x, \frac{1}{\gamma G\Delta t_2}\right)\right)$$
$$\times sinc(\pi\gamma G\Delta t_3 x) \tag{2.19}$$

The extra sinc term represents shading that is particularly evident far from the center of the field of view. This behavior can be eliminated by replacing the constant gradient G with a series of "blipped" gradients of the same amplitude as the original constant gradient, but played only during gaps between individual RF pulses. In order to understand this approach, it is necessary to perform a change of variable in the original expression for transverse magnetization such that the

75

gradient and RF terms are represented as functions of position in excitation k-space rather than functions of time, as follows:

$$M_+\left(x, \tau_{rf}/2\right) = i\gamma M_0 \int_{-\tau_{rf}/2}^{\tau_{rf}/2} B_{1+}(t)e^{-i2\pi k(t)\cdot x}dt$$

$$= i\gamma M_0 \int_{k(-\tau_{rf}/2)}^{k(\tau_{rf}/2)} \frac{B_{1+}\left(k(t)\right)}{\left|\frac{\gamma}{2\pi} G\left(k(t)\right)\right|} e^{-i2\pi k(t)\cdot x}dk$$

(2.20)

Using this formalism, we see that the spatial profile of the transverse magnetization is the Fourier transform of the RF pulse as a function of excitation k-space position, divided by the gradient as a function of excitation k-space position.

The sinc-modulated rectangular RF pulse train played in the intervals between blipped gradients can be expressed as a function of k as follows:

$$B_{1+}(k(t)) = sinc\left(\frac{\pi k(t)}{\Delta k_s}\right) \times comb(k(t), \Delta k_c)$$

(2.21)

where the pulse spacing Δk_c is given by:

$$\Delta k_c = \frac{\gamma}{2\pi} G(\Delta t_2 - \Delta t_3)$$

(2.22)

and the sinc width parameter Δk_s is given by:

$$\Delta k_s = \frac{\gamma}{2\pi} G\Delta t_1 \left(1 - \frac{\Delta t_3}{\Delta t_2}\right)$$

(2.23)

The individual pulses comprising the pulse train are impulses with respect to k, as no gradients are executed during the individual pulses and therefore k does not advance while the individual pulses occur.

The blipped gradient pulses can still be understood to be constant with respect to k, such that:

$$G\left(k(t)\right) = G$$

(2.24)

The above expressions for $B_{1+}(k(t))$ and $G(k(t))$ have been simplified by omitting the rect function enclosing each of them in $k(t)$, as this rect function is identical for both $B_{1+}(k(t))$ and $G(k(t))$ and thus disappears once the two quantities are divided below.

The transverse magnetization can then be determined by evaluating the above Fourier transform, as follows:

$$
\begin{aligned}
M_+\left(x, \tau_{rf}/2\right) &= i\gamma M_0 \int_{k(-\tau_{rf}/2)}^{k(\tau_{rf}/2)} \frac{B_{1+}\left(k(t)\right)}{\left|\frac{\gamma}{2\pi} G\left(k(t)\right)\right|} e^{-i2\pi k(t)\cdot x} dk \\
&= i\gamma M_0 \int_{k(-\tau_{rf}/2)}^{k(\tau_{rf}/2)} \frac{sinc\left(\frac{\pi k(t)}{\Delta k_s}\right) \times comb(k(t), \Delta k_c)}{\left|\frac{\gamma}{2\pi} G\right|} e^{-i2\pi k(t)\cdot x} dk \\
&= \frac{1}{\frac{\gamma}{2\pi} G} \cdot rect\left(\left(\frac{\gamma}{2\pi} G\Delta t_1 \left(1 - \frac{\Delta t_3}{\Delta t_2}\right)\right) x\right) \\
& \quad * comb\left(x, \frac{1}{\frac{\gamma}{2\pi} G(\Delta t_2 - \Delta t_3)}\right)
\end{aligned}
$$

(2.25)

This magnetization profile – a rect function convolved with a comb function – matches the desired result in the tagging MRI context. In this expression, the tag width w_{tag} is given by:

$$
w_{tag} = 2\pi / \left(\gamma G\Delta t_1 \left(1 - \frac{\Delta t_3}{\Delta t_2}\right)\right)
$$

(2.26)

and the center-to-center tag spacing Δx_{tag} is given by:

$$
\Delta x_{tag} = 2\pi / (\gamma G[\Delta t_2 - \Delta t_3])
$$

(2.27)

Recall that Δt_1 represents the first zero-crossing time of the sinc-modulated RF pulse train, Δt_2 represents the center-to-center spacing of the rectangular RF pulses, and Δt_3 represents the width of each RF pulse. Since the gradient is only turned on during the time between RF pulses, which is equal to $\Delta t_2 - \Delta t_3$, the tag spacing can be expressed more generally as:

$$\Delta x_{tag} = 2\pi / (\gamma G_{Moment}) \qquad (2.28)$$

where G_{Moment} represents the zeroth moment of each blipped gradient pulse.

The form for B_{1+} as a function of $k(t)$ shown above holds not only for sinc-modulated RF pulses of equal length, but for RF pulses of identical amplitude and different lengths, such that the area under each sequential RF pulse matches the area under its equivalent pulse in the case of sinc-modulated amplitude. This observation offers the opportunity to shorten the tagging MRI pulse sequence by using shorter, higher-amplitude RF pulses over the course of the sequence (Fig. 2.17).
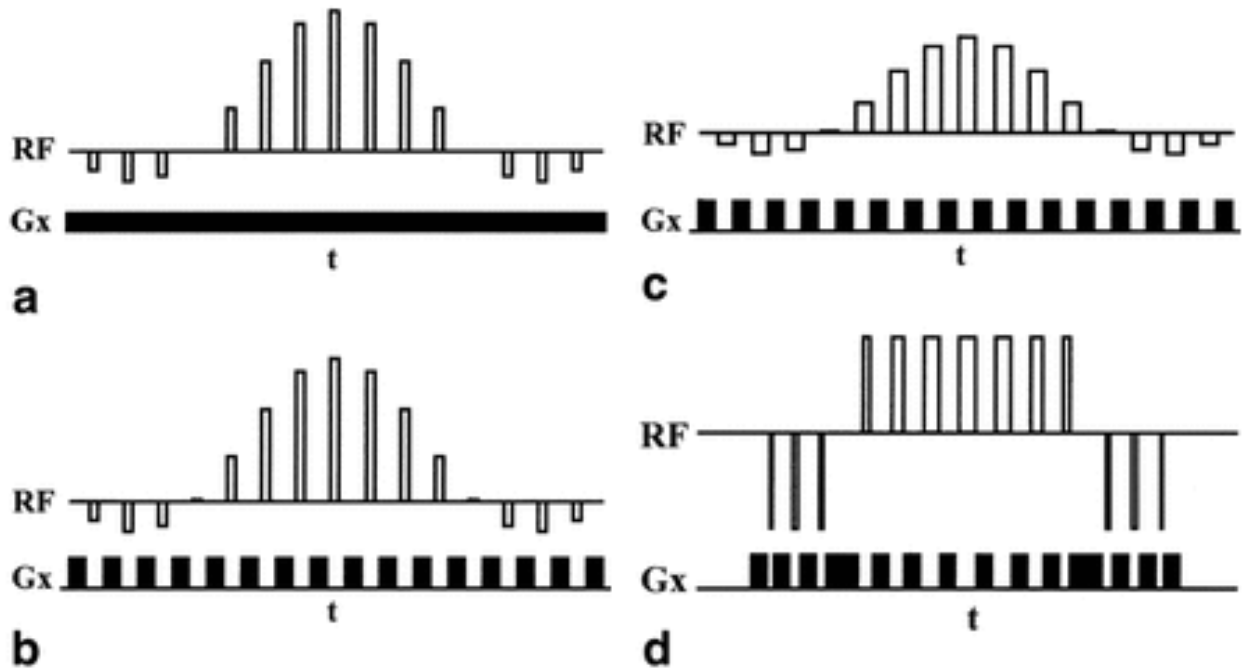
Figure 2.17: Sinc-modulated RF pulse trains with **a)** a constant gradient, **b)** blipped gradients, and **c)** blipped gradients combined with shorter, wider RF pulses to reduce peak power requirement, as well as **d)** a pulse train composed of constant-amplitude RF pulses of equivalent area to those in a-c). Reproduced from Wu *et al* (20).

2.5.2. Finite-element-based strain calculation

The process of deriving element-wise strains and volumes for an individual four-node tetrahedral element is described below. This description largely recapitulates that given in chapter 10.1 of *Finite Element Analysis* by Moaveni (44).

Start by approximating the displacement field (u, v, w) from one time point to another time point within a three-dimensional coordinate system (X, Y, Z) as a linear function of position, as follows:

$$
\begin{aligned}
u(X,Y,Z) &= C_{11} + C_{12}X + C_{13}Y + C_{14}Z \\
v(X,Y,Z) &= C_{21} + C_{22}X + C_{23}Y + C_{24}Z \\
w(X,Y,Z) &= C_{31} + C_{32}X + C_{33}Y + C_{34}Z
\end{aligned} \tag{2.29}
$$

where the constants C_{mn} relate the positional coordinates (X, Y, Z) to the displacement field (u, v, w). For instance, C_{13} relates the amplitude of the displacement along the X-axis to a given Y coordinate in space.

The known displacement values at the initial locations of the four nodes of the tetrahedron (I, J, K, L) can be taken as boundary conditions for the above equations, as follows:

$$
\begin{aligned}
u &= u_I \ at \ (X,Y,Z) = (X_I, Y_I, Z_I) \\
u &= u_J \ at \ (X,Y,Z) = (X_J, Y_J, Z_J) \\
&\vdots \\
w &= w_L \ at \ (X,Y,Z) = (X_L, Y_L, Z_L)
\end{aligned} \tag{2.30}
$$

A four-node tetrahedron is depicted in Fig. 2.18. In the tagging MRI context, the coordinates X, Y, and Z correspond to the location of a tag in the earlier of a pair of tagging images, and the displacements u, v, and w correspond to the difference in locations of the tag in question between the earlier and later images in the pair of tagging images along the X, Y, and Z directions, respectively. For instance, let vertex I of a tetrahedral element be defined by a given tag. The initial location of the tag along the X, Y, and Z directions can be denoted as X_I, Y_I, and Z_I, respectively. The difference in locations between the initial and final position of the tag along the X, Y, and Z directions can be denoted as u_I, v_I, and w_I, respectively.

79
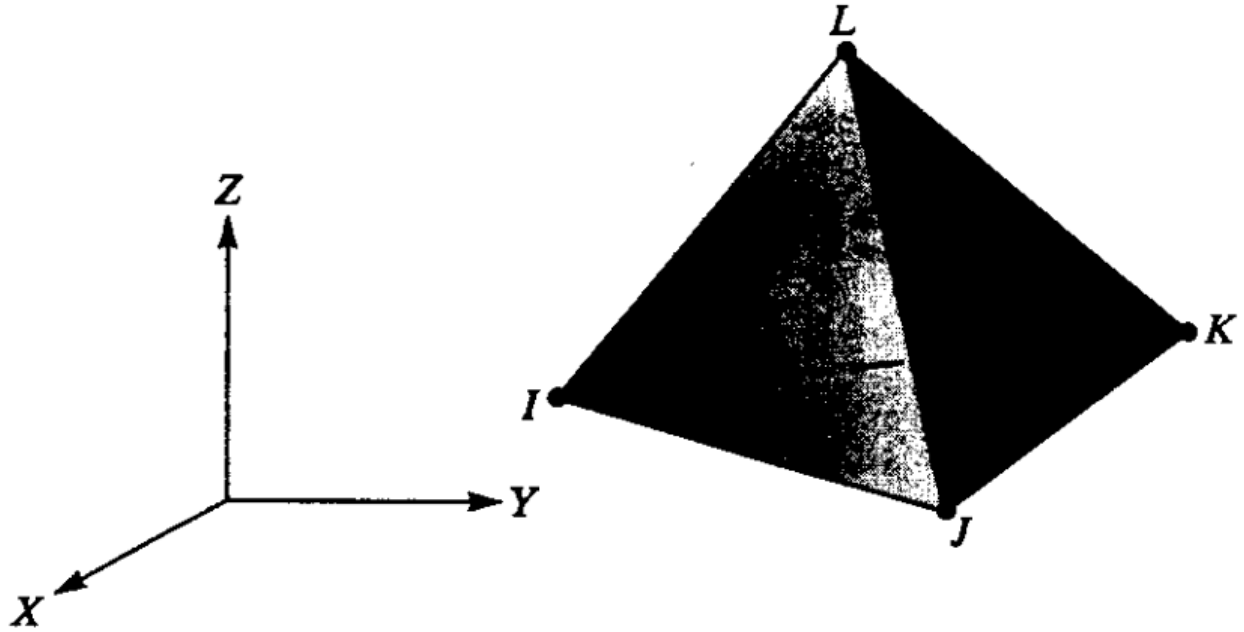
Figure 2.18: Four-node tetrahedral element, characterized by nodes I, J, K, and L. Each node has a starting position and a displacement, each defined in three dimensions. For instance, node I has initial position X_I, Y_I, and Z_I, and displacement u_I, v_I, and w_I. Reproduced from Moaveni (44).

Substituting each of the nodal displacement values into the displacement field equation yields a system of twelve equations and twelve unknowns (the twelve C_{mn} values):

$$u_I = C_{11} + C_{12}X_I + C_{13}Y_I + C_{14}Z_I$$
$$u_J = C_{11} + C_{12}X_J + C_{13}Y_J + C_{14}Z_J$$
$$\vdots$$
$$w_L = C_{31} + C_{32}X_L + C_{33}Y_L + C_{34}Z_L$$

(2.31)

Solving for these unknowns and regrouping the parameters yields the following expressions for the overall displacement field as a function of the nodal displacements:

$$u = S_I u_I + S_J u_J + S_K u_K + S_L u_L$$
$$v = S_I v_I + S_J v_J + S_K v_K + S_L v_L$$
$$w = S_I w_I + S_J w_J + S_K w_K + S_L w_L$$

(2.32)

The above relationship between the displacement field, shape functions, and nodal displacements can be expressed in matrix form as follows:

$$\{\mathbf{u}\}^T = \{u \quad v \quad w\}$$

$$[\mathbf{S}] = \begin{bmatrix} S_I & 0 & 0 & S_J & 0 & 0 & S_K & 0 & 0 & S_L & 0 & 0 \\ 0 & S_I & 0 & 0 & S_J & 0 & 0 & S_K & 0 & 0 & S_L & 0 \\ 0 & 0 & S_I & 0 & 0 & S_J & 0 & 0 & S_K & 0 & 0 & S_L \end{bmatrix} \tag{2.33}$$

$$\{\mathbf{U}\}^T = \{u_I \quad v_I \quad w_I \quad u_J \quad v_J \quad w_J \quad u_K \quad v_K \quad w_K \quad u_L \quad v_L \quad w_L\}$$

$$\{\mathbf{u}\} = [\mathbf{S}]\{\mathbf{U}\}$$

The nodal shape functions (S_I, S_J, S_K, S_L) are:

$$S_I = \frac{1}{6V}(a_I + b_I X + c_I Y + d_I Z)$$

$$\vdots \tag{2.34}$$

$$S_L = \frac{1}{6V}(a_L + b_L X + c_L Y + d_L Z)$$

The volume of the tetrahedron (V) is calculated as follows:

$$V = \frac{1}{6}\det \begin{vmatrix} 1 & X_I & Y_I & Z_I \\ 1 & X_J & Y_J & Z_J \\ 1 & X_K & Y_K & Z_K \\ 1 & X_L & Y_L & Z_L \end{vmatrix} \tag{2.35}$$

and the a, b, c, and d terms are calculated as follows:

$$a_I = \det \begin{vmatrix} X_J & Y_J & Z_J \\ X_K & Y_K & Z_K \\ X_L & Y_L & Z_L \end{vmatrix} \qquad b_I = -\det \begin{vmatrix} 1 & Y_J & Z_J \\ 1 & Y_K & Z_K \\ 1 & Y_L & Z_L \end{vmatrix}$$

$$c_I = \det \begin{vmatrix} X_J & 1 & Z_J \\ X_K & 1 & Z_K \\ X_L & 1 & Z_L \end{vmatrix} \qquad d_I = -\det \begin{vmatrix} X_J & Y_J & 1 \\ X_K & Y_K & 1 \\ X_L & Y_L & 1 \end{vmatrix} \tag{2.36}$$

The examples shown above for node I can be adapted to nodes J, K, and L by rotating subscripts using the right-hand rule, as shown below for a_J:

$$a_J = \det \begin{vmatrix} X_K & Y_K & Z_K \\ X_L & Y_L & Z_L \\ X_I & Y_I & Z_I \end{vmatrix} \tag{2.37}$$

The state of strain of the element is characterized by three normal strains and three shear strains, as follows:

$$\{\boldsymbol{\varepsilon}\}^T = \{\varepsilon_x \quad \varepsilon_y \quad \varepsilon_z \quad \gamma_{xy} \quad \gamma_{yz} \quad \gamma_{zx}\} \tag{2.38}$$

where the respective strain components are defined as follows:

$$\varepsilon_x = \frac{\delta u}{\delta x} \qquad\qquad \varepsilon_y = \frac{\delta v}{\delta y} \qquad\qquad \varepsilon_z = \frac{\delta w}{\delta z}$$

$$\gamma_{xy} = \frac{\delta u}{\delta y} + \frac{\delta v}{\delta x} \qquad \gamma_{yz} = \frac{\delta v}{\delta z} + \frac{\delta w}{\delta y} \qquad \gamma_{zx} = \frac{\delta w}{\delta x} + \frac{\delta u}{\delta z} \tag{2.39}$$

Normal strains represent the fractional change in distance between strain elements along each of the three principal axes, while shear strains represent the fractional change in shape of strain elements within the planes normal to each of the three principal axes.

The relationships between strain components and displacement field components above can be used to express the strain components in terms of the shape functions and nodal displacements, as follows:

$$
\begin{Bmatrix} \varepsilon_x \\ \varepsilon_y \\ \varepsilon_z \\ \gamma_{xy} \\ \gamma_{yz} \\ \gamma_{zx} \end{Bmatrix} =
\begin{bmatrix}
\frac{\delta S_I}{\delta x} & 0 & 0 & \frac{\delta S_J}{\delta x} & 0 & 0 & \frac{\delta S_K}{\delta x} & 0 & 0 & \frac{\delta S_L}{\delta x} & 0 & 0 \\
0 & \frac{\delta S_I}{\delta y} & 0 & 0 & \frac{\delta S_J}{\delta y} & 0 & 0 & \frac{\delta S_K}{\delta y} & 0 & 0 & \frac{\delta S_L}{\delta y} & 0 \\
0 & 0 & \frac{\delta S_I}{\delta z} & 0 & 0 & \frac{\delta S_J}{\delta z} & 0 & 0 & \frac{\delta S_K}{\delta z} & 0 & 0 & \frac{\delta S_L}{\delta z} \\
\frac{\delta S_I}{\delta y} & \frac{\delta S_I}{\delta x} & 0 & \frac{\delta S_J}{\delta y} & \frac{\delta S_J}{\delta x} & 0 & \frac{\delta S_K}{\delta y} & \frac{\delta S_K}{\delta x} & 0 & \frac{\delta S_L}{\delta y} & \frac{\delta S_L}{\delta x} & 0 \\
0 & \frac{\delta S_I}{\delta z} & \frac{\delta S_I}{\delta y} & 0 & \frac{\delta S_J}{\delta z} & \frac{\delta S_J}{\delta y} & 0 & \frac{\delta S_K}{\delta z} & \frac{\delta S_K}{\delta y} & 0 & \frac{\delta S_L}{\delta z} & \frac{\delta S_L}{\delta y} \\
\frac{\delta S_I}{\delta z} & 0 & \frac{\delta S_I}{\delta x} & \frac{\delta S_J}{\delta z} & 0 & \frac{\delta S_J}{\delta x} & \frac{\delta S_K}{\delta z} & 0 & \frac{\delta S_K}{\delta x} & \frac{\delta S_L}{\delta z} & 0 & \frac{\delta S_L}{\delta x}
\end{bmatrix}
\begin{Bmatrix} u_I \\ v_I \\ w_I \\ u_J \\ v_J \\ w_J \\ u_K \\ v_K \\ w_K \\ u_L \\ v_L \\ w_L \end{Bmatrix} \tag{2.40}
$$

Assessing each of the shape function derivatives yields the following set of equations for the strain components in terms of the nodal displacements and *a*, *b*, *c*, and *d* values:

$${\boldsymbol{\varepsilon}} = [\mathbf{B}]\{\mathbf{U}\} \tag{2.41}$$

where

$$[\mathbf{B}] = \frac{1}{6V}\begin{bmatrix} b_I & 0 & 0 & b_J & 0 & 0 & b_k & 0 & 0 & b_L & 0 & 0 \\ 0 & c_I & 0 & 0 & c_J & 0 & 0 & c_K & 0 & 0 & c_L & 0 \\ 0 & 0 & d_I & 0 & 0 & d_J & 0 & 0 & d_K & 0 & 0 & d_L \\ c_I & b_I & 0 & c_J & b_J & 0 & c_K & b_K & 0 & c_L & b_L & 0 \\ 0 & d_I & c_I & 0 & d_J & c_J & 0 & d_K & c_K & 0 & d_L & c_L \\ d_I & 0 & b_I & d_J & 0 & b_J & d_K & 0 & b_K & d_L & 0 & b_L \end{bmatrix} \tag{2.42}$$

and $\{\mathbf{U}\}$ is the 12-element vector of nodal displacements defined in Eq. 2.33. In a practical sense, given the nodal positions and displacements, the strain components can be found by calculating a, b, c, and d for each node, calculating the initial tetrahedral volume V, and using these to construct the matrix $\mathbf{B}$, without needing to directly calculate the shape functions.

2.6. References

1. Hogg JC, Timens W. The Pathology of Chronic Obstructive Pulmonary Disease. Annual Review of Pathology: Mechanisms of Disease. 2009;4(1):435–59.

2. Gelb AF, Licuanan J, Shinar CM, Zamel N. Unsuspected Loss of Lung Elastic Recoil in Chronic Persistent Asthma. CHEST. 2002 Mar 1;121(3):715–21.

3. Plantier L, Cazes A, Dinh-Xuan AT, Bancal C, Marchand-Adam S, Crestani B. Physiology of the lung in idiopathic pulmonary fibrosis. Eur. Respir Rev. 2018 Mar 31;27(147):170062.

4. Ware LB, Matthay MA. The Acute Respiratory Distress Syndrome. N Engl J Med. 2000 May 4;342(18):1334–49.

5. Light RB. Pulmonary pathophysiology of pneumococcal pneumonia. Semin Respir Infect. 1999 Sep;14(3):218–26.

6. Sundaram TA, Gee JC. Towards a model of lung biomechanics: pulmonary kinematics via registration of serial lung images. Medical Image Analysis. 2005 Dec 1;9(6):524–37.

7. Tustison NJ, Awate SP, Cai J, Altes TA, Miller GW, de Lange EE, et al. Pulmonary kinematics from tagged hyperpolarized helium-3 MRI. J Magn Reson Imaging. 2010 May;31(5):1236–41.

8. Cai J, Altes TA, Miller GW, Sheng K, Read PW, Mata JF, et al. MR grid-tagging using hyperpolarized helium-3 for regional quantitative assessment of pulmonary biomechanics and ventilation. Magn Reson Med. 2007 Aug;58(2):373–80.

9. Cai J, Miller GW, Altes TA, Read PW, Benedict SH, de Lange EE, et al. Direct measurement of lung motion using hyperpolarized helium-3 MR tagging. Int J Radiat Oncol Biol Phys. 2007 Jul 1;68(3):650–3.

10. Cai J, Sheng K, Benedict SH, Read PW, Larner JM, Mugler JP, et al. Dynamic MRI of grid-tagged hyperpolarized helium-3 for the assessment of lung motion during breathing. Int J Radiat Oncol Biol Phys. 2009 Sep 1;75(1):276–84.

11. Cui T, Miller GW, Mugler JP, Cates GD, Mata JF, de Lange EE, et al. An initial investigation of hyperpolarized gas tagging magnetic resonance imaging in evaluating deformable image registration-based lung ventilation. Med Phys. 2018 Dec;45(12):5535–42.

12. Hu L, Huang Q, Cui T, Duarte I, Miller GW, Mugler JP, et al. A hybrid proton and hyperpolarized gas tagging MRI technique for lung respiratory motion imaging: a feasibility study. Phys Med Biol. 2019 May 16;64(10):105019.

13. Owers-Bradley JR, Fichele MS, Bennattayalah A, McGloin CJS, Bowtell RW, Morgan PS, et al. MR tagging of human lungs using hyperpolarized 3He gas. Journal of Magnetic Resonance Imaging. 2003;17(1):142–6.

14. Woods JC, Yablonskiy DA, Chino K, Tanoli TSK, Cooper JD, Conradi MS. Magnetization tagging decay to measure long-range 3He diffusion in healthy and emphysematous canine lungs. Magnetic Resonance in Medicine. 2004;51(5):1002–8.

15. Wang C, Miller GW, Altes TA, Lange EE de, Jr GDC, Mugler JP. Time dependence of 3He diffusion in the human lung: Measurement in the long-time regime using stimulated echoes. Magnetic Resonance in Medicine. 2006;56(2):296–309.

16. Bachert P, Schad LR, Bock M, Knopp MV, Ebert M, Grobmann T, et al. Nuclear magnetic resonance imaging of airways in humans with use of hyperpolarized 3He. Magnetic Resonance in Medicine. 1996;36(2):192–6.

17. Zhao L, Albert MS. Biomedical imaging using hyperpolarized noble gas MRI: Pulse sequence considerations. Nuclear Instruments and Methods in Physics Research Section A: Accelerators, Spectrometers, Detectors and Associated Equipment. 1998 Jan 11;402(2):454–60.

18. Knoll F, Clason C, Diwoky C, Stollberger R. Adapted random sampling patterns for accelerated MRI. Magn Reson Mater Phy. 2011 Feb 1;24(1):43–50.

19. Zhang Y, Peterson BS, Ji G, Dong Z. Energy Preserved Sampling for Compressed Sensing MRI. Comput Math Methods Med. 2014;2014:546814.

20. Wu EX, Towe CW, Tang H. MRI cardiac tagging using a sinc-modulated RF pulse train. Magnetic Resonance in Medicine. 2002;48(2):389–93.

21. Altes TA, Powers PL, Knight-Scott J, Rakes G, Platts-Mills TAE, de Lange EE, et al. Hyperpolarized 3He MR lung ventilation imaging in asthmatics: Preliminary findings. Journal of Magnetic Resonance Imaging. 2001;13(3):378–84.

22. Wild JM, Teh K, Woodhouse N, Paley MNJ, Fichele S, de Zanche N, et al. Steady-state free precession with hyperpolarized 3He: Experiments and theory. Journal of Magnetic Resonance. 2006 Nov 1;183(1):13–24.

23. Bouchiat MA, Carver TR, Varnum CM. Nuclear Polarization in 3He Gas Induced by Optical Pumping and Dipolar Exchange. Phys Rev Lett. 1960 Oct 15;5(8):373–5.

24. Walker TG, Happer W. Spin-exchange optical pumping of noble-gas nuclei. Rev Mod Phys. 1997 Apr 1;69(2):629–42.

25. Mooney KE, Miller GW, Dolph PAM, Tobias WA, Nelyubin V, Singh J, et al. A 3-Liter Capacity, Hybrid Spin-Exchange 3He Polarizer for Medical Imaging. In: Proceedings of the 17th Annual Meeting of the International Society for Magnetic Resonance in Medicine. Honolulu, HI; 2009.

26. Lustig M, Donoho D, Pauly JM. Sparse MRI: The application of compressed sensing for rapid MR imaging. Magnetic Resonance in Medicine. 2007;58(6):1182–95.

27. Lustig M, Donoho DL, Santos JM, Pauly JM. Compressed Sensing MRI. IEEE Signal Processing Magazine. 2008 Mar;25(2):72–82.

28. Fletcher R, Reeves CM. Function minimization by conjugate gradients. The Computer Journal. 1964 Jan 1;7(2):149–54.

29. Cohen A, Daubechies I, Feauveau JC. Biorthogonal bases of compactly supported wavelets. Communications on Pure and Applied Mathematics. 1992;45(5):485–560.

30. Otsu N. A Threshold Selection Method from Gray-Level Histograms. IEEE Transactions on Systems, Man, and Cybernetics. 1979 Jan;9(1):62–6.

31. Lloyd S. Least squares quantization in PCM. IEEE Transactions on Information Theory. 1982 Mar;28(2):129–37.

32. Arthur D, Vassilvitskii S. k-means++: the advantages of careful seeding. In: Proceedings of the eighteenth annual ACM-SIAM symposium on Discrete algorithms. USA: Society for Industrial and Applied Mathematics; 2007. p. 1027–35. (SODA '07).

33. West CT, Slim N, Steele D, Chowdhury A, Brassett C. Are textbook lungs really normal? A cadaveric study on the anatomical and clinical importance of variations in the major lung fissures, and the incomplete right horizontal fissure. Clinical Anatomy. 2021;34(3):387–96.

34.   Amelon RE, Cao K, Reinhardt JM, Christensen GE, Raghavan ML. A measure for characterizing sliding on lung boundaries. Ann Biomed Eng. 2014 Mar;42(3):642–50.

35.   Choi J, Kim H. Implementation of time-efficient adaptive sampling function design for improved undersampled MRI reconstruction. Journal of Magnetic Resonance. 2016 Dec 1;273:47–55.

36.   De Troyer A, Borenstein S, Cordier R. Analysis of lung volume restriction in patients with respiratory muscle weakness. Thorax. 1980 Aug;35(8):603–10.

37.   Benditt JO, Boitano LJ. Pulmonary Issues in Patients with Chronic Neuromuscular Disease. Am J Respir Crit Care Med. 2013 May 15;187(10):1046–55.

38.   Sheers NL, Howard ME, Rochford PD, Rautela L, Chao C, McKim DA, et al. A Randomised Controlled Trial of Lung Volume Recruitment in Adults with Neuromuscular Disease. Ann Am Thorac Soc. 2023 Jun 30;

39.   Wang C, Altes TA, Mugler JP, Miller GW, Ruppert K, Mata JF, et al. Assessment of the lung microstructure in patients with asthma using hyperpolarized 3He diffusion MRI at two time scales: comparison with healthy subjects and patients with COPD. J Magn Reson Imaging. 2008 Jul;28(1):80–8.

40.   Huttinga NRF, Bruijnen T, van den Berg CAT, Sbrizzi A. Nonrigid 3D motion estimation at high temporal resolution from prospectively undersampled k-space data using low-rank MR-MOTUS. Magnetic Resonance in Medicine. 2021;85(4):2309–26.

41.   Miller Z, Torres L, Fain S, Johnson K. Motion Compensated Extreme MRI: Multi-Scale Low Rank Reconstructions for Highly Accelerated 3D Dynamic Acquisitions (MoCo-MSLR) [Internet]. arXiv; 2022 [cited 2023 Aug 31]. Available from: http://arxiv.org/abs/2205.00131

42.   Pauly J, Nishimura D, Macovski A. A k-space analysis of small-tip-angle excitation. Journal of Magnetic Resonance (1969). 1989 Jan 1;81(1):43–56.

43.   Brown RW, Cheng YCN, Haacke EM, Thompson MR, Venkatesan R. Magnetic Resonance Imaging: Physical Principles and Sequence Design. 2nd ed. John Wiley & Sons, Incorporated; 2014. 1161 p.

44.   Moaveni S. Finite Element Analysis: Theory and Application with ANSYS. 2nd ed. Upper Saddle River, N.J.: Prentice Hall; 1999. 527 p.

Chapter 3: Repeatability and lung volume dependence of 3D dissolved-phase ^{129}Xe lung MRI

3.1. Introduction

MRI of inhaled hyperpolarized xenon-129 (^{129}Xe) is a quantitative method for evaluating lung structure and function and characterizing pulmonary pathology (1–4). Upon inhalation, a measurable fraction of inhaled ^{129}Xe gas diffuses into and across the alveolar membrane and into the blood, identical to the uptake pathway followed by inhaled oxygen. This behavior can be observed and characterized using MRI due to the resulting chemical shifts of ^{129}Xe in two distinct compartments: 1) dissolved in the alveolar membrane and blood plasma (Mbr; shifted ~198 ppm from gas phase; also called "tissue/plasma," "TP," or "barrier" in previous studies) and 2) bound to hemoglobin in red blood cells (RBC; ~218 ppm) (5,6). The associated MRI technique, known as dissolved-phase ^{129}Xe MRI, can thus be used to derive spatially-resolved metrics characterizing gas uptake by the lung that cannot be obtained using CT or conventional MRI (6–8). Techniques including chemical shift saturation recovery (CSSR) spectroscopy (9,10), chemical-shift imaging (11), single-point Dixon imaging (8,12,13), and the multi-point Dixon-based hierarchical iterative decomposition of water and fat with echo asymmetry and least-squares estimation (IDEAL) (14–16) permit direct, simultaneous measurement of relative concentrations of ^{129}Xe in each compartment.

Quantitative signal ratios derived from such techniques, including Mbr/Gas, RBC/Gas, and RBC/Mbr, constitute self-normalized measures of gas uptake, and have been reported to display concordance with quantitative readouts of lung function derived from pulmonary function tests (17,18). These ratios demonstrate sensitivity to changes in lung function associated with disorders such as chronic obstructive pulmonary disease (COPD) (9,19–21) and idiopathic pulmonary fibrosis (IPF) (11,17,22–24). They are of clinical interest due to their ability to characterize particular aspects of pulmonary pathophysiology including emphysematous tissue destruction and perfusion limitation in COPD (19,20) and provide spatially-resolved assessments of disease-related deficits in lung function related to remodeling of the lung microstructure.

To be clinically useful, gas uptake metrics derived from dissolved-phase ^{129}Xe MRI must be reliable, repeatable, and reproducible. It has previously been observed that lung volume during measurement substantially impacts gas uptake metrics across and within healthy individuals (9,22,25,26). These results implicate lung-volume variability as an important contributor to gas uptake metric variability and potential confounder when separate measurements are compared. A comprehensive characterization of lung-volume dependence in both healthy and diseased individuals, including the impact of lung-volume variability on measurement repeatability, is therefore necessary to optimize the use and reliability of gas uptake metrics derived from dissolved-phase ^{129}Xe MRI. Prior work has examined reproducibility of Dixon-based Mbr/Gas, RBC/Gas, and RBC/Mbr image ratios in healthy volunteers (22,26,27) and patients with IPF (23), as well as reproducibility of these ratios and related metrics derived from CSSR spectroscopy in patients with COPD (27,28). However, relatively little work exists directly evaluating the impact of lung-volume variability on gas uptake reproducibility, and such work has been reported only in healthy individuals (26).

To address this knowledge gap, the purpose of the work presented in this chapter was therefore to characterize relationships between lung volume and Mbr/Gas, RBC/Gas, and RBC/Mbr ratios derived from IDEAL-based dissolved-phase ^{129}Xe MRI, assess and compare same-session repeatability of these measurements in participants with COPD versus healthy participants, and assess the impact of scan-to-scan volume differences on measurement variability.

3.2. Methods

3.2.1. Study participants

This prospective study complied with the Health Insurance Portability and Accountability Act and was approved by the University of Virginia institutional review board. All study participants provided written informed consent. Volunteers were solicited from the University of Virginia geographical area. Candidates were screened for respiratory infection within the prior two weeks and for history of congenital cardiac disease and were not invited for an in-person screening visit if either of these factors were present. Spirometry was performed at screening visit to determine forced expiratory volume in one second (FEV_1) and forced vital capacity (FVC). Inclusion criteria for healthy participants included FEV_1/FVC greater than 0.70, and inclusion criteria for

participants with COPD included age greater than 45 years and FEV_1/FVC less than 0.70. Healthy candidates were further screened for history of diagnosed pulmonary disease and for >10% increase in FEV_1 30-50 minutes after bronchodilator administration (in order to rule out undiagnosed asthma); candidates were not enrolled if either of these factors were present.

A total of 52 participants (21 with COPD and 31 healthy) were enrolled and underwent [129]Xe MRI for this study between March 2014 and December 2015 (Fig. 3.1, Table 3.1). After exclusion of three enrolled participants due to various study failures (Fig. 3.1), 49 participants (19 with COPD and 30 healthy) were included in the final analysis. Healthy participants were divided into older (≥44 years, 25 participants approximating inclusion criteria for participants with COPD) and young (≤27 years, five participants) categories.
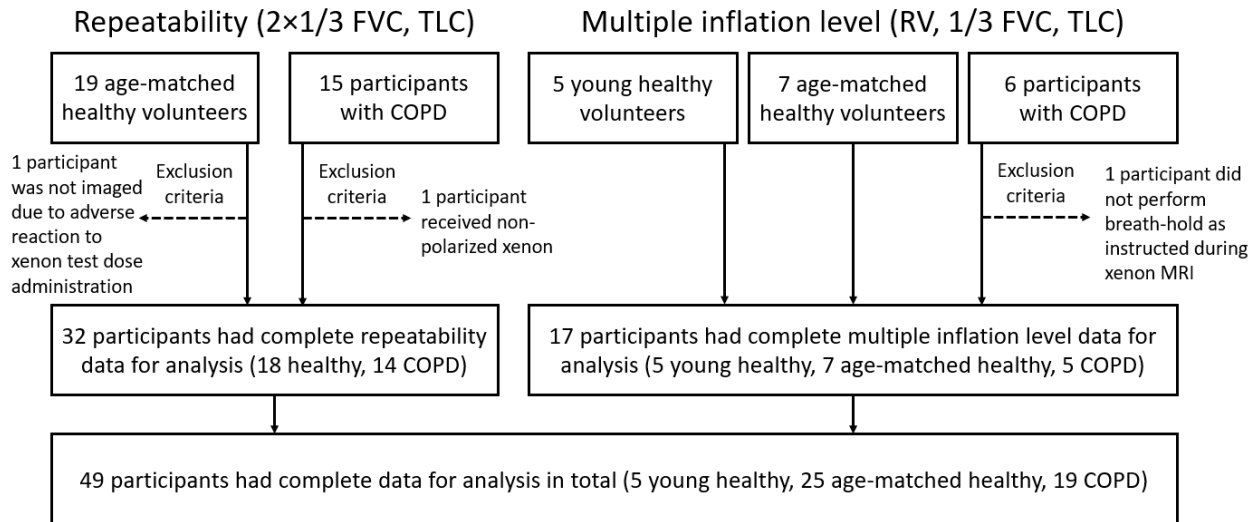
Figure 3.1: Study flowchart details exclusion criteria. Among 52 participants who entered the study protocol, one participant did not undergo imaging due to an adverse reaction to xenon test dose administration, one participant did not undergo full imaging due to xenon polarization failure, and data from one participant was excluded from analysis due to failure to perform breath-hold as instructed. COPD = chronic obstructive pulmonary disease, FVC = forced vital capacity, RV = residual volume, TLC = total lung capacity.

Parameter	Young Healthy	Older Healthy	COPD
Participants	5 (10.2%)	25 (51.0%)	19 (38.8%)
Sex			
Male	0	5	10
Female	5	20	9
Mean age (y)	23 (20−25)	58 (52−64)	65 (60−74)
Mean pack-years	0 (0−0)	0 (0−22)	35 (26−80)
FEV$_1$ (%-pred.)	103 (95−106)	103 (93−110)	67 (43−86)
FEV$_1$/FVC (%)	83 (82−86)	77 (74−80)	60 (52−64)
FVC (L)	4.0 (3.8−4.2)	3.4 (3.2−4.0)	3.8 (2.8−4.4)
TLC (L)	5.4 (5.1−5.6)	5.6 (5.1−6.5)	6.9 (5.1−8.3)

Table 3.1: Demographics and pulmonary metrics for dissolved-phase ^{129}Xe MRI study participants. Values are medians with interquartile ranges in parentheses, except for participants, which are numbers of participants with percentages of the total participant sample in parentheses. All participants with COPD were former or current smokers. Four of the older healthy participants were current smokers, and five of the older healthy participants were former smokers. Pack-years = number of cigarette packs smoked per day multiplied by years of smoking, %-pred = percent predicted.

3.2.2. Lung inflation levels during imaging

Thirty-two total participants (14 with COPD and 18 older healthy) received repeated dissolved-phase xenon scans at a target inflation level of residual volume plus one-third FVC (RV+FVC/3), with 29 of these participants (14 with COPD and 15 older healthy) also receiving one scan at a target inflation level of total lung capacity (TLC) and one of the remaining three participants receiving a third scan at a target inflation level of RV+FVC/3. The remaining 17 participants (five with COPD, seven older healthy, and five young healthy) received single dissolved-phase xenon scans at each of three target inflation levels: TLC, RV+FVC/3, and residual volume (RV). For the 32 participants that received repeated scans at RV+FVC/3, hereafter referred to as repeatability participants, the order of the three scans was typically as follows: (1) first RV+FVC/3, (2) TLC, (3) second RV+FVC/3. For the 17 participants that received scans at all three target inflation levels, hereafter referred to as multiple-inflation-level participants, the order of the three scans was varied to reduce potential bias. Table 3.2 provides the exact distribution of scan ordering across all imaging sessions.

Order #	Scan 1	Scan 2	Scan 3	# of participants
1	RV	RV+FVC/3	TLC	3
2	RV	TLC	RV+FVC/3	6
3	RV+FVC/3	RV	TLC	3
4	RV+FVC/3	TLC	RV	1
5	TLC	RV	RV+FVC/3	0
6	TLC	RV+FVC/3	RV	4
7	RV+FVC/3	RV+FVC/3	None	2
8	RV+FVC/3	RV+FVC/3	RV+FVC/3	1
9	RV+FVC/3	RV+FVC/3	TLC	1
10	RV+FVC/3	TLC	RV+FVC/3	26
11	TLC	RV+FVC/3	RV+FVC/3	2

Table 3.2: Chronological order of dissolved-phase ^{129}Xe MR scans within individual imaging sessions. Rows 1-6 correspond to multiple-inflation-level participants, while rows 7-11 correspond to repeatability participants. Repeatability participants in row 7 received only two dissolved-phase ^{129}Xe scans, while all others received three dissolved-phase ^{129}Xe scans. The third RV+FVC/3 scan of the participant in row 8 was used for lung volume analysis, but not repeatability analysis. FVC = forced vital capacity, RV = residual volume, TLC = total lung capacity.

3.2.3. ^{129}Xe polarization and delivery

Isotopically enriched xenon gas (87% ^{129}Xe) was polarized to approximately 40% via spin-exchange optical pumping using a prototype commercial system (XeBox-E10, Xemed, LLC, Durham, NH) (29,30). For each dissolved-phase scan, 1.0 L of hyperpolarized ^{129}Xe was dispensed into a plastic bag for inhalation (Tedlar plastic bag; Jensen Inert Products, Coral Springs, FL).

All breathing maneuvers were practiced without ^{129}Xe administration while participants were inside the scanner bore prior to ^{129}Xe MRI in order to familiarize participants with study procedures. During ^{129}Xe MRI, participants were instructed to take a large, deep breath in until reaching full lung capacity, exhale as far as possible to minimum lung capacity, repeat this inhalation/exhalation procedure once, and then inhale the administered gas dose from residual volume. Dose inhalation procedures were specific to each target inflation level as follows:

- RV: Participants inhaled the full contents of a bag containing 1 L of ^{129}Xe, followed by a small "sip" of room air to ensure as much ^{129}Xe as possible made its way into the lungs. Participants then exhaled back to RV.
- RV+FVC/3: Participants simultaneously inhaled the full contents of two bags: one containing 1 L of ^{129}Xe, and another containing medical-grade nitrogen. The volume of nitrogen was chosen based on participant spirometry, such that the total volume of the bag contents would match one-third of FVC volume for each participant.
- TLC: Participants inhaled the full contents of a bag containing 1 L of ^{129}Xe and then inhaled room air to maximum capacity.

After completing the above procedure for the corresponding target inflation level, participants then held their breath for the duration of image acquisition, spanning up to 15 seconds. Participants were monitored by study coordinators during this procedure to verify compliance.

All ^{129}Xe doses administered during the study were spaced apart by at least two minutes. Participants were monitored for transient central nervous system symptoms (primarily lightheadedness and dizziness), and additional time between doses was given when necessary to ensure participants returned to baseline prior to the next dose.

Participants' O_2 saturation was taken at baseline prior to the start of xenon dosing, and was monitored continuously throughout the study. No participants recorded O_2 saturation lower than 80% at any point during the study. Medical-grade O_2 was readily available in the MRI scanner room, and administered if deemed necessary by study coordinators. Out of the 49 participants studied, one participant (a 66-year-old healthy female volunteer) received supplemental doses of 2–4 L of pure O_2 between each ^{129}Xe dose.

3.2.4. ^{129}Xe and proton MRI

MRI studies were performed using a 1.5T commercial whole-body MRI scanner (Avanto; Siemens Medical Solutions, Malvern, PA) and a flexible, proton-blocked, vest-shaped ^{129}Xe quadrature transmit/receive radiofrequency coil (Clinical MR Solutions, Brookfield, WI). A ^{129}Xe calibration scan was performed for each participant using an inhaled gas mixture containing ~200 mL of hyperpolarized ^{129}Xe to determine optimal transmitter voltage and ^{129}Xe central frequency.

Simultaneous dissolved-phase and gas-phase xenon MRIs were acquired using a multi-echo three-dimensional (3D) radial pulse sequence described previously (15). Same-breath-hold proton MRIs were acquired immediately after each [129]Xe scan, using a three-fold under-sampled spoiled gradient-echo 3D Cartesian pulse sequence. Separate fully-sampled proton images were acquired at TLC in all participants. Table 3.3 lists pulse sequence parameters and scan resolutions for [129]Xe and proton MRI.

	[129]Xe			Proton
	Repeatability (RV+FVC/3)	Repeatability (TLC)	Multiple-inflation-level	
Resolution (mm^3)	7.6×7.6×17	10.9×10.9×17	15.2×15.2×17.6	5.2×3.9×6.0
Flip angle	23° (dissolved-phase) 0.4° (gas-phase)			10°
TE (ms)	0.74/2.36/3.98 (dissolved-phase) 0.74/2.36 (gas-phase)			0.78
TR (ms)	19			1.8

Table 3.3: Pulse sequence parameters for [129]Xe and proton MRI. For [129]Xe scans, two different excitation/readout cycles were interleaved. The first row of flip angle and TE corresponds to the dissolved-phase excitation and readout, while the second row of flip angle and TE corresponds to the gas-phase excitation and readout.

3.2.5. Image analysis

Under-sampled dissolved-phase xenon MR images were reconstructed using the quadratic penalized weighted-least-squares via preconditioned conjugate gradients algorithm (31), and the Mbr and RBC dissolved-phase signal components were separated using the hierarchical IDEAL method (9,14,15). Reconstructed xenon images were used to calculate Mbr/Gas, RBC/Gas, and RBC/Mbr signal ratios at each ventilated pixel location, and whole-lung mean values for each ratio were calculated for each dissolved-phase scan.

Under-sampled proton MR images were reconstructed using a compressed sensing algorithm solved via non-linear conjugate gradients (15,32). Lung volumes were determined by segmenting proton images using a deep learning-based method from the ANTsPyNet toolbox, with manual intervention applied in selected cases when necessary (33).

Preliminary analysis of lung volume and gas uptake data suggested an inverse relationship between lung volume and each of Mbr/Gas and RBC/Gas. The following relationship was initially theorized for each of these two ratios:

$$R = C \cdot V^{-\alpha} \tag{3.1}$$

where R is the ratio in question for a given measurement, V is the lung volume during measurement, and C and α are arbitrary constants to be determined via fitting of the equation above to subject data. This formulation was developed with an eye toward using the $V^{-\alpha}$ term as a proxy for alveolar surface-to-volume ratio, with α allowed to float in order to represent different models of alveolar expansion and shape change with lung volume change (34). (For instance, $\alpha = \frac{2}{3}$ would correspond to balloon-like inflation and deflation, and $\alpha = 1$ would correspond to recruitment of alveoli upon inflation and derecruitment and collapse of alveoli upon deflation.)

For the final analysis used in this study, Eq. 3.1 was modified to a relative-difference formulation by differentiating each side of the equation and assuming $C = 1$. This formulation quantified the effect of scan-to-scan lung-volume changes on measured signal ratios by performing pairwise comparisons of different scans within each participant. The following linear relationship was therefore assumed between the relative signal-ratio difference and relative volume difference between any two such scans:

$$\frac{R_2 - R_1}{(R_1 + R_2)/2} = -\alpha \cdot \frac{V_2 - V_1}{(V_1 + V_2)/2} \tag{3.2}$$

where R_1 (R_2) and V_1 (V_2) represent the mean signal ratio and lung volume, respectively, from the chronologically earlier (later) of the two scans, and α represents the slope of the linear correlation. A differential relationship of this form was previously used by Hahn et al. in a study of inter-visit reproducibility in healthy volunteers (26). Because three different scans of each participant were performed in this study, three scan pairings per participant were possible for each signal ratio, except in the two repeatability participants that only received two RV+FVC/3 scans, for which only one scan pairing was possible. A total of 143 scan pairings were generated from the 49 participants. The slope α was determined for each signal ratio within each participant group by performing a least-squares fit of all such pairwise comparisons to Eq. 3.2.

94

The resulting groupwise values of α were finally used to correct for volume contributions to signal ratios measured in COPD and older healthy groups. For each of the three nominal inflation levels, the mean of all volume measurements made at a given inflation level across all COPD and older healthy participants was calculated. This volume was then used as a reference volume for the corresponding inflation level, and all mean ratio measurements taken at the corresponding inflation level were projected to that volume using the corresponding value of α determined from the differential volume analysis described above. This was done for each scan by setting V_1 equal to the actual scan volume for a given scan, V_2 equal to the reference volume for that inflation level, R_1 equal to one of the three signal ratios for that scan, and solving for R_2 in Eq. 3.2.

3.2.6. Statistical analysis

Two-way random, single-measure, absolute-agreement intraclass correlation coefficient (ICC) (34) and coefficient of variation (CV) were used to quantify repeatability of lung volumes and signal ratios. ICC values were classified as excellent (>0.9), good (0.75-0.9), moderate (0.5-0.75), or poor (<0.5) (35). Bland-Altman plots were also used to assess repeatability of volumes and ratios, and traditional Bland-Altman measures of agreement – mean inter-measurement discrepancy, lower and upper limits of agreement (LoAs) for measurements, and 95% confidence intervals (CIs) of these quantities – were calculated, with $p < 0.05$ indicating a statistically significant difference between mean discrepancy and zero. Spearman correlation coefficients were calculated for $(\Delta R)/R_{avg}$ and $(\Delta V)/V_{avg}$ for each of the three signal ratios, and statistical significance was established at the $p = 0.05$ level, with p values determined using an F test. Wilcoxon rank-sum tests were performed to assess differences in volume, signal ratios, and projected ratios at reference volumes between COPD and older healthy groups. Bonferroni correction for multiple comparisons was applied to the 24 Wilcoxon rank-sum tests performed on these quantities, with $p < 0.05/24 \approx 0.0021$ thus taken to indicate a statistically significant difference between the two groups. Further description of the individual statistical methods used in the study is provided in the Appendix.

3.3. Results

3.3.1. ^{129}Xe and proton MRI

Representative proton images and xenon uptake ratio maps are shown in Fig. 3.2. Mean ratio values varied by less than 10% in representative repeatability scans in which lung volume was tightly repeated between scans (Fig. 3.2a). Scans at three different target inflation levels (Fig. 3.2b) showed increased ratios with decreased lung volume, particularly for Mbr/Gas and RBC/Gas.
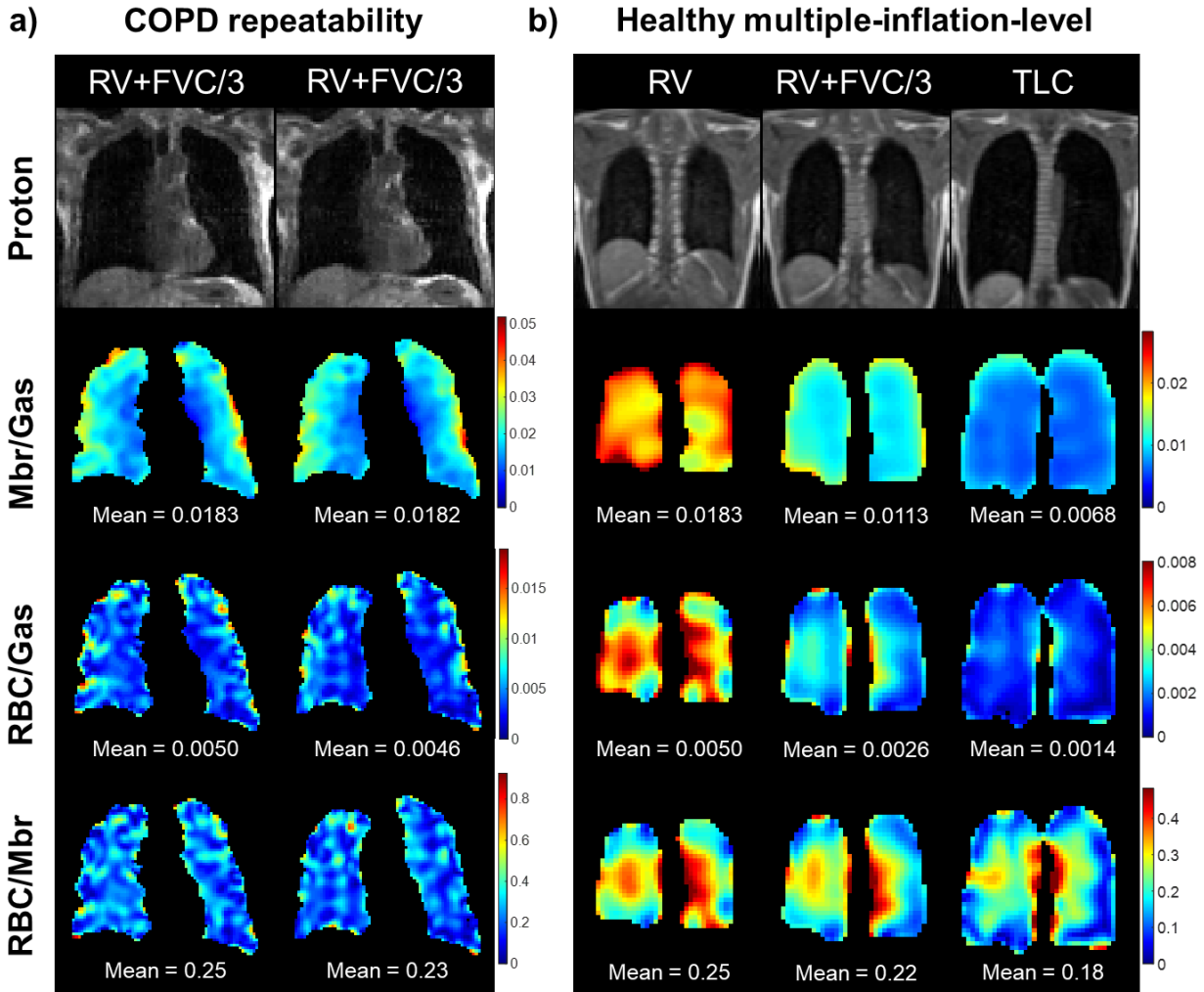
Figure 3.2: **a)** Representative repeated proton, Mbr/Gas, RBC/Gas, and RBC/Mbr [129]Xe images from a 57-year-old male with COPD. Both scans were performed at a target inflation level of RV+FVC/3. All three ratios differed by less than 10% across the two repeated scans. **b)** Representative multiple-inflation-level proton, Mbr/Gas, RBC/Gas, and RBC/Mbr [129]Xe images from a healthy 52-year-old female. Scans were performed at target inflation levels of RV, RV+FVC/3, and TLC, respectively, from left to right. Ratios increased with decreasing lung volume across the three scans, particularly Mbr/Gas and RBC/Gas.

3.3.2. Statistical analysis of repeatability

Fig. 3.3 shows Bland-Altman plots of whole-lung mean Mbr/Gas, RBC/Gas, and RBC/Mbr ratios in each participant that received repeated RV+FVC/3 scans. None of the three ratios displayed a significant non-zero mean discrepancy between repeated scans (Fig. 3.3, Table 3.4). As shown in Table 3.5, Mbr/Gas and RBC/Mbr displayed good repeatability across all participants, while RBC/Gas displayed moderate repeatability (ICC=0.88, 95% CI: [0.76, 0.94]

for Mbr/Gas; 0.71 [0.48, 0.84] for RBC/Gas; and 0.88 [0.76, 0.94] for RBC/Mbr). RBC/Mbr appeared to display the smallest CV of the three ratios (CV=11.4% [8.7, 14.0] for Mbr/Gas, 13.0% [10.0, 16.0] for RBC/Gas, 7.2% [5.5, 8.9] for RBC/Mbr). CVs for the three measures were generally similar between older healthy participants (CV≤14.1%) and participants with COPD (CV≤11.4%).
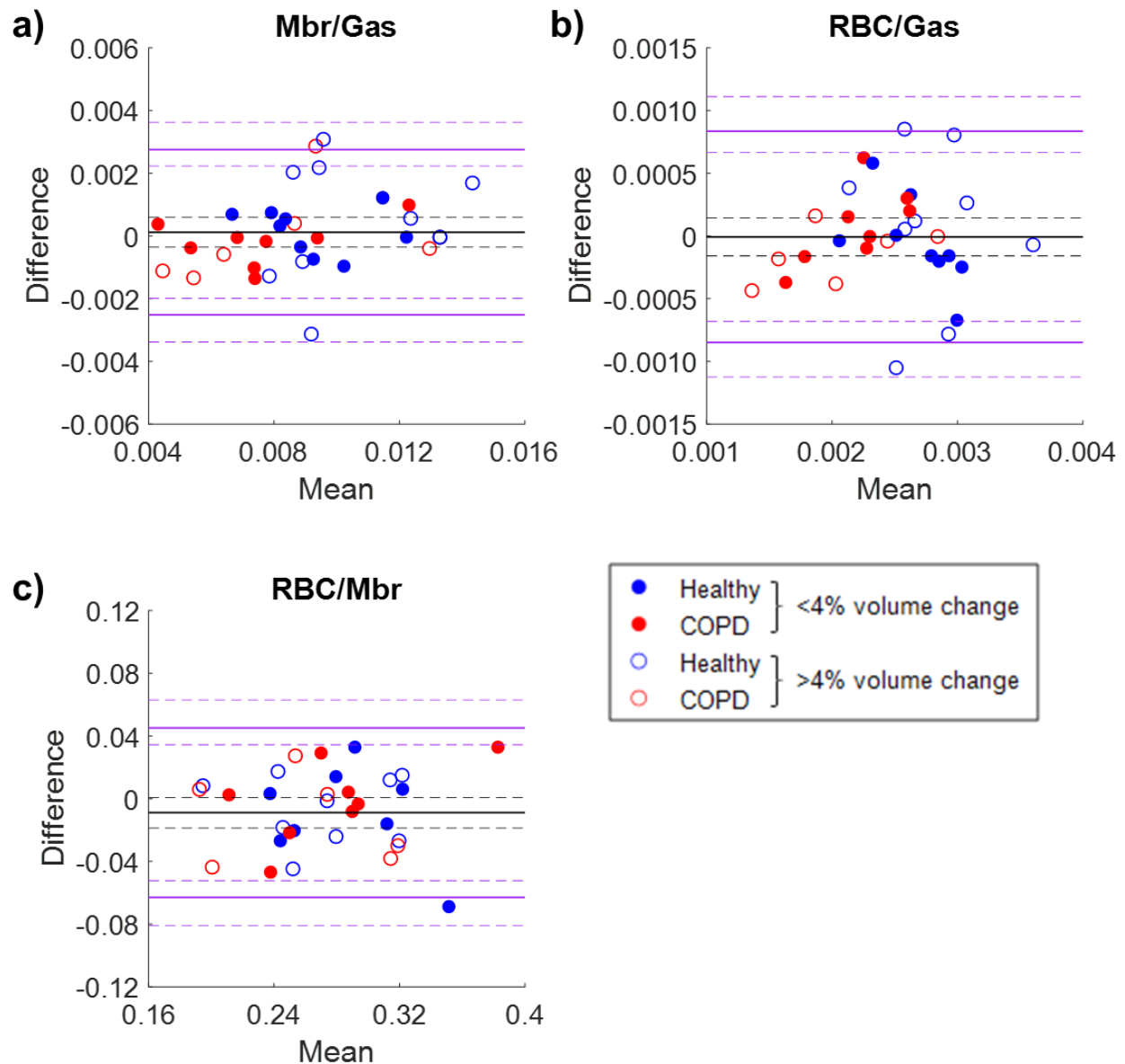
Figure 3.3: Bland-Altman plots for repeatability analysis of **a)** Mbr/Gas, **b)** RBC/Gas, and **c)** RBC/Mbr, in healthy participants and in participants with COPD that received repeated dissolved-phase ^{129}Xe scans at RV+FVC/3 (n = 32). Solid black lines indicate mean discrepancies, dashed black lines indicate 95% confidence intervals of mean discrepancies, solid purple lines indicate lower 2.5% and upper 97.5% limits of agreement, and dashed purple lines indicate 95% confidence intervals for limits of agreement.

	Mean Discrepancy	Lower LoA	Upper LoA	p
Mbr/Gas $\times 10^3$	0.12 [-0.35, 0.60]	-2.51 [-3.38, -1.99]	2.76 [2.23, 3.62]	0.60
RBC/Gas $\times 10^3$	-0.01 [-0.16, 0.15]	-0.85 [-1.13, -0.68]	0.84 [0.67, 1.11]	0.93
RBC/Mbr	-0.01 [-0.02, 0.00]	-0.06 [-0.08, -0.05]	0.05 [0.03, 0.06]	0.07
Volume (RV+FVC/3, L)	0.00 [-0.18, 0.18]	-0.98 [-1.30, -0.78]	0.98 [0.78, 1.30]	0.99
Volume (TLC, L)	-0.04 [-0.15, 0.07]	-0.63 [-0.83, -0.51]	0.54 [0.42, 0.75]	0.45

Table 3.4: Mean discrepancies and 95% LoAs for lung volumes and gas uptake ratios. Data in brackets represent 95% confidence intervals.

		n	Mbr/Gas		RBC/Gas		RBC/Mbr	
			ICC	CV (%)	ICC	CV (%)	ICC	CV (%)
All scan pairs	All	32	0.88 [0.76, 0.94]	11.4 [8.7, 14.0]	0.71 [0.48, 0.84]	13.0 [10.0, 16.0]	0.88 [0.76, 0.94]	7.2 [5.5, 8.9]
	Healthy	18	0.78 [0.52, 0.91]	11.7 [8.1, 15.3]	0.37 [-0.12, 0.71]	14.1 [9.8, 18.4]	0.88 [0.70, 0.95]	6.8 [4.7, 8.9]
	COPD	14	0.92 [0.77, 0.97]	11.0 [7.1, 14.8]	0.81 [0.50, 0.94]	11.4 [7.4, 15.4]	0.88 [0.67, 0.96]	7.6 [4.9, 10.3]
Scan pairs with volume difference >4%	All	15	0.83 [0.57, 0.94]	15.4 [10.3, 20.5]	0.70 [0.30, 0.89]	15.7 [10.5, 21.0]	0.86 [0.65, 0.95]	7.2 [4.7, 9.7]
	Healthy	9	0.70 [0.16, 0.92]	15.7 [9.0, 22.5]	0.31 [-0.37, 0.78]	17.8 [10.2, 25.3]	0.87 [0.57, 0.97]	6.1 [3.3, 8.8]
	COPD	6	0.90 [0.53, 0.99]	14.9 [7.0, 22.8]	0.90 [0.51, 0.98]	12.3 [5.7, 18.8]	0.87 [0.40, 0.98]	8.7 [4.0, 13.5]
Scan pairs with volume difference <4%	All	17	0.95 [0.87, 0.98]	6.3 [4.2, 8.3]	0.73 [0.40, 0.89]	10.0 [6.8, 13.3]	0.88 [0.70, 0.95]	7.1 [4.8, 9.4]
	Healthy	9	0.92 [0.72, 0.98]	5.6 [3.1, 8.1]	0.58 [-0.04, 0.88]	9.5 [5.3, 13.7]	0.87 [0.56, 0.97]	7.5 [4.1, 10.8]
	COPD	8	0.96 [0.82, 0.99]	7.0 [3.7, 10.3]	0.69 [0.09, 0.93]	10.7 [5.7, 15.6]	0.89 [0.60, 0.98]	6.7 [3.5, 9.8]

Table 3.5: Repeatability measures for paired measurements of ^{129}Xe gas uptake at target lung volume of RV+FVC/3. Data in brackets represent 95% confidence intervals.

Within-participant repeatability of RBC/Mbr did not improve when lung volume differences (ΔV) larger than 4% were excluded, and was good in both cases (ICC=0.88 [0.70, 0.95] when ΔV<4% vs. 0.86 [0.65, 0.95] when ΔV>4%). By contrast, within-participant repeatability of Mbr/Gas was excellent in participants whose lung volume was better repeated, but only good in participants whose lung volume was repeated less well (ICC=0.95 [0.87, 0.98] when ΔV<4% vs. 0.83 [0.57, 0.94] when ΔV>4%).

Lung volumes achieved during each of the RV+FVC/3 repeatability scans (Fig. 3.4, Table 3.6) displayed excellent within-participant repeatability (ICC=0.90 [0.81, 0.95]), as did lung volumes measured in separate TLC scans of each repeatability participant (ICC=1.00 [0.99, 1.00]).

Neither lung volume displayed a significant non-zero mean discrepancy between repeated scans (Fig. 3.4, Table 3.4). CV appeared to be lower for scans at TLC than at RV+FVC/3 across all repeatability participants (CV=4.1 [3.1, 5.1] at TLC vs. =7.4 [5.6, 9.1] at RV+FVC/3) and also within the COPD group (CV=3.5 [2.2, 4.7] at TLC vs. 7.8 [5.0, 10.6] at RV+FVC/3).
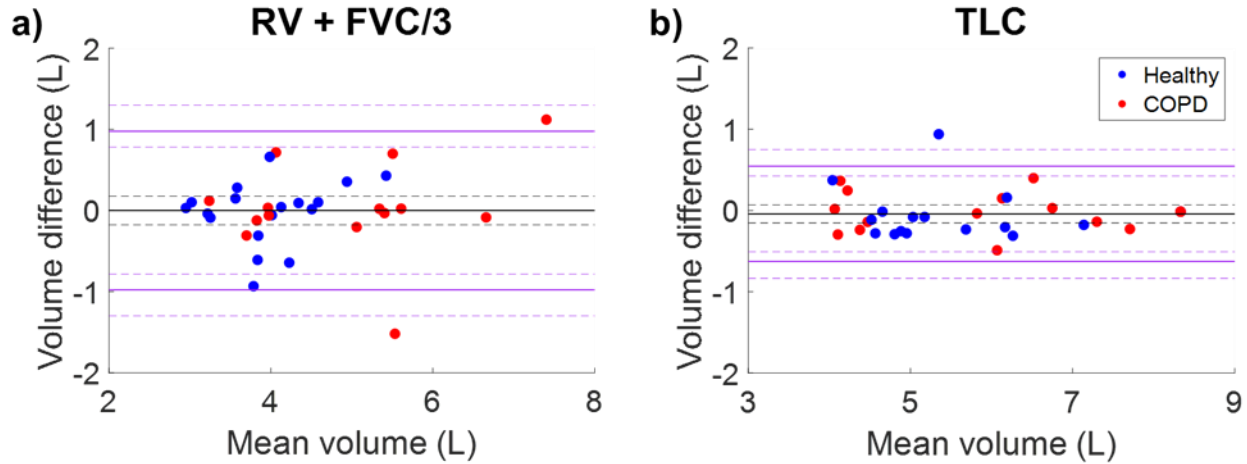
Figure 3.4: **a)** Bland-Altman plot of lung volume differences between repeated dissolved-phase [129]Xe MRI scans at RV+FVC/3, in healthy repeatability participants (n = 18) and repeatability participants with COPD (n = 14). **b)** Bland-Altman plot of lung volume differences between dissolved-phase [129]Xe MRI scan at TLC and scan at TLC without xenon inhalation, in healthy repeatability participants (n = 15) and repeatability participants with COPD (n = 14). The same participants shown in a) are shown in b), except for three healthy participants that did not receive a dissolved-phase scan at TLC. Solid black lines indicate mean discrepancies, dashed black lines indicate 95% confidence intervals of mean discrepancies, solid purple lines indicate lower 2.5% and upper 97.5% limits of agreement, and dashed purple lines indicate 95% confidence intervals for limits of agreement.

		n	ICC	CV (%)
RV+FVC/3	**All**	32	0.90 [0.81, 0.95]	7.4 [5.6, 9.1]
	Healthy	18	0.84 [0.64, 0.94]	7.0 [4.8, 9.3]
	COPD	14	0.89 [0.70, 0.96]	7.8 [5.0, 10.6]
TLC	**All**	29	1.00 [0.99, 1.00]	4.1 [3.1, 5.1]
	Healthy	15	1.00 [0.99, 1.00]	4.6 [3.0, 6.2]
	COPD	14	1.00 [0.99, 1.00]	3.5 [2.2, 4.7]

Table 3.6: Repeatability measures for lung volumes at RV+FVC/3 and TLC. Data in brackets represent 95% confidence intervals.

3.3.3. Statistical analysis of lung volume dependence

Gas uptake measurements performed at target volumes of RV, RV+FVC/3, and TLC revealed a clear dependence on lung volume (Fig. 3.5, Table 3.7). Across all participants, Mbr/Gas and RBC/Gas ratios increased as lung volume decreased (Fig. 3.5a,b), with the slope of dependence highest at lower lung volumes. Comparatively little dependence on lung volume is observed in the plot of RBC/Mbr ratios (Fig. 3.5c). Fits of paired data within individuals to Eq. 3.2 revealed a strong linear correlation between relative ratio difference and relative volume difference for Mbr/Gas ($r = -0.97$, Fig. 3.5d) and RBC/Gas ($r = -0.93$, Fig. 3.5e), with RBC/Gas exhibiting a slightly greater dependence on volume change ($\alpha = 1.74$) than Mbr/Gas ($\alpha = 1.38$). Relative volume change was also correlated with relative ratio change for RBC/Mbr, but less strongly ($r = -0.68$, Fig. 3.5f) and with a much weaker dependence on volume change ($\alpha = 0.44$). The slopes of all three volume dependencies, represented by α in Eq. 3.2, were consistent across participant subgroups spanning a wide range of ages and presence of disease (Table 3.7). The slope of the RBC/Mbr volume dependence was approximately equal to the difference between the slopes for the other two ratios, which was expected since the three ratio combinations are interdependent.

	n	Mbr/Gas		RBC/Gas		RBC/Mbr	
		α	r	α	r	α	r
All (49)	143	1.38 [1.32, 1.44]	-0.97 [-0.97, -0.95]	1.74 [1.62, 1.85]	-0.93 [-0.95, -0.90]	0.44 [0.36, 0.52]	-0.68 [-0.76, -0.58]
Young healthy (5)	15	1.33 [1.27, 1.40]	-1.00 [-1.00, -0.99]	1.71 [1.58, 1.85]	-0.99 [-1.00, -0.96]	0.50 [0.38, 0.63]	-0.91 [-0.97, -0.76]
Older healthy (25)	71	1.42 [1.34, 1.50]	-0.98 [-0.99, -0.96]	1.76 [1.59, 1.92]	-0.93 [-0.96, -0.89]	0.40 [0.29, 0.52]	-0.66 [-0.77, -0.51]
COPD (19)	57	1.37 [1.21, 1.53]	-0.92 [-0.95, -0.86]	1.72 [1.41, 2.04]	-0.83 [-0.89, -0.72]	0.40 [0.18, 0.62]	-0.46 [-0.64, -0.23]

Table 3.7: Fitted linear slopes and Spearman correlation coefficients of relative difference relationships between [129]Xe gas uptake metrics and lung volume. Data in brackets represent 95% confidence intervals. Slopes are represented by α, while Spearman correlation coefficients are represented by r. All linear fits in all participant categories were significant ($p < 0.001$). n represents the total number of within-participant scan pairs analyzed in each category, with each participant contributing either one or three scan pairs to the total, depending on how many scans were performed in each individual.
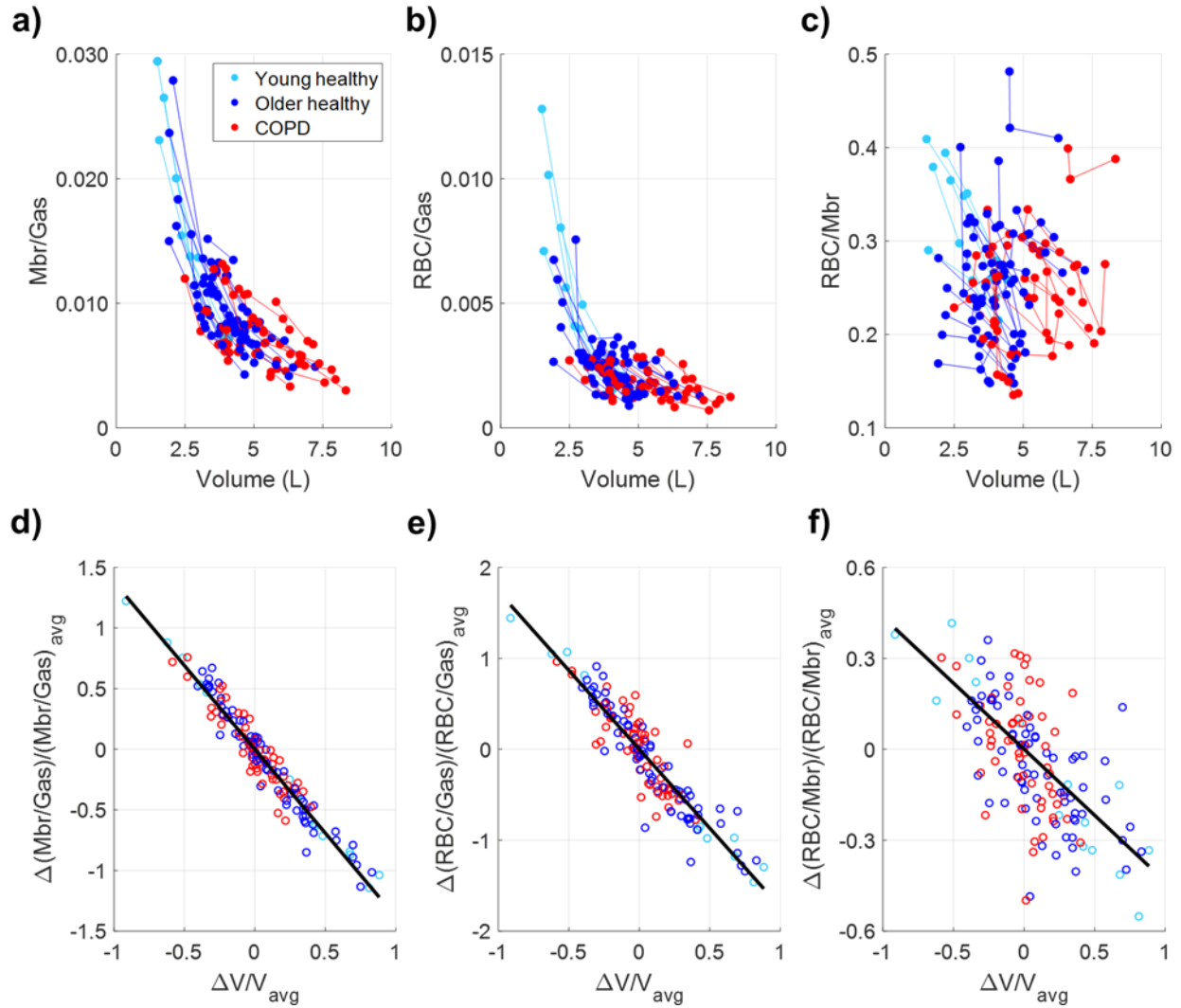
Figure 3.5: **a)** Mbr/Gas, **b)** RBC/Gas, and **c)** RBC/Mbr vs. lung volume. Thin lines connect scans from the same participant. **d)** Relative Mbr/Gas differences, **e)** relative RBC/Gas differences, and **f)** relative RBC/Mbr differences vs. relative volume differences ($\Delta V/V_{avg}$). Each data point in d), e), and f) corresponds to a pair of points from the same participant in a), b), and c), respectively. Lines in d), e), and f) are linear fits to Eq. 3.2, with corresponding slopes and linear correlation coefficients shown in the first row of Table 3.7.

Lung volumes achieved during dissolved-phase ^{129}Xe MRI scans (Fig. 3.6a, Tables 3.8 and 3.9) were higher for participants with COPD than older healthy participants at 1/3 FVC (p=0.001), consistent with emphysema-related hyperinflation. This trend persisted when lung volumes measured at RV+FVC/3 were normalized to TLC (p<0.001; Fig. 3.6b). Mean lung volumes across all participants with COPD and older healthy participants were 3.2 L at RV, 4.3 L at RV+FVC/3, and 5.4 L at TLC.

Compared with the older healthy group, the COPD group had lower mean Mbr/Gas (p=0.001) and RBC/Gas (p<0.001) ratios at RV+FVC/3 (Fig. 3.6, Tables 3.8 and 3.9). However, after correcting for volume contribution to measured ratio values in each participant, neither of these differences remained significant (p=0.23 for Mbr/Gas, 0.09 for RBC/Gas). No evidence of groupwise differences in RBC/Mbr ratios was found at any of the three inflation levels, with or without lung volume correction.

c)

d)

e)

f)
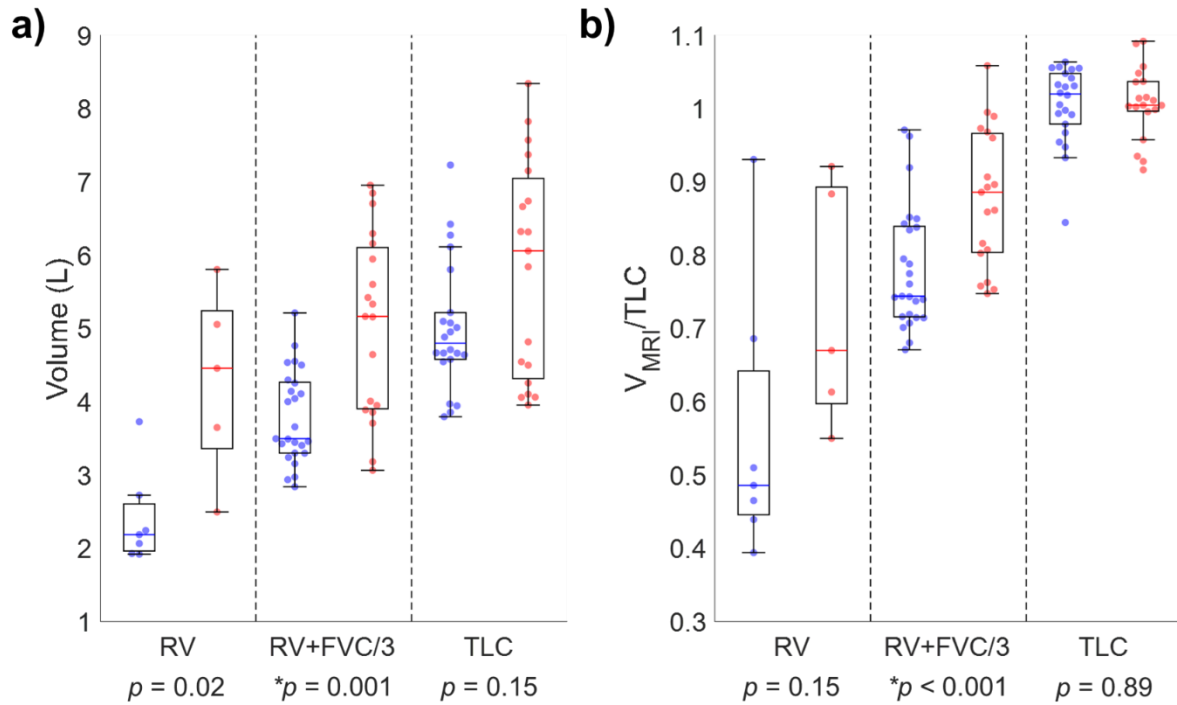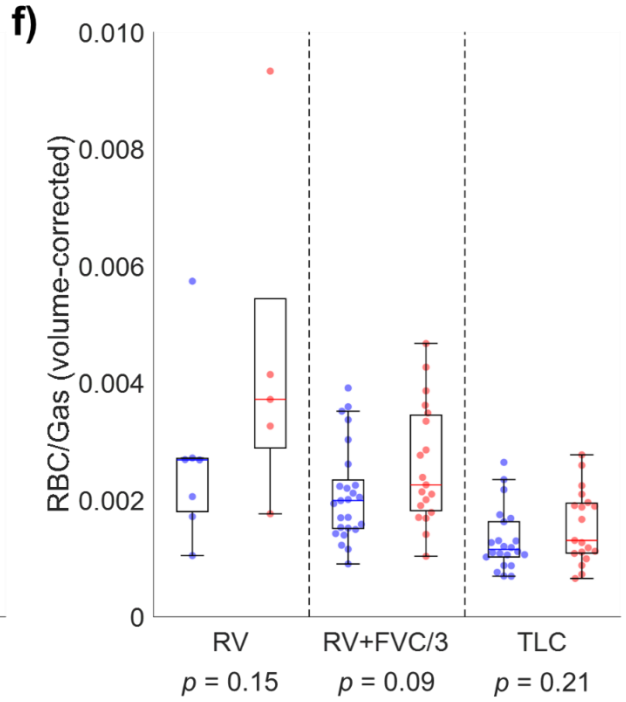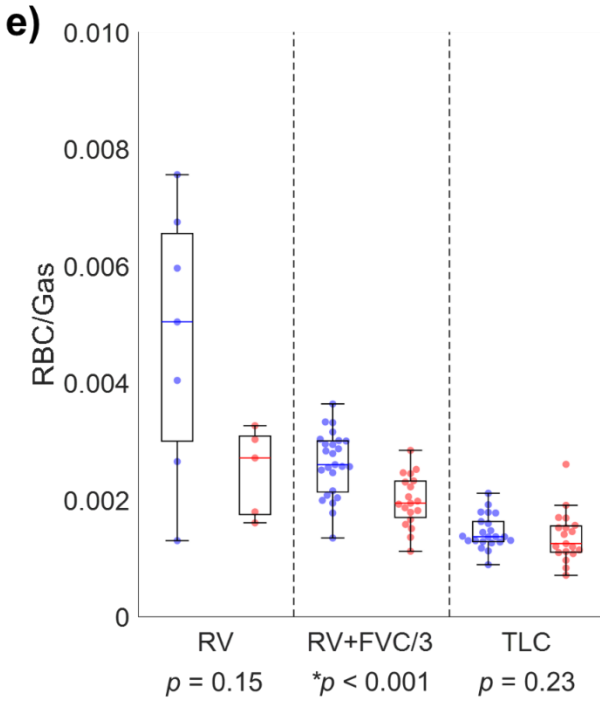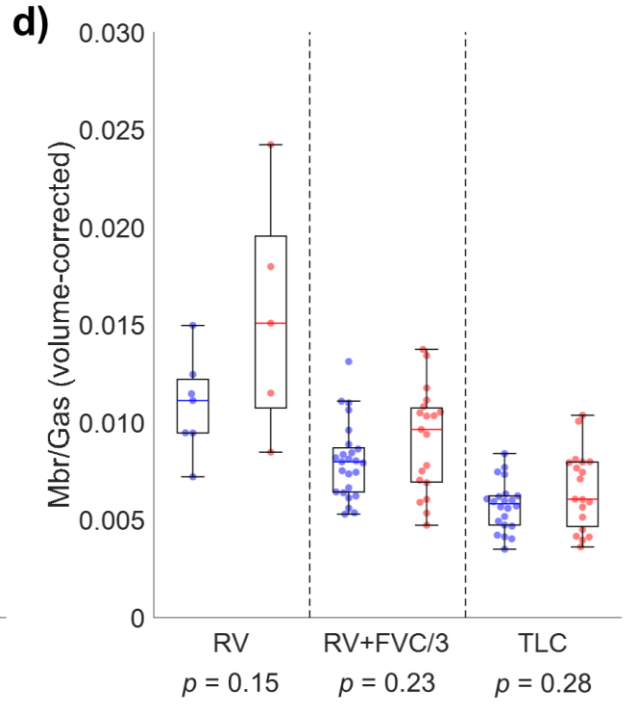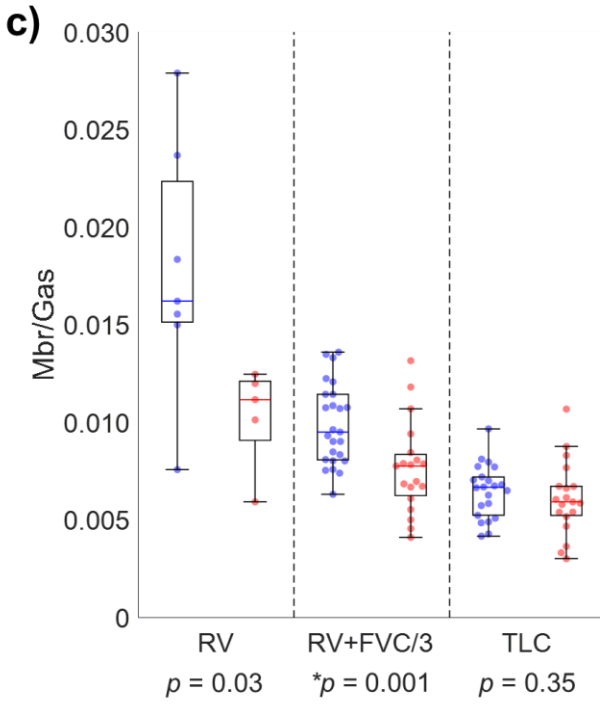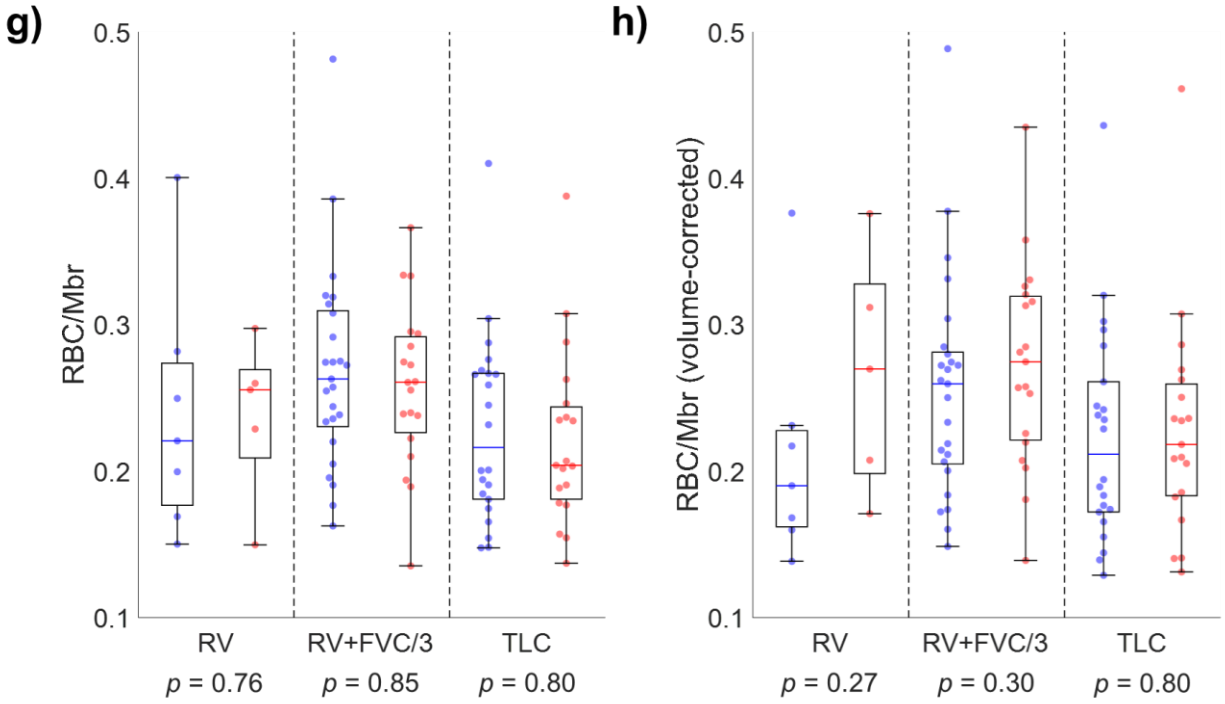
Figure 3.6: Boxplots of **a)** lung volumes, **b)** lung volumes normalized to total lung capacity (TLC), **c)** Mbr/Gas, **e)** RBC/Gas, and **g)** RBC/Mbr, separated by inflation level, in participants with chronic obstructive pulmonary disease (COPD, red) and older healthy participants (blue). **d)** Mbr/Gas, **f)** RBC/Gas, and **h)** RBC/Mbr corrected for lung volume contribution by estimating measurement at a reference lung volume for each inflation level using Eq. 3.2, separated by disease state and inflation level. * indicates a significant difference between groups after Bonferroni correction.

	Number of scans		Volume (L)		Mbr/Gas		RBC/Gas		RBC/Mbr	
	Healthy	**COPD**	**Healthy**	**COPD**	**Healthy**	**COPD**	**Healthy**	**COPD**	**Healthy**	**COPD**
RV	7	5	2.4	4.3	0.0178	0.0103	0.0048	0.0025	0.24	0.24
RV+FVC/3	25	19	3.8	5.0	0.0100	0.0077	0.0026	0.0020	0.27	0.26
TLC	22	19	5.0	5.8	0.0065	0.0061	0.0015	0.0014	0.23	0.22

Table 3.8: Mean volumes and gas uptake ratios for all participants in either the older healthy or COPD groups.

	Vol. (L)	Vol./TLC	Mbr/Gas	Mbr/Gas†	RBC/Gas	RBC/Gas†	RBC/Mbr	RBC/Mbr†
RV	0.02	0.15	0.03	0.15	0.15	0.15	0.76	0.27
RV+FVC/3	0.001*	<0.001*	0.001*	0.23	<0.001*	0.09	0.85	0.30
TLC	0.15	0.89	0.35	0.28	0.23	0.21	0.80	0.80

Table 3.9: Wilcoxon rank-sum test *p*-values for comparison of volumes and gas uptake ratios between older healthy and COPD groups. * indicates coefficients less than the significance threshold after Bonferroni correction ($p = 0.05/24 \approx 0.0021$). † indicates ratios projected to reference lung volumes.

3.4. Discussion

Results from the lung volume dependence portion of the study implicate volume differences as an important source of variability for Mbr/Gas and RBC/Gas ratios in both healthy and diseased participants. This finding, while intuitive, holds important implications for the field of dissolved-phase ^{129}Xe MRI. These results echo those from a recent investigation by Hahn et al. (26) of xenon-uptake ratios in healthy volunteers using the single-point Dixon method, which examined the lung-volume dependence of repeated measurements at a target lung volume of functional residual capacity plus 1 L. The authors found significant correlations between relative ratio differences and relative volume differences for Mbr/Gas and RBC/Gas, with a linear slope near 1.0 for both, but no significant correlation for RBC/Mbr.

Examining these relationships over a much wider range of volume differences, this study identified larger and significantly different slopes for Mbr/Gas ($\alpha = 1.38 \pm 0.06$) and RBC/Gas ($\alpha = 1.74 \pm 0.12$), and a significantly nonzero slope for RBC/Mbr ($\alpha = 0.44 \pm 0.08$). The values of α above 1 for Mbr/Gas and RBC/Gas suggest that surface-to-volume ratio changes driven by alveolar recruitment and/or inflation do not by themselves account for the volume dependencies of these ratios, and thus either shape change of the alveoli during inflation or other factors driving the ability of inhaled gas to access and transit the alveolar membrane must therefore play a role. The nonzero volume dependence of RBC/Mbr is implied by the unequal dependencies of the other two ratios, and further reinforces the notion that alveolar shape change across inflation levels does not explain the observed lung volume dependence of these ratios alone.

These relationships were found to be consistent across age range and presence of disease, and are reminiscent of a similar observation that had previously been made comparing CT-based

measurements of lung density performed at disparate lung volumes across individuals with widely varying ages and disease states (36). These previous results, as well as those described here, suggest that volume-related ratio differences were primarily driven by basic lung physiology, rather than COPD- or age-related processes, and imply that corrections for volume-related ratio differences based on such empirical relationships, which have been suggested previously (25), should be implemented. The current work presents an initial demonstration of concept for how such a correction might be performed, but further work is necessary to establish and validate a more authoritative approach.

Although the differential volume dependencies appeared linear across the achievable range of lung volumes, the absolute volume dependence was strongest at smaller lung volumes, again echoing CT-based lung density measurements made at disparate volumes (36). Strong volume dependence was entirely expected for Mbr/Gas and RBC/Gas since changing the inflation level will affect the denominator much more than the numerator for these two ratios. The origin of the RBC/Mbr volume dependence is less obvious, however, as the gas signal does not appear in this ratio. As suggested in previous work, the observed decrease in RBC/Mbr with increasing inflation level is consistent with decreased blood volume at higher inflation levels, possibly due to greater alveolar pressure (9,26).

All three signal ratios were repeatable in participants with COPD, but RBC/Mbr was more repeatable than RBC/Gas, in general agreement with previous results (26,27). The better repeatability of RBC/Mbr compared with RBC/Gas likely reflects strong covariance of the membrane and RBC components in response to volume changes and correspondingly lower sensitivity of RBC/Mbr to small lung volume perturbations between repeated scans. RBC/Mbr also displayed the smallest volume dependence and RBC/Gas the greatest, as indicated by the fit values of α, supporting the notion that covariance of the membrane and RBC components suppresses volume-driven changes in RBC/Mbr. Lung volumes were also generally repeatable but were better repeated when the target volume was TLC rather than RV+FVC/3; this finding likely corresponds with the greater number of variables in the RV+FVC/3 inhalation procedure compared with that for TLC.

The better volume repeatability at TLC, together with the weaker absolute volume dependence in this regime for all signal ratios, suggest that TLC may be the optimal inflation level for signal-

ratio measurements to maximize repeatability and minimize sensitivity to scan-to-scan and person-to-person lung volume differences. However, dose volume during experiments is also an important concern, as discussed in a recent position paper from the ^{129}Xe MRI Clinical Trials Consortium (4). Performing these studies at TLC, rather than the lower inflation levels (one-sixth of TLC, or one-fifth of FVC) recommended by the Consortium, results in diluted ^{129}Xe concentration and therefore lower signal-to-noise ratio. Moreover, increasing the volume of ^{129}Xe and anoxic buffer gas delivered per dose in order to achieve an inflation level near TLC is likely to increase the frequency and severity of temporary physiological effects associated with ^{129}Xe inhalation. High inflation levels also may not provide optimal sensitivity to disease, as seen in the current work, in which no significant groupwise differences between any gas-uptake measurements were detected at TLC.

That said, the results shown here also suggest that at lower inflation levels, gas uptake measurements are sensitive to hyperinflation, a key aspect of emphysema pathophysiology. Groupwise Mbr/Gas and RBC/gas differences in the study sample diminished when lung-volume corrections were applied, demonstrating that care must be taken when comparing these measurements at lower inflation levels in COPD to those in health. It is evident that further discussion and experimentation is likely necessary in order to identify practices for dissolved-phase ^{129}Xe MRI in the COPD context that will best support disease characterization.

A limitation of the study is that although eligibility criteria for the older healthy and COPD participant groups covered the same age range, the mean ages of the two groups were significantly different. Further, the older healthy group was predominantly female, whereas the COPD group was almost evenly split. This sex mismatch might partially explain the higher lung volumes measured in the COPD group. Another limitation is the disparate imaging resolutions used within and across participants, which may confound results by producing differences in partial volume effects between measurements. Additionally, while it is expected that the observed lung-volume dependencies would generally hold true for ^{129}Xe gas uptake metrics measured using single-point Dixon MRI or CSSR spectroscopy, only the IDEAL-based method was specifically examined in the study. The data set also lacks repeated dissolved-phase ^{129}Xe MRI scans at TLC. The results presented here suggest that ratio measurements may be more repeatable at TLC than at lower inflation levels, given the lower sensitivity of measured ratios to

lung volume perturbations and higher repeatability of lung volumes themselves between scans. That said, future work is necessary to validate this hypothesis and to fully evaluate the diagnostic sensitivity of scans at TLC relative to those at lower inflation levels.

In conclusion, gas uptake metrics based on dissolved-phase [129]Xe lung MRI showed high repeatability in both healthy participants and participants with COPD, with variations in lung volume as an important driver of metric variability. Linear relative-difference relationships between signal ratios and lung volume that were consistent across study groups were observed and characterized. Finally, significant differences found in Mbr/Gas and RBC/Gas between healthy participants and participants with COPD were largely eliminated upon correcting for lung-volume contribution by projecting signal ratios to expected values at reference volumes specific to each target inflation level, demonstrating the need for careful consideration of volume-related effects when comparing results in patients with COPD with those in healthy individuals.

3.5. Appendix

3.5.1. Intraclass correlation coefficient

The intraclass correlation coefficient (ICC) is a descriptive statistic that can be used to infer test-retest and rater-to-rater measurement reliability for a given test from a study of the test in a representative sample (35,37,38). Selection of the appropriate ICC expression depends upon the nature and number of the measurement system(s) (or "rater(s)") used in the study, the nature and number of the measurement system(s) to be used in actual application of the studied measurement technique, and whether absolute agreement or relative consistency is desired between measurement system(s). For the study described here, the measurement system can be understood to include (but perhaps not be limited to) the MR scanner, the pulse sequences used to collect dissolved-phase and lung volume data, and the described analysis procedure. The appropriate ICC characteristics for this study are as follows:

- Model selection: a two-way random-effects model should be used, as the single measurement system used on all subjects in the study is a representative example of

measurement systems used at other institutions, and the study results are intended to generalize to these similar measurement systems.

- Type selection: a single-measure type should be used, because in general practice only a single measurement system would be used to perform these measurements in a given subject.
- Definition selection: absolute-agreement should be used, as different measurement systems should be expected to measure the same or similar values if used in the same subject.

The expression for two-way random, single-measure, absolute-agreement ICC is as follows:

$$ICC = \frac{MS_R - MS_E}{MS_R + (k-1)MS_E + \frac{k}{n}(MS_C - MS_E)} \tag{3.3}$$

where MS_R is the mean square for rows (i.e., subjects), MS_C is the mean square for columns (i.e., individual measurements), MS_E is the mean square error, k is the number of measurements per subject, and n is the number of subjects.

3.5.2. Coefficient of variation

The coefficient of variation is a normalized measure of the extent of data variability for data measured on a ratio scale. In general, the coefficient of variation of a set of measurements can be calculated by dividing the standard deviation of the measured values by the mean of the measured values.

A modification of the standard coefficient of variation can be made to assess within-subject variability (39,40). This within-subject coefficient of variation can be calculated for repeated measurement vectors X and Y each consisting of n measurements using a logarithmic method described by Bland and Altman (40), as follows:

$$CV = \exp\left(\sqrt{\frac{1}{n}\sum_{i=1}^{n}\frac{1}{2}(\log(X_i) - \log(Y_i))^2}\right) - 1 \tag{3.4}$$

The 95% confidence intervals of the within-subject coefficient of variation can be found for paired measurements as follows:

$$CI_{CV} = CV \pm 1.96 * \sqrt{\frac{1}{2n^2} \sum_{i=1}^{n} \frac{1}{2} (\log(X_i) - \log(Y_i))^2} \qquad (3.5)$$

3.5.3. Bland-Altman analysis

Bland-Altman analysis and plots quantify and visualize agreement between two quantitative, paired sets of measurements (41–43). Data in Bland-Altman plots are plotted as the difference between paired measurements vs. the mean of the corresponding measurements. Typically, the horizontal line indicating the measurement mean discrepancy (i.e., the mean of the paired measurement differences) is plotted, as well as horizontal lines indicating the 95% limits of agreement (i.e., the mean of the paired measurement differences plus/minus ~1.96 times the standard deviation of the paired measurement differences, assuming that the paired measurement differences can be considered to follow an approximately Gaussian distribution). For repeated measures of the same quantity, the mean discrepancy indicates any systemic difference between results of the earlier and later of the two measurements, while the 95% limits of agreement provide an estimate of typical measurement-to-measurement variability.

3.5.4. Spearman rank correlation

The Spearman rank correlation coefficient measures rank correlation between two variables, assessing whether the relationship between the two variables of interest can be described by a monotonic function (44,45). Spearman correlation can be interpreted as the Pearson linear correlation of the rankings of the respective variables. Spearman correlation is non-parametric; i.e., no specific functional relationship is assumed between the values of the two variables (in contrast to Pearson linear correlation, which assumes a linear relationship between the variables).

The Spearman correlation r between two variables x and y having ranks $R(x)$ and $R(y)$ is defined as follows:

$$r_s = \frac{cov\big(R(x), R(y)\big)}{\sigma_{R(x)}\sigma_{R(y)}} \qquad (3.6)$$

where cov($R(x)$ and $R(y)$) denotes the covariance of the rank variables, and $\sigma_{R(x)}$ and $\sigma_{R(y)}$ denote the standard deviations of the rank variables $R(x)$ and $R(y)$, respectively.

For the case where all ranks are distinct integers, the following equation can be used:

$$r_s = 1 - \frac{6\sum_{i=1}^n d_i^2}{n(n^2-1)} \qquad (3.7)$$

where $d_i = R(x_i) - R(y_i)$ is the difference between the two ranks corresponding to a given measurement and n is the number of measurements.

3.5.5. Wilcoxon rank-sum test

The Wilcoxon rank-sum test is a nonparametric test of median equality of populations represented by two independent samples X and Y (46,47). The null hypothesis of the Wilcoxon rank-sum test is that the probability of X being greater than Y is equal to the probability of Y being greater than X. Calculation of the z-score in the Wilcoxon rank-sum test incorporates the U statistic, which describes

The U statistic for each of the two compared groups is calculated as follows:

- Assign numeric ranks to all measurements from the combined groups, from smallest to largest. (For purposes of this study in which each measurement was expressed to several decimal places and ties did not occur, tied measurements are not considered.)
- Add all rank values for the measurements in sample X (Y). Denote this quantity as R_X (R_Y).
- Calculate U_X (U_Y) as follows, where n_X (n_Y) is the sample size of X (Y):

$$U_X = R_X - \frac{n_X(n_X+1)}{2}$$
$$U_Y = R_Y - \frac{n_Y(n_Y+1)}{2} \qquad (3.8)$$

- Take the smaller value of U_X and U_Y as the U statistic.

For large samples, a z statistic can be calculated from the U statistic using the following expression:

$$z = \frac{U - \frac{n_X n_Y}{2}}{\sqrt{\frac{n_X n_Y (n_X + n_Y + 1)}{12}}} \tag{3.9}$$

The U or z statistic can then be used to determine the significance value of the test, and the significance value can be compared with the chosen threshold for rejection of the null hypothesis (chosen to be 0.05 before Bonferroni correction in this study) to determine whether the null hypothesis is rejected for the given two samples.

3.6. References

1.   Mugler JP, Altes TA. Hyperpolarized 129Xe MRI of the human lung. J Magn Reson Imaging. 2013 Feb;37(2):313–31.

2.   Ebner L, Kammerman J, Driehuys B, Schiebler ML, Cadman RV, Fain SB. The role of hyperpolarized 129xenon in MR imaging of pulmonary function. Eur J Radiol. 2017 Jan;86:343–52.

3.   Marshall H, Stewart NJ, Chan HF, Rao M, Norquay G, Wild JM. In vivo methods and applications of xenon-129 magnetic resonance. Progress in Nuclear Magnetic Resonance Spectroscopy. 2021 Feb 1;122:42–62.

4.   Niedbalski PJ, Hall CS, Castro M, Eddy RL, Rayment JH, Svenningsen S, et al. Protocols for multi-site trials using hyperpolarized 129Xe MRI for imaging of ventilation, alveolar-airspace size, and gas exchange: A position paper from the 129Xe MRI clinical trials consortium. Magnetic Resonance in Medicine. 2021;86(6):2966–86.

5.   Miller KW, Reo NV, Schoot Uiterkamp AJ, Stengle DP, Stengle TR, Williamson KL. Xenon NMR: chemical shifts of a general anesthetic in common solvents, proteins, and membranes. Proceedings of the National Academy of Sciences. 1981 Aug;78(8):4946–9.

6.   Norquay G, Leung G, Stewart NJ, Tozer GM, Wolber J, Wild JM. Relaxation and exchange dynamics of hyperpolarized 129Xe in human blood. Magnetic Resonance in Medicine. 2015;74(2):303–11.

7.   Mugler JP, Altes TA, Ruset IC, Dregely IM, Mata JF, Miller GW, et al. Simultaneous magnetic resonance imaging of ventilation distribution and gas uptake in the human lung using hyperpolarized xenon-129. Proceedings of the National Academy of Sciences. 2010 Dec 14;107(50):21707–12.

8.   Cleveland ZI, Cofer GP, Metz G, Beaver D, Nouls J, Kaushik SS, et al. Hyperpolarized 129Xe MR Imaging of Alveolar Gas Uptake in Humans. PLOS ONE. 2010 Aug 16;5(8):e12192.

9.   Qing K, Mugler III JP, Altes TA, Jiang Y, Mata JF, Miller GW, et al. Assessment of lung function in asthma and COPD using hyperpolarized 129Xe chemical shift saturation recovery spectroscopy and dissolved-phase MRI. NMR in Biomedicine. 2014;27(12):1490–501.

10.   Stewart NJ, Leung G, Norquay G, Marshall H, Parra-Robles J, Murphy PS, et al. Experimental validation of the hyperpolarized 129Xe chemical shift saturation recovery technique in healthy volunteers and subjects with interstitial lung disease. Magnetic Resonance in Medicine. 2015;74(1):196–207.

11.   Mata J, Guan S, Qing K, Tustison N, Shim Y, Mugler JP, et al. Evaluation of Regional Lung Function in Pulmonary Fibrosis with Xenon-129 MRI. Tomography. 2021 Sep 15;7(3):452–65.

12.   Kaushik SS, Robertson SH, Freeman MS, He M, Kelly KT, Roos JE, et al. Single-breath clinical imaging of hyperpolarized 129xe in the airspaces, barrier, and red blood cells using an interleaved 3D radial 1-point Dixon acquisition. Magnetic Resonance in Medicine. 2016;75(4):1434–43.

13.   Hahn AD, Kammerman J, Fain SB. Removal of hyperpolarized 129Xe gas-phase contamination in spectroscopic imaging of the lungs. Magnetic Resonance in Medicine. 2018;80(6):2586–97.

14.   Tsao J, Jiang Y. Hierarchical IDEAL: Fast, robust, and multiresolution separation of multiple chemical species from multiple echo times. Magnetic Resonance in Medicine. 2013;70(1):155–9.

15.   Qing K, Ruppert K, Jiang Y, Mata JF, Miller GW, Shim YM, et al. Regional mapping of gas uptake by blood and tissue in the human lung using hyperpolarized xenon-129 MRI. Journal of Magnetic Resonance Imaging. 2014;39(2):346–59.

16.   Zanette B, Santyr G. Accelerated interleaved spiral-IDEAL imaging of hyperpolarized 129Xe for parametric gas exchange mapping in humans. Magnetic Resonance in Medicine. 2019;82(3):1113–9.

17.   Wang JM, Robertson SH, Wang Z, He M, Virgincar RS, Schrank GM, et al. Using hyperpolarized 129Xe MRI to quantify regional gas transfer in idiopathic pulmonary fibrosis. Thorax. 2018 Jan 1;73(1):21–8.

18.   Wang Z, Bier EA, Swaminathan A, Parikh K, Nouls J, He M, et al. Diverse cardiopulmonary diseases are associated with distinct xenon magnetic resonance imaging signatures. European Respiratory Journal [Internet]. 2019 Dec 1 [cited 2023 Jun 22];54(6). Available from: https://erj.ersjournals.com/content/54/6/1900831

19. Qing K, Tustison NJ, Mugler JP, Mata JF, Lin Z, Zhao L, et al. Probing Changes in Lung Physiology in COPD Using CT, Perfusion MRI, and Hyperpolarized Xenon-129 MRI. Academic Radiology. 2019 Mar 1;26(3):326–34.

20. Myc L, Qing K, He M, Tustison N, Lin Z, Manichaikul AW, et al. Characterisation of gas exchange in COPD with dissolved-phase hyperpolarised xenon-129 MRI. Thorax. 2021 Feb 1;76(2):178–81.

21. Mummy DG, Coleman EM, Wang Z, Bier EA, Lu J, Driehuys B, et al. Regional Gas Exchange Measured by 129Xe Magnetic Resonance Imaging Before and After Combination Bronchodilators Treatment in Chronic Obstructive Pulmonary Disease. Journal of Magnetic Resonance Imaging. 2021;54(3):964–74.

22. Kaushik SS, Freeman MS, Yoon SW, Liljeroth MG, Stiles JV, Roos JE, et al. Measuring diffusion limitation with a perfusion-limited gas—Hyperpolarized 129Xe gas-transfer spectroscopy in patients with idiopathic pulmonary fibrosis. Journal of Applied Physiology. 2014 Sep 15;117(6):577–85.

23. Weatherley ND, Stewart NJ, Chan HF, Austin M, Smith LJ, Collier G, et al. Hyperpolarised xenon magnetic resonance spectroscopy for the longitudinal assessment of changes in gas diffusion in IPF. Thorax. 2019 May 1;74(5):500–2.

24. Rankine LJ, Wang Z, Wang JM, He M, McAdams HP, Mammarappallil J, et al. 129Xenon Gas Exchange Magnetic Resonance Imaging as a Potential Prognostic Marker for Progression of Idiopathic Pulmonary Fibrosis. Ann Am Thorac Soc. 2020 Jan;17(1):121–5.

25. Inati SJ, Hansen MS, Kellman P. A fast optimal method for coil sensitivity estimation and adaptive coil combination for complex images. In: Proc Intl Soc Mag Reson Med 22. 2014. p. 4407.

26. Hahn AD, Kammerman J, Evans M, Zha W, Cadman RV, Meyer K, et al. Repeatability of regional pulmonary functional metrics of Hyperpolarized 129Xe dissolved-phase MRI. Journal of Magnetic Resonance Imaging. 2019;50(4):1182–90.

27. Kern AL, Gutberlet M, Qing K, Voskrebenzev A, Klimeš F, Kaireit TF, et al. Regional investigation of lung function and microstructure parameters by localized 129Xe chemical shift saturation recovery and dissolved-phase imaging: A reproducibility study. Magnetic Resonance in Medicine. 2019;81(1):13–24.

28. Stewart NJ, Horn FC, Norquay G, Collier GJ, Yates DP, Lawson R, et al. Reproducibility of quantitative indices of lung function and microstructure from 129Xe chemical shift saturation recovery (CSSR) MR spectroscopy. Magnetic Resonance in Medicine. 2017;77(6):2107–13.

29. Hersman FW, Ruset IC, Ketel S, Muradian I, Covrig SD, Distelbrink J, et al. Large Production System for Hyperpolarized 129Xe for Human Lung Imaging Studies. Academic Radiology. 2008 Jun 1;15(6):683–92.

30. Driehuys B, Cates GD, Miron E, Sauer K, Walter DK, Happer W. High-volume production of laser-polarized 129Xe. Applied Physics Letters. 1996 Sep 16;69(12):1668–70.

31. Sutton BP, Noll DC, Fessler JA. Fast, iterative image reconstruction for MRI in the presence of field inhomogeneities. IEEE Trans Med Imaging. 2003 Feb;22(2):178–88.

32. Lustig M, Donoho D, Pauly JM. Sparse MRI: The application of compressed sensing for rapid MR imaging. Magnetic Resonance in Medicine. 2007;58(6):1182–95.

33. Tustison NJ, Avants BB, Lin Z, Feng X, Cullen N, Mata JF, et al. Convolutional Neural Networks with Template-Based Data Augmentation for Functional Lung Image Quantification. Acad Radiol. 2019 Mar;26(3):412–23.

34. Gil J, Bachofen H, Gehr P, Weibel ER. Alveolar volume-surface area relation in air- and saline-filled lungs fixed by vascular perfusion. J Appl Physiol Respir Environ Exerc Physiol. 1979 Nov;47(5):990–1001.

35. Koo TK, Li MY. A Guideline of Selecting and Reporting Intraclass Correlation Coefficients for Reliability Research. J Chiropr Med. 2016 Jun;15(2):155–63.

36. Brown RH, Wise RA, Kirk G, Drummond MB, Mitzner W. Lung Density Changes With Growth and Inflation. Chest. 2015 Oct 1;148(4):995–1002.

37. Bartko JJ. The Intraclass Correlation Coefficient as a Measure of Reliability. Psychol Rep. 1966 Aug 1;19(1):3–11.

38. McGraw KO, Wong SP. Forming inferences about some intraclass correlation coefficients. Psychological Methods. 1996;1(1):30–46.

39. Bland JM, Altman DG. Statistics notes: Measurement error. BMJ. 1996 Jun 29;312(7047):1654.

40. How should I calculate a within-subject coefficient of variation? [Internet]. [cited 2023 Oct 9]. Available from: https://www-users.york.ac.uk/~mb55/meas/cv.htm

41. Altman DG, Bland JM. Measurement in Medicine: The Analysis of Method Comparison Studies. Journal of the Royal Statistical Society Series D (The Statistician). 1983;32(3):307–17.

42. Bland JM, Altman D. Statistical methods for assessing agreement between two methods of clinical measurement. The Lancet. 1986 Feb 8;327(8476):307–10.

43. Giavarina D. Understanding Bland Altman analysis. Biochem Med (Zagreb). 2015 Jun 5;25(2):141–51.

44. Schober P, Boer C, Schwarte LA. Correlation Coefficients: Appropriate Use and Interpretation. Anesthesia & Analgesia. 2018 May;126(5):1763.

45. Best DJ, Roberts DE. Algorithm AS 89: The Upper Tail Probabilities of Spearman's Rho. Journal of the Royal Statistical Society Series C (Applied Statistics). 1975;24(3):377–9.

46. Mann HB, Whitney DR. On a Test of Whether one of Two Random Variables is Stochastically Larger than the Other. The Annals of Mathematical Statistics. 1947 Mar;18(1):50–60.

47. Fay MP, Proschan MA. Wilcoxon-Mann-Whitney or t-test? On assumptions for hypothesis tests and multiple interpretations of decision rules. Stat Surv. 2010;4:1–39.

Chapter 4: Free-breathing 4D ultrashort echo time balanced steady-state free precession ^{1}H lung MRI

4.1. Introduction

Obtaining strong signal from lung parenchyma using MRI is a significant technical challenge, due to its short T_2^* and low proton density. One approach to address this challenge is the use of an ultrashort echo time (UTE) radial pulse sequence (1–4). This technique samples the center of k-space immediately following excitation and before significant inhomogenity-driven dephasing of the transverse magnetization can occur, maximizing the signal that can be obtained from short T_2^* species.

Balanced steady-state free precession (bSSFP) techniques facilitate higher steady-state signal at shorter TRs than spoiled techniques, and have been demonstrated in the context of lung MRI (5–7). However, large B_0 disturbances in and about the lung often cause noticeable banding artifacts in bSSFP lung images, even for short TRs. Furthermore, for typical bSSFP techniques, TE does not occur immediately after excitation, but after a pre-phasing gradient that sets up a Cartesian k-space readout that is symmetric about the phase-encode axis. This results in the low-frequency parenchyma signal being sampled at the middle of the TR window, rather than at its maximum value immediately following excitation.

Motion of the lungs during breathing is also a significant barrier to high-quality lung MRI. Imaging during a breath-hold constrains available scan time to less than 30 seconds, limiting achievable resolution and signal-to-noise ratio (SNR). Imaging continuously during free breathing and reconstructing images from all sampled data can produce high-SNR, fine-resolution images, but at the cost of significant blurring in moving structures such as the pulmonary vasculature, diaphragm, and liver. Prospective respiratory triggering based on an imaging navigator centered on the diaphragm (1,8) can freeze motion to a reasonable extent, but lengthens scan times considerably over continuous imaging and restricts imaging of the lung to a single respiratory phase.

Compressed sensing approaches have been developed that apply a penalty term assessed along a temporal dimension that facilitates reconstruction of heavily under-sampled temporal frames (9–

11), and such approaches can be applied to the free-breathing lung MRI context in order to reconstruct high-quality images from under-sampled frames at a range of respiratory phases (12–14). In particular, the golden-angle radial sparse parallel (GRASP) family of techniques (15–18) reconstructs under-sampled image series produced from radial MR readouts using a total variation term applied along either a temporal or pseudo-temporal dimension, taking advantage of the high degree of mutual information contained in repeated images of the same field-of-view and the incoherence of under-sampling-related aliasing artifacts in radial MRI in order to reconstruct highly under-sampled image frames with relatively little visible under-sampling artifact.

A recent innovation to GRASP, entitled GRASP-Pro, takes yet further advantage of the temporal sparsity inherent in the 4D MRI image context (19,20). Rather than directly solving for a k-space image series using a compressed-sensing-based optimization, GRASP-Pro-based techniques start by solving for a low-rank temporal basis for a low-resolution image series reconstruction that is intended to effectively represent the true signal evolution of the collection of voxels in the image series. Compressed-sensing-based optimization is then applied to the matrix of subspace coefficients that is multiplied by the low-rank temporal basis in order to obtain a final image series.

The purpose of the work presented in this chapter was therefore to develop and demonstrate a combined 4D UTE bSSFP spoke-radial pulse sequence with a GRASP-Pro-based reconstruction algorithm for high-resolution, high-signal, respiratory-phase-resolved MRI of the lung. This pulse sequence takes advantage of the high signal even for short TR inherent in bSSFP techniques, as well as the ability to read out at low-frequency k-space locations immediately after excitation inherent in radial UTE techniques. The reconstruction approach exploits the natural sparsity of the sorted respiratory phase-binned image series in the respiratory-phase domain to de-noise highly under-sampled images at each phase.

4.2. Simulation of bSSFP vs. spoiled signal

4.2.1. Methods

To gain insight into expected signal behavior for UTE bSSFP and UTE spoiled pulse sequences, temporal signal evolution was modelled using Bloch equation solutions applied to an ensemble of $S = 5001$ simulated spins. T_2^*-driven dephasing was simulated by modelling off-resonance frequencies of the spins using a Lorentzian distribution (Fig. 4.1), as follows:

$$\Delta f_j = bB_0 \tan\left(\pi \cdot \left(\frac{j}{S+1} - 0.5\right)\right), 1 \leq j \leq S \tag{4.1}$$

where Δf_j is the frequency offset from the Larmor frequency of the jth spin in the ensemble and b is an empirically-determined constant chosen to achieve a desired modelled T_2^* in simulated precession of a spin ensemble modelled using a given T_2 and at a particular field strength B_0. To simulate different degrees of global off-resonance for a given isochromat, an additional precession angle β was applied equally to all spins in the simulated isochromat over the course of each TR window. β is related to the global off-resonance frequency $\Delta f = f_{actual} - f_0$ as follows:

$$\beta = TR \cdot 2\pi\Delta f \tag{4.2}$$
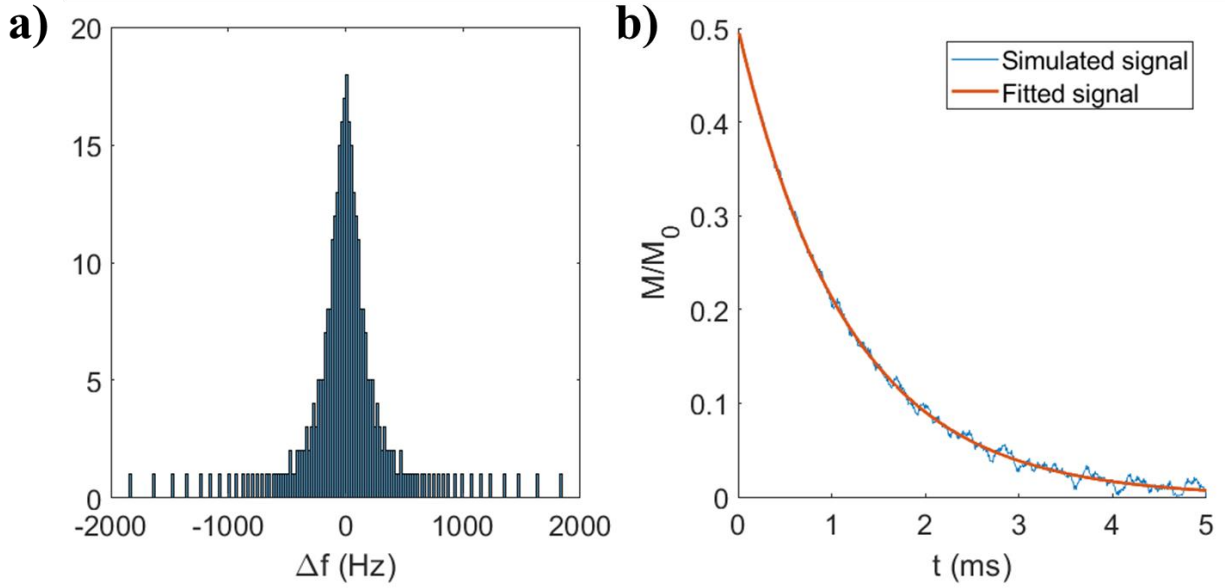
Figure 4.1: **a)** Simulated distribution of spin offset frequencies within an isochromat to achieve a T_2^* of ~1.2 ms for the material properties listed in Table 4.1 for lung parenchyma at 1.5 T. **b)** Simulated coherent transverse magnetization magnitude following excitation with a 30° RF pulse (blue line), fitted to a simple model of T_2^*-driven dephasing and T_2-driven magnetization decay (orange line).

Signal was plotted over the course of a single TR window occurring after a steady state was reached, with simulation carried out for a total of 2000 TR windows prior to the plotted window to ensure that a steady state was reached. Phase cycling of 180° was applied between sequential simulated RF pulses. Diffusion and other possible confounding effects were neglected in the simulation. For simulation of spoiled sequences, perfect spoiling was assumed, and the analytical Ernst angle θ_E was used for the simulated TR and T_1:

$$\theta_E = \arccos\left(e^{-TR/T_1}\right) \tag{4.3}$$

Estimated material properties for pulmonary blood vessels and lung parenchyma that were used for signal simulation (21–23) are given in Table 4.1. A field strength of $B_0 = 1.5$ T was used for all simulations.

	T_1 (ms)	T_2 (ms)	T_2^* (ms)	b (Hz/T)
Vasculature	2000	160	100	0.45
Parenchyma	1375	65	1.2 (TLC)	89 (TLC)
			2.0 (RV)	51 (RV)

Table 4.1: Simulated material properties for pulmonary blood vessels and lung parenchyma. A field strength of 1.5 T is assumed, and constants b associated with the T_2, T_2^*, and magnetic field strength combination for a given material are additionally given. T_2^* of parenchyma was assumed to differ at end-of-inhalation (total lung capacity, TLC) and end-of-exhalation (residual volume, RV) based on observations in the literature *(21)*.

4.2.2. Results

Results of Bloch simulations are shown in Figs. 4.2, 4.3, and 4.4 for the pulse sequence parameters described in section 4.2.2 using the simulated material properties for vasculature and lung parenchyma given in Table 4.1. For vasculature (Fig. 4.2), the signal availability remains essentially constant throughout the TR window at steady-state, because T_2^* is much longer than TR, resulting in relatively small off-resonance frequency spread about the global frequency. Global off-resonance heavily affects available signal for bSSFP imaging, however, with particular β values leading to near-disappearance of the signal, corresponding to the band-shaped signal voids characteristic of off-resonance image regions in bSSFP. The simulated signal intensity for bSSFP imaging (aside from regions in the signal voids) was several times higher than that for spoiled imaging throughout the TR window.
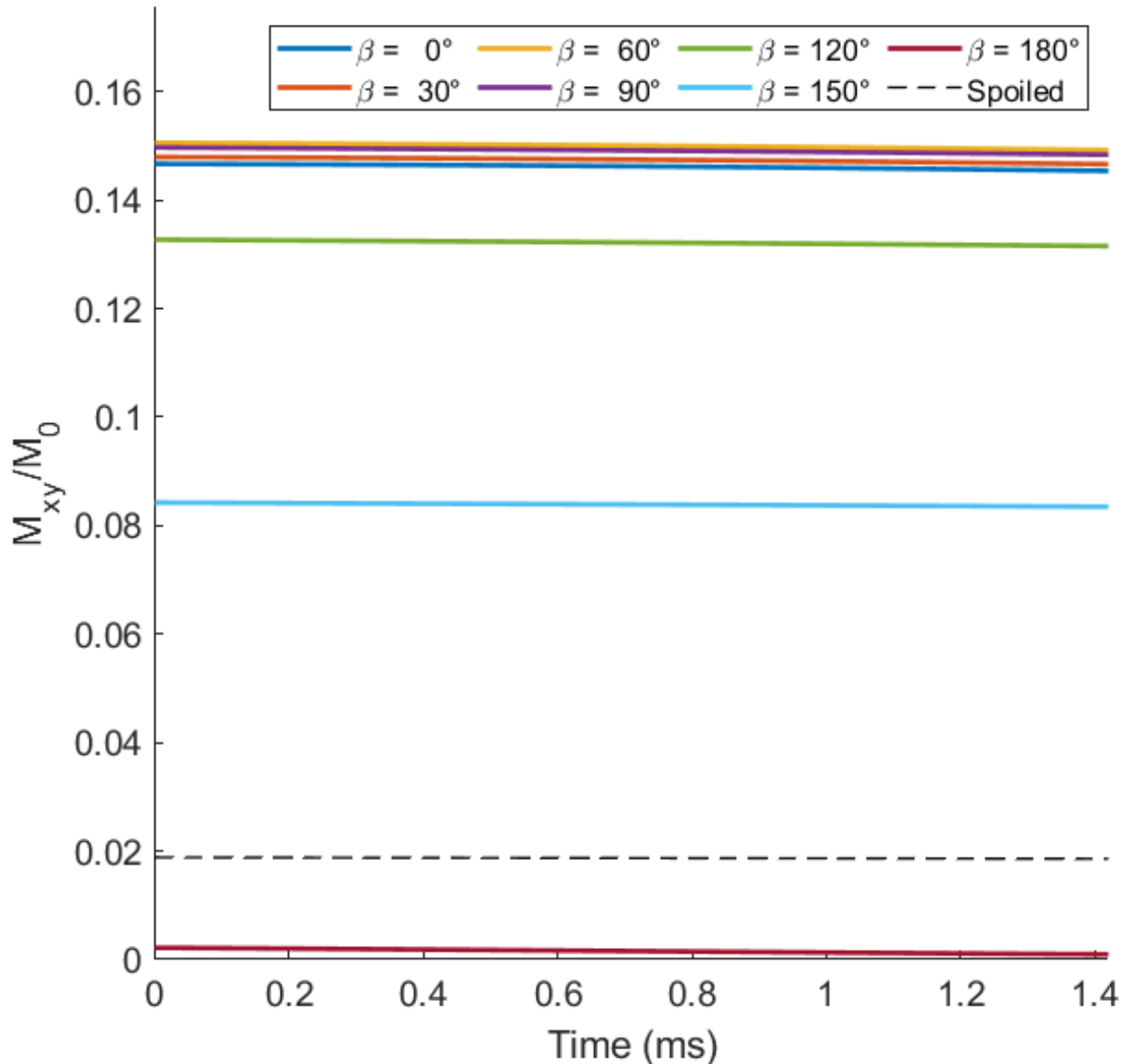
Figure 4.2: Simulated available signal at steady-state for vasculature (parameters given in Table 4.1) throughout a TR window at field strength $B = 1.5$ T for TR $= 1.42$ ms for bSSFP (solid lines, global offset angle β labeled in caption for each line, flip angle $= 25°$) and spoiled (dashed line, Ernst angle $\approx 2.6°$) imaging.

For lung parenchyma at total lung capacity (TLC, Fig. 4.3), the signal availability displays a "saddle" shape over the course of the TR window at steady-state for bSSFP imaging, with maximum signal at $t = 0$ and $t =$ TR and minimum signal at $t =$ TR/2. As with vasculature, global off-resonance affects the available signal, but unlike vasculature, at least some signal availability is maintained at the beginning and end of the TR window for all values of β, suggesting that susceptibility of lung parenchyma and other short-T_2* species to SSFP banding artifacts is

124

somewhat mitigated for echo times TE $\approx$ 0 (i.e., echoes immediately after excitation, as in spoke-radial readouts) and TE $\approx$ TR (i.e., refocused echoes that occur immediately prior to the next excitation). As with vasculature, the simulated signal intensity for SSFP imaging (aside from regions in the signal voids that were read out near the center of the TR window) was several times higher than that for spoiled imaging.

The behavior observed for lung parenchyma at residual volume (RV, Fig. 4.4) was generally similar to that of lung parenchyma at TLC (Fig. 4.3). Slightly higher signal, and smaller signal decrease toward the center of the TR window, was observed for $\beta < 150°$ at RV than at TLC. However, slightly lower signal was observed at RV than at TLC for offset angles $\beta = 150°$ and 180°, suggesting that the potential for visible banding artifacts would be slightly higher at RV than at TLC.
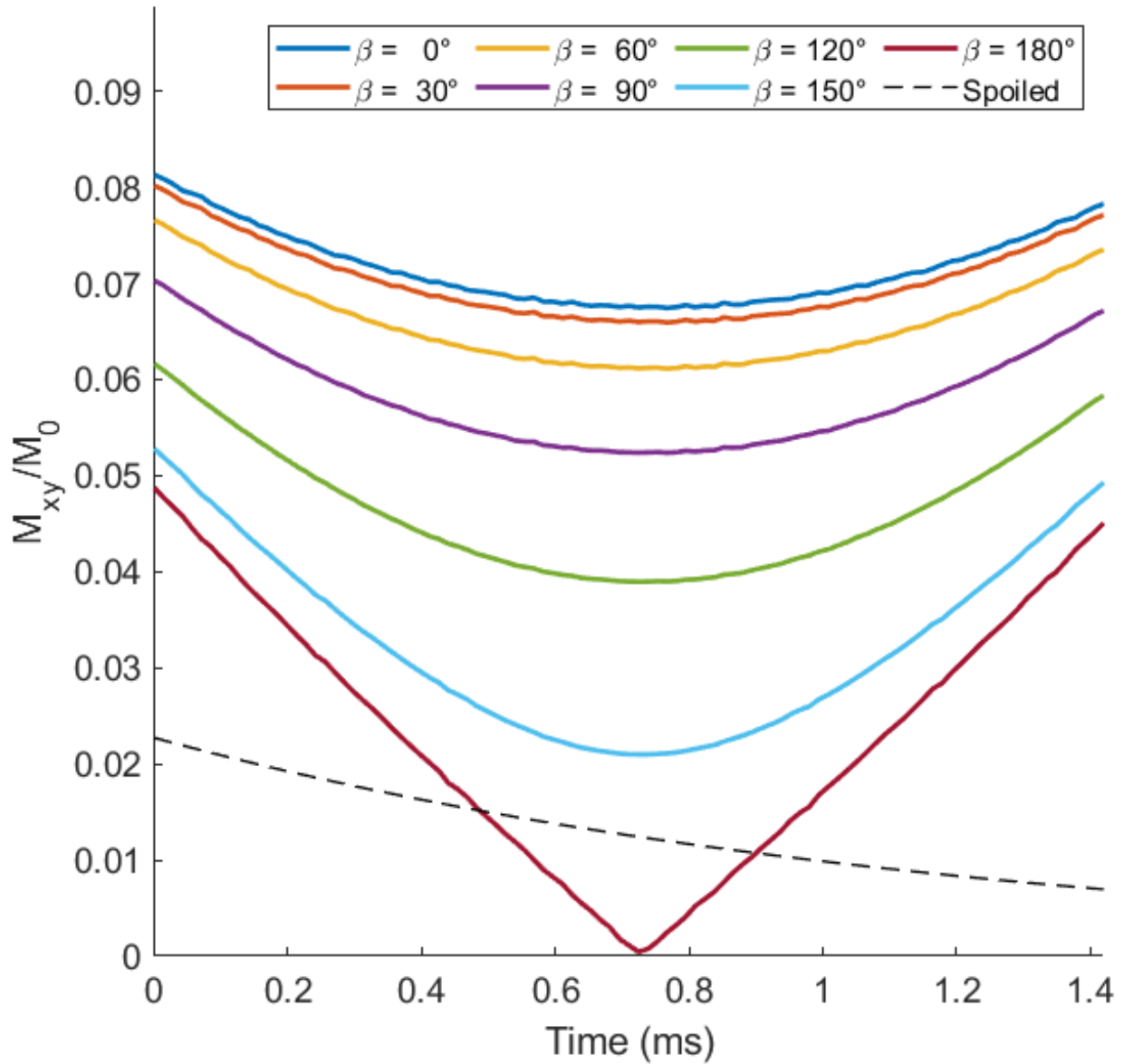
Figure 4.3: Simulated available signal at steady-state for lung parenchyma at total lung capacity (parameters given in Table 4.1) throughout a TR window at field strength $B = 1.5$ T for TR = 1.42 ms for bSSFP (solid lines, global offset angle β labeled in caption for each line, flip angle = 25°) and spoiled (dashed line, Ernst angle $\approx 2.6°$) imaging.
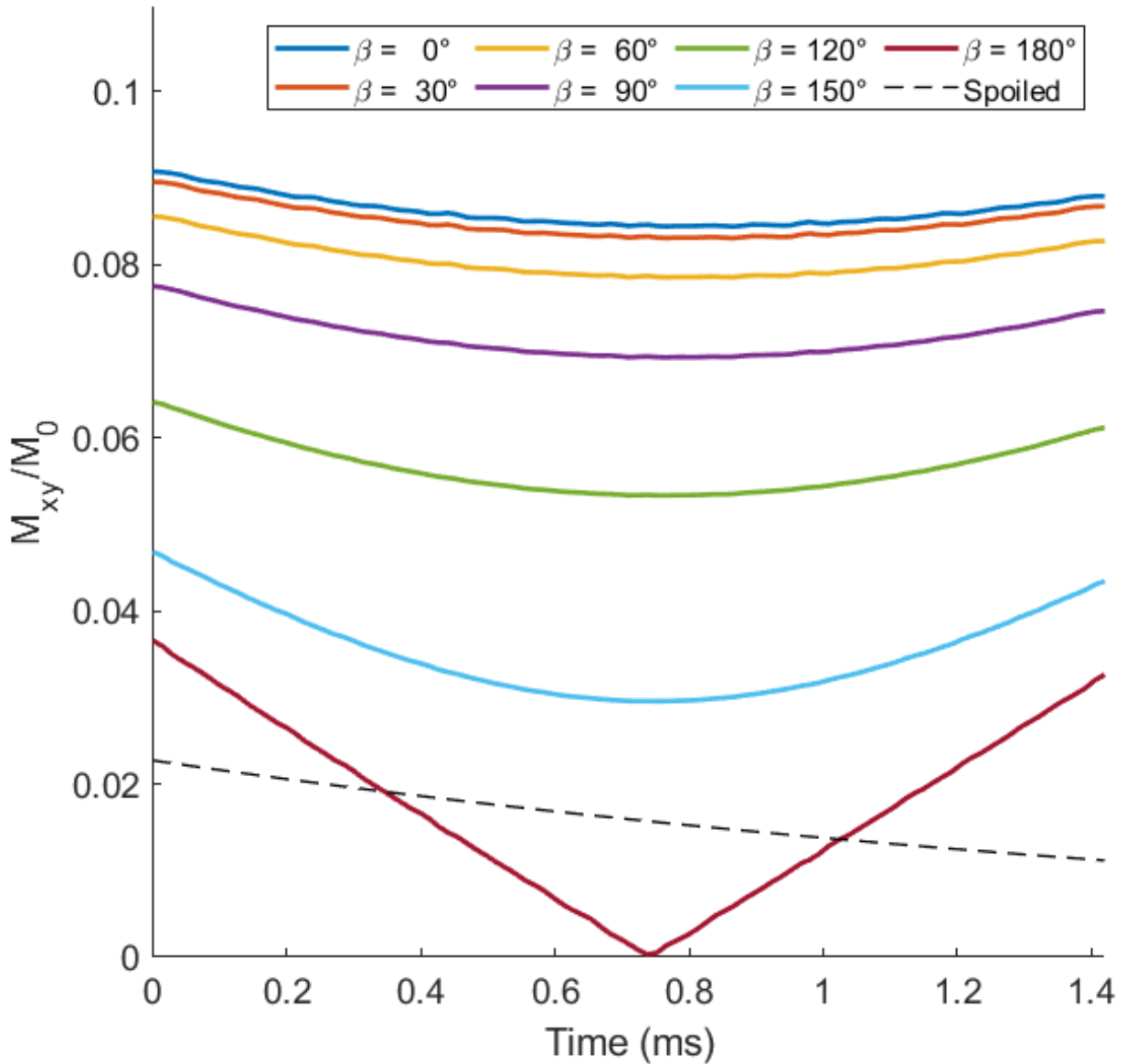
Figure 4.4: Simulated available signal at steady-state for lung parenchyma at residual volume (parameters given in Table 4.1) throughout a TR window at field strength $B = 1.5$ T for TR = 1.42 ms for bSSFP (solid lines, global offset angle β labeled in caption for each line, flip angle = 25°) and spoiled (dashed line, Ernst angle $\approx 2.6°$) imaging.

4.3. Respiratory-triggered 3D lung MRI

4.3.1. Methods

A diagram of the 3D radial UTE bSSFP pulse sequence used for the imaging studies described herein is shown in Fig. 4.5a. Precise pulse sequence parameters varied from subject to subject, but typical values were as follows: TR = 1.42 ms, TE = 0.13 ms, flip angle = 25° (with alternating 0°-180° phase from one readout to the next) matrix size = 256×256×256, resolution = 1.5 mm isotropic, maximum readout gradient amplitude = 22.65 mT/m.

Imaging was also performed in some subjects using a 3D radial UTE spoiled pulse sequence (Fig. 4.5b) for comparison. The smaller flip angle used for spoiled imaging permitted a shorter hard RF pulse and a shorter echo time, while the spoiler gradient applied after each readout lengthened the repetition time. Precise pulse sequence parameters varied from subject to subject, but typical values were as follows: TR = 2.93 ms, TE = 0.06 ms, flip angle = 5°, matrix size = 256×256×256, resolution = 1.5 mm isotropic, maximum readout gradient amplitude = 22.65 mT/m.
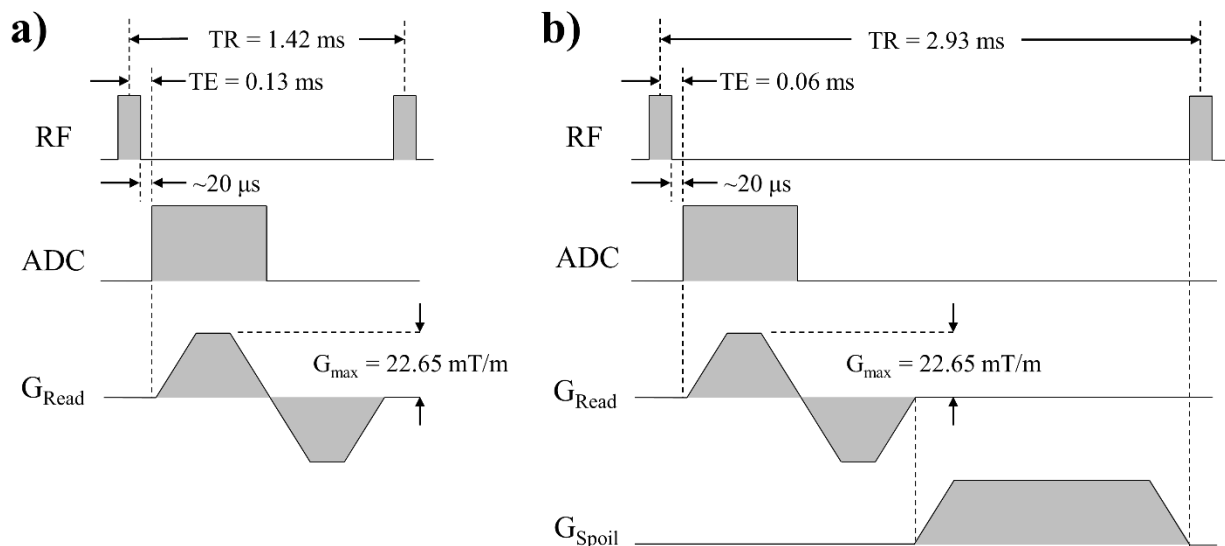
Figure 4.5: Pulse sequence diagrams for **a)** ultrashort echo time (UTE) balanced steady-state free precession MRI and **b)** UTE spoiled MRI. Adapted from Miller *et al* (1).

Respiratory triggering was performed using prospective acquisition correction (PACE) (8), in which the position of the diaphragm is monitored continuously via repeated acquisition of low-

resolution 2D images of a small user-defined field of view (FOV) centered on the diaphragm, and crossing of a certain positional threshold by the diaphragm triggers acquisition of a segment of the pre-defined 3D radial k-space trajectory. The k-space trajectory was organized as depicted in Fig. 4.6.
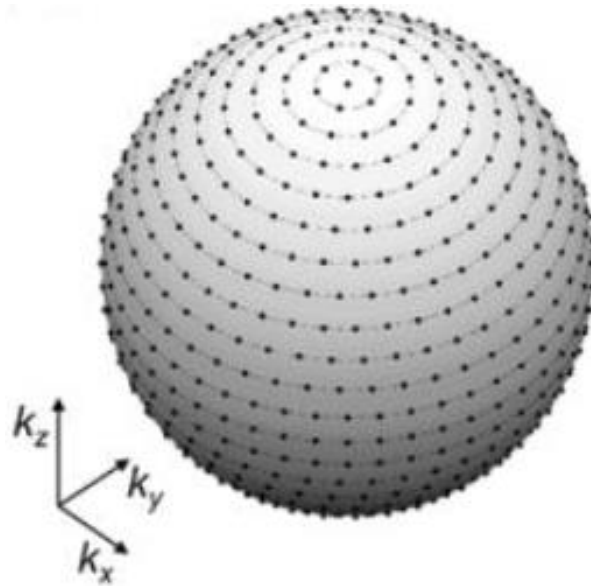
Figure 4.6: A k-space sphere depicting the endpoints of 3D radial k-space readout spokes corresponding to a fully-sampled 25×25×25 Cartesian k-space matrix. In practice, k-space is sampled far more densely than this, as the matrix size used in this study was 256×256×256. However, the general pattern (ray endpoints arranged in rings around the k_z poles) is maintained for any k-space sampling density. Reproduced from Miller et al (1).

All human studies complied with the Health Insurance Portability and Accountability Act and were approved by the University of Virginia Institutional Review Board, and all study subjects provided written, informed consent. 3D respiratory-triggered spoke-radial UTE bSSFP MRI was performed in 19 healthy individuals using a 1.5T whole-body scanner (Avanto; Siemens; Erlangen, DE). 3D respiratory-triggered spoke-radial UTE spoiled MRI was performed in 6/19 subjects for comparison.

Subjects were fitted with a vest-shaped array coil and positioned head-first supine inside the scanner. Standard localizer imaging was performed once subjects were positioned, to guide selection of an FOV that would fully encompass the lungs and to identify a diaphragm navigator window for PACE triggering (8). Subjects were instructed to breathe gently and comfortably

throughout the scan. Images were reconstructed on the scanner computer using a standard gridding-based procedure (24).

Signal properties of the bSSFP and spoiled UTE sequences were compared to one another by measuring mean signals in parenchyma, vessel, and noise regions in manually-defined regions-of-interest from triggered 3D images collected in the subset of six subjects that were imaged using both bSSFP and spoiled triggered sequences. Mean parenchyma (vasculature) signal divided by mean noise signal was used to approximate SNR of parenchyma (vasculature). A paired-sample t-test was used to compare approximate SNR of parenchyma and vasculature between bSSFP and spoiled images.

4.3.2. Results

Comparisons of approximate SNR in parenchyma and vasculature are shown in Fig. 4.7a-b for the six subjects in which both triggered 3D UTE bSSFP and triggered 3D UTE spoiled imaging was performed. Approximate SNR was higher for bSSFP than for spoiled imaging, both individually and groupwise ($p<0.001$ for both tissue types using a paired-samples t-test). Fig. 4.7c-d depicts a paired set of triggered bSSFP and spoiled images, in which qualitative vasculature and parenchyma contrast is higher for bSSFP than for spoiled imaging.
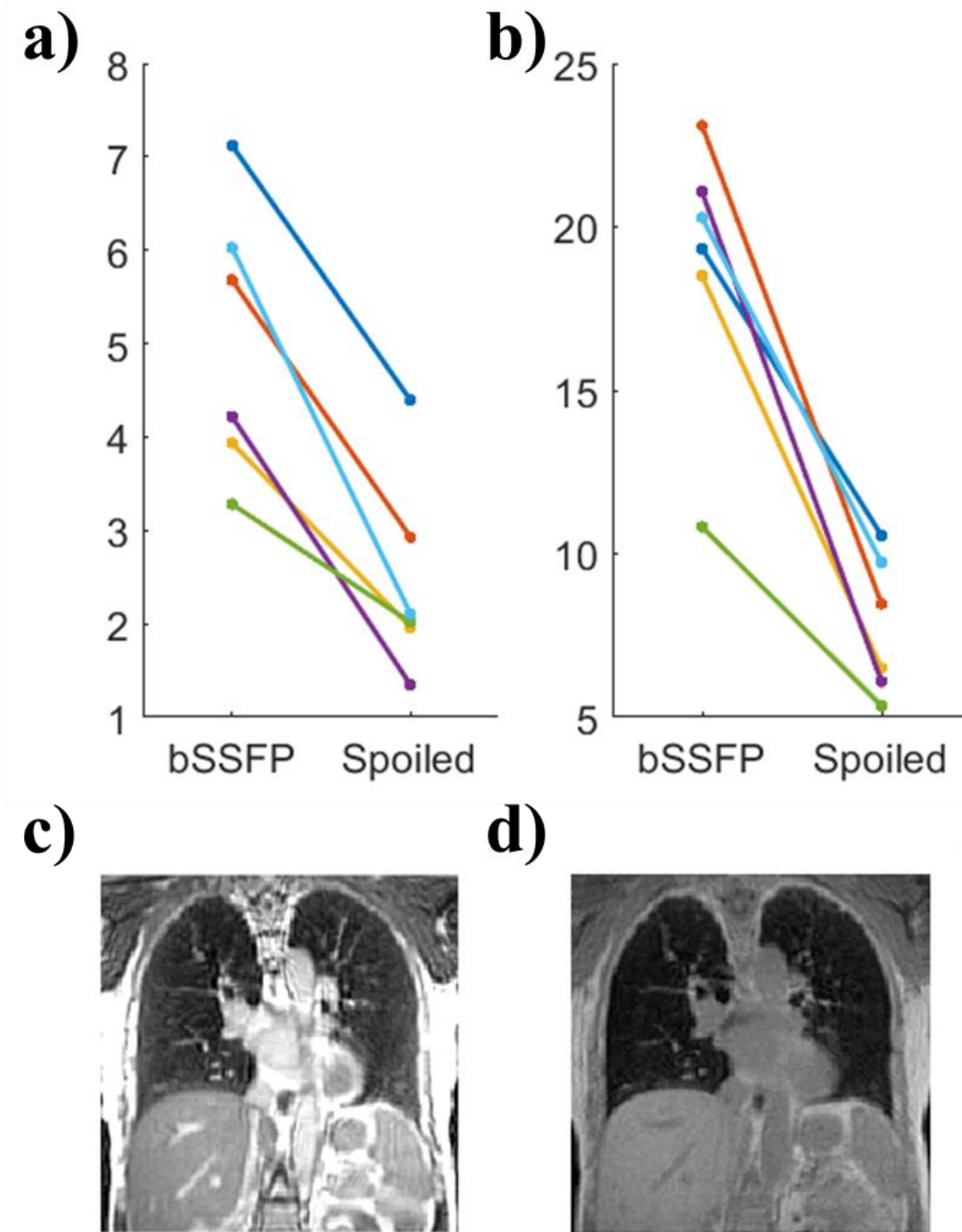
Figure 4.7: Approximate signal-to-noise ratio (SNR) of triggered bSSFP UTE and spoiled UTE images in **a)** lung parenchyma and **b)** vasculature, where individual subjects are represented by different colors, and each line in a subplot connects the bSSFP and spoiled SNR values for an individual subject. **c)** Coronal frame from a triggered bSSFP UTE image. **d)** Corresponding coronal frame from a triggered spoiled UTE image taken in the same individual as in c).

4.4. Free-breathing 4D lung MRI

4.4.1. Acquisition methods

Free-breathing 4D radial UTE bSSFP and spoiled MR data sets were acquired using identical pulse sequences and parameters to those shown in Fig. 4.5 and described in section 4.3.1.

In order to facilitate randomized, yet relatively even, coverage of k-space for each retrospectively-binned respiratory-phase image, spoke-radial k-space readouts were organized into passes using a spiral phyllotaxis-based approach (25,26). Construction of the spiral phyllotaxis passes was performed as follows:

Let the entire trajectory consist of $N{\times}R$ radial spokes, where N is the number of spiraling passes to use and R is the number of spokes assigned to each pass. Construct an ordered vector of polar angles $\boldsymbol{\theta}$ of length equal to $N{\times}R$ as follows:

$$\theta_m = \begin{cases} \dfrac{\pi}{\sqrt{2}} \cdot \sqrt{\dfrac{m-1}{NR-1}} & for\ 1 \le m < \dfrac{NR}{2} \\[4mm] \pi - \dfrac{\pi}{\sqrt{2}} \cdot \sqrt{\dfrac{NR-m}{NR-1}} & for\ \dfrac{NR}{2} \le m \le NR \end{cases} \tag{4.4}$$

such that $\theta_{NR} = \pi$ (i.e., setting the final spoke to lie on the negative k_z-axis).

Construct a corresponding vector of azimuthal angles $\boldsymbol{\varphi}$ of length equal to $N{\times}R$ by starting with $\varphi_1 = 0$ and incrementing each sequential azimuthal angle φ_m by a golden angle:

$$\Delta\varphi = 180° \cdot (3 - \sqrt{5}) \approx 137.51° \tag{4.5}$$

relative to the previous angle φ_{m-1}.

Once $\boldsymbol{\theta}$ and $\boldsymbol{\varphi}$ have been constructed, assign pairs of angles to each pass as follows, where n is a pass number between 1 and N:

$$\boldsymbol{\theta}(\boldsymbol{n}) = \{\boldsymbol{\theta}_{jN+n} \mid j \in \mathbb{Z}_0^+, j < R\} \tag{4.6}$$

$$\boldsymbol{\varphi(n)} = \left\{ \boldsymbol{\varphi}_{jN+n} \mid j \in \mathbb{Z}_0^+, j < R \right\}$$

That is, for the first pass in a trajectory consisting of $N = 898$ passes, assign the 1st, 899th, 1797th, etc., entries in $\boldsymbol{\theta}$ and $\boldsymbol{\varphi}$ to $\boldsymbol{\theta(1)}$ and $\boldsymbol{\varphi(1)}$, respectively. For large pass and ray numbers, this organization of ray angles into passes will create a series of passes incremented by an azimuthal angle $\Delta\varphi \approx 137.51°$ and by a very slight polar angle. The number of passes $N = 898$ was chosen to ensure that a steady state was maintained within passes (i.e., ray-to-ray angle jumps within a pass were small), while still spiraling slightly throughout the pass in order to ensure that a diverse set of k-space regions was sampled within each pass. Fig. 4.8 illustrates passes resulting from this ray organization scheme, as well as from a number of passes N nearly equal to 898 that resulted in poor maintenance of a steady state. 376 k-space samples were taken along each radial ray.
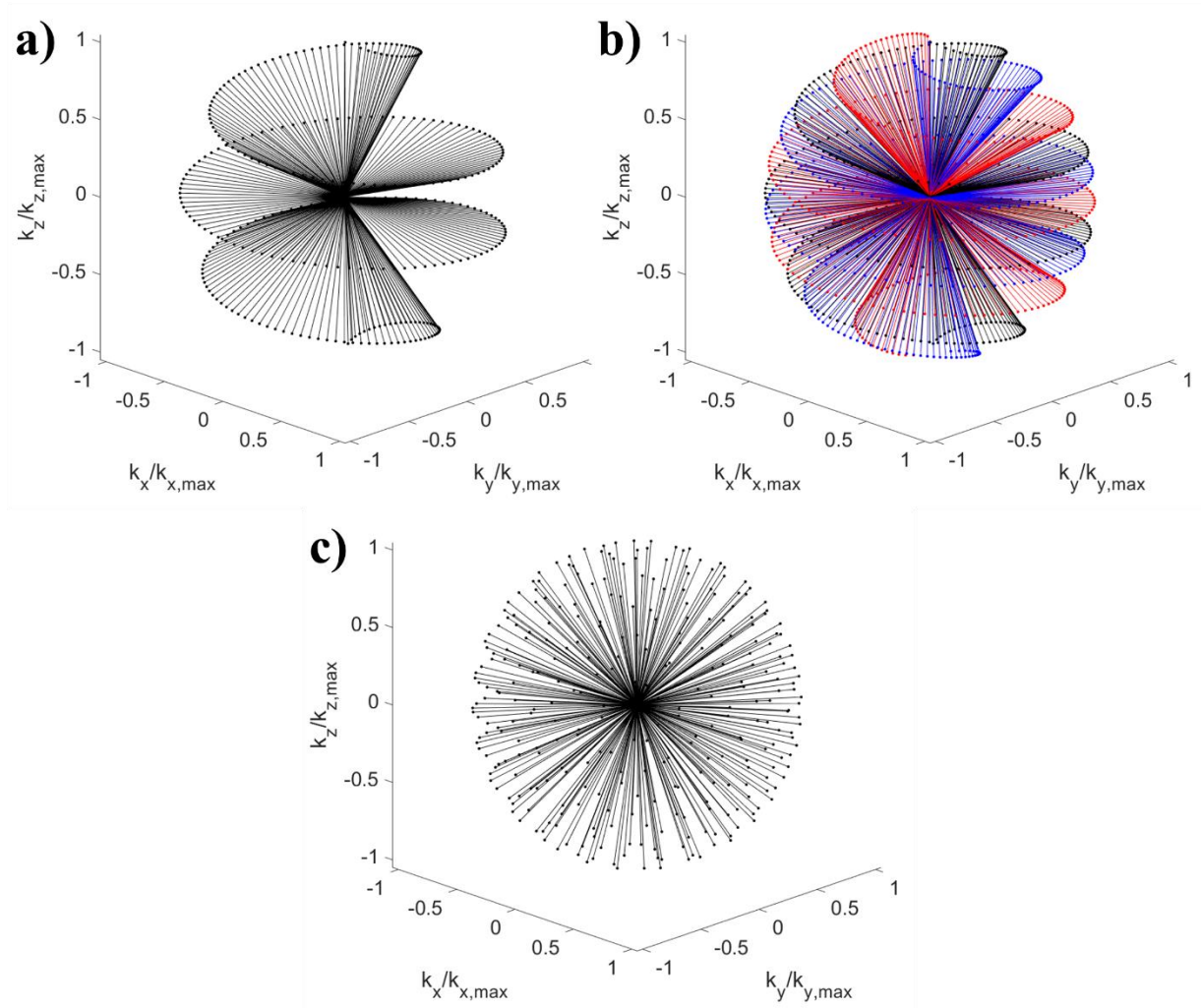
Figure 4.8: **a)** *k*-space spokes composing the first spiral phyllotaxis pass in a trajectory that uses 304 spokes per pass and 898 passes. **b)** *k*-space spokes composing the first (black), second (red), and third (blue) spiral phyllotaxis pass in the same trajectory as in a). **c)** *k*-space spokes composing the first spiral phyllotaxis pass in a trajectory that uses 304 spokes per pass and 895 passes. Jumps between individual *k*-space spokes for this set of trajectory parameters are much larger than for those for the set of parameters used to generate the trajectory shown in a).

This study complied with the Health Insurance Portability and Accountability Act and was approved by the University of Virginia Institutional Review Board, and all subjects provided written, informed consent. MRI was performed in 27 healthy individuals using a 1.5T whole-body scanner (Avanto; Siemens; Erlangen, DE). Free-breathing 4D spoke-radial UTE bSSFP MRI was performed in all subjects. Free-breathing 4D spoke-radial UTE spoiled MRI was performed for comparison in 11/27 subjects.

As in section 4.3.1, subjects were fitted with a vest-shaped array coil and positioned head-first supine inside the scanner, and localizer imaging was performed once subjects were positioned to guide FOV. Subjects were instructed to breathe gently and comfortably throughout the scan.

4.4.2. Reconstruction methods

MR k-space readouts collected during free breathing were retrospectively binned into respiratory phases in order to perform respiratory phase-resolved reconstruction. Two approaches were used for respiratory binning: one in which passes were binned using a k_0-based navigator derived from data collected during the 3D passes, and one in which passes were binned using 2D navigator images collected prior to each 3D pass. Both methods are described below:

- *k_0-based navigator:* All data taken at k_0 for a given pass and a given coil was averaged into a single k_0 number for each pass and coil. A median filter was then applied to the passwise k_0 timecourse for each coil to remove k_0 drift. The filtered k_0 signal timecourses for each coil were then correlated with one another to form a correlation matrix. The timecourses corresponding to the coil that had the most correlation coefficients above a chosen threshold (usually 0.85), as well as all of the coils that shared a correlation coefficient above the threshold with that coil, were normalized and then averaged into a single timecourse that was considered to contain the respiratory signal. Principal component analysis (PCA) was then performed on this timecourse, and the most dominant principal component was extracted and considered to represent the respiratory signal. The highest and lowest ~2% of values in the timecourse were excluded, and the remaining timepoints were ordered and assigned respiratory phase labels. Optionally, prior to binning, the local derivative of the timecourse at each point was used to determine whether a particular timepoint occurred during inhalation or exhalation, and timepoints were divided into inhalation and exhalation bins prior to more granular binning into inhalation- and exhalation-specific respiratory phases.

- *2D navigator images:* Initial 2D coronal navigator images were reconstructed for each pass by defining and executing a non-uniform fast Fourier transform (NUFFT) for each navigator image (27). These images were denoised by performing a GRASP reconstruction (15) with a temporal total variation penalty term to minimize temporal variations due to radial under-sampling artifacts. PCA was then performed on the N-by-M

time series composed of the vectorized denoised images, where N was the number of timepoints (passes) and M was the number of voxels in each image, and the 6 strongest components were used to define a compressed subspace in which to represent the denoised images. A spatial region of interest (ROI) that included the entire range of positions of the diaphragm during breathing was identified. The image portions of the subspace-represented navigator images corresponding to the ROI were then vectorized to produce an N-by-M_{ROI} time series, where M_{ROI} is the number of voxels in the ROI. Initial clustering of the vectorized ROI images into P respiratory phases was performed using k-means (28,29), producing a P-by-M_{ROI} initial cluster centers. To group the vectorized images into equally-sized clusters, the initial cluster centers were replicated N/P times in order to produce a cluster center matrix of identical size to the N-by-M_{ROI} ROI time series. ROI images were then matched with cluster centers by solving the linear assignment problem (30) using a squared-Euclidean distance metric, producing final respiratory phase labels for the navigator image series.

To generate coil sensitivity maps for multi-coil acquisitions, an NUFFT with uniform coil sensitivity weighting was defined and used to reconstruct individual coil images from the full, non-respiratory binned k-space data for each coil. Complex coil sensitivity maps were then calculated using an iterative adaptive-combination-based approach (31) and included in the NUFFT objects defined for subsequent steps.

Respiratory-phase-resolved image frames were reconstructed as a series using an adaptation of the XD-GRASP-Pro approach (19,20). To obtain a temporal basis to be used in the final optimization, an initial XD-GRASP (16) reconstruction was performed using the low-resolution k-space readouts (defined as all readouts taken at $0 \leq |k| \leq |k|_{\max}/4$) contained in each respiratory phase bin. An optimal solution for the low-resolution image series m_L was found by solving the following minimization problem:

$$\widetilde{m}_L = \arg \min_{m_L} \frac{1}{2} \|E_L m_L - y_L\|_2^2 + \lambda_{TVt,1} \|TV_t(m_L)\|_1 \qquad (4.7)$$

where E_L is a multi-coil NUFFT operator defined for the low-resolution sampled k-space points that incorporates coil sensitivities and radial density compensation, y_L is the sampled low-

resolution k-space data, $\lambda_{TVt,1}$ is a weighting coefficient applied to the L_1 penalty term, and TV_t represents a temporal total variation operator applied to the low-resolution image series m_L.

Following optimization, the optimal low-resolution image series m_L was organized into a 2D matrix of size N-by-M, where N is the number of respiratory phase bins and M is the number of voxels per image frame. PCA was then performed on m_L in order to identify a temporal basis corresponding to the low-resolution image series:

$$m_L = UV_L \qquad (4.8)$$

where U is the N-by-N temporal basis and V_L is the N-by-M set of coefficients that represent the image m_L under U. The small number of significantly nonzero singular values indicates that the image can be reasonably approximated using only the first K dominant basis components, where $K \ll N$ (most commonly for this work, $K = 6$ and $N = 25$):

$$m_L = UV_L \approx U_K V_{LK} \qquad (4.9)$$

where U_K is the N-by-K temporal basis and V_{LK} is the K-by-M set of coefficients that best approximate the image m_L under U_K.

After the low-rank basis U_K is then estimated, the full-resolution image series m is reconstructed by setting $m = U_K V_K$, where V_K is the matrix of subspace coefficients that best represent the image series m under U_K, and by then solving an XD-GRASP-based minimization of V_K, as follows:

$$\tilde{V}_K = \arg\min_{V_K} \frac{1}{2} \|E(U_K V_K) - y\|_2^2 + \lambda_{TVt,2} \|TV_t(U_K V_K)\|_1 \\ + \lambda_{TVs} \|TV_s(V_K)\|_1 \qquad (4.10)$$

where E is a multi-coil NUFFT operator defined for the entire set of sampled k-space points that incorporates coil sensitivities and radial density compensation, y is the sampled k-space data, $\lambda_{TVt,2}$ is a weighting coefficient applied to the L_1 temporal total variation penalty term, TV_t represents a temporal total variation operator applied to $U_K V_K$ (m as best approximated in the

subspace defined by U_K), λ_{TVs} is a weighting coefficient applied to the L_1 spatial total variation penalty term, and TV_s represents a spatial total variation operator applied to V_K.

Both optimizations were solved using the nonlinear conjugate gradient method (32,33). For the low-resolution optimization, a total of eight iterations was used. For the full-resolution optimization, a total of 24 iterations (three outer loops each consisting of eight iterations) was used, with the optimization procedure reset upon completing each instance of the outer loop.

4D image series reconstructed using XD-GRASP-Pro were compared with series reconstructed using standard XD-GRASP and with triggered 3D images collected in the same individual using the same pulse sequence parameters.

4.4.3. Results

Coronal and sagittal views from a reconstructed 4D bSSFP image frame at end-of-exhalation are shown alongside a 3D triggered frame taken at end-of-exhalation from the same individual in Fig. 4.9. Under-sampling artifacts are highly reduced in image frames from the 4D image set reconstructed using XD-GRASP-Pro, and appearance of the end-of-exhalation frame closely matches that of the triggered image. Freezing of diaphragm motion appears slightly more effective in the XD-GRASP-Pro 4D reconstruction than in the triggered image, possibly due to small variance in the motion states captured during the acquisition windows of the triggered scan.
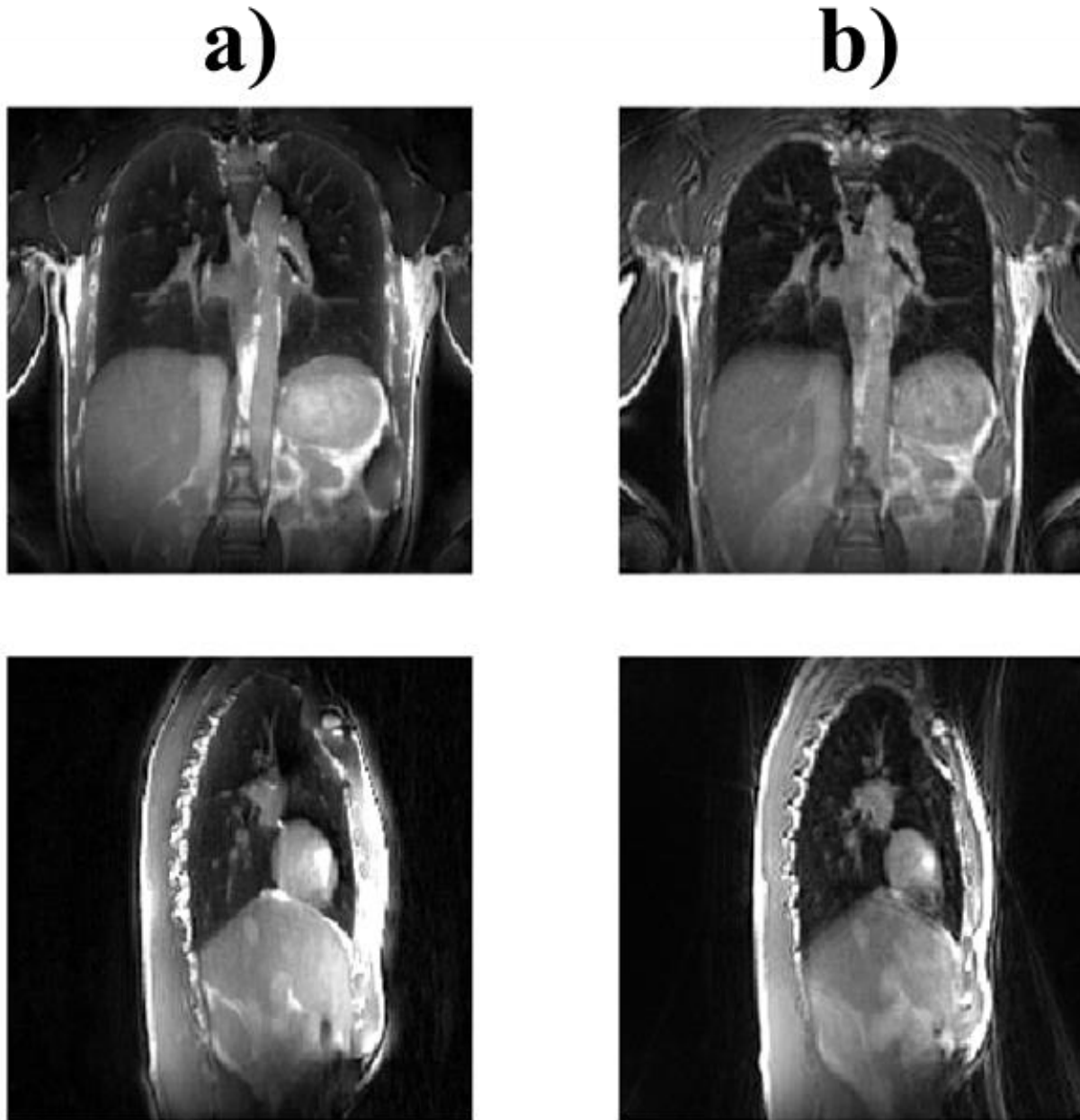
Figure 4.9: **a)** Coronal (top) and sagittal (bottom) frames reconstructed at end-of-exhalation from free-breathing 4D ultrashort echo time (UTE) balanced steady-state free precession (bSSFP) MRI using XD-GRASP-Pro. **b)** Coronal (top) and sagittal (bottom) end-of-exhalation frames from respiratory-triggered 3D UTE bSSFP MRI.

Fig. 4.10 depicts reconstructed image frames from all respiratory phases from the 4D bSSFP image series shown in Fig. 4.9. Blurring of the diaphragm and large blood vessels is still apparent in the image frames from the 4D image set that were taken at end-of-inhalation and at intermediate points in the breathing cycle.

139
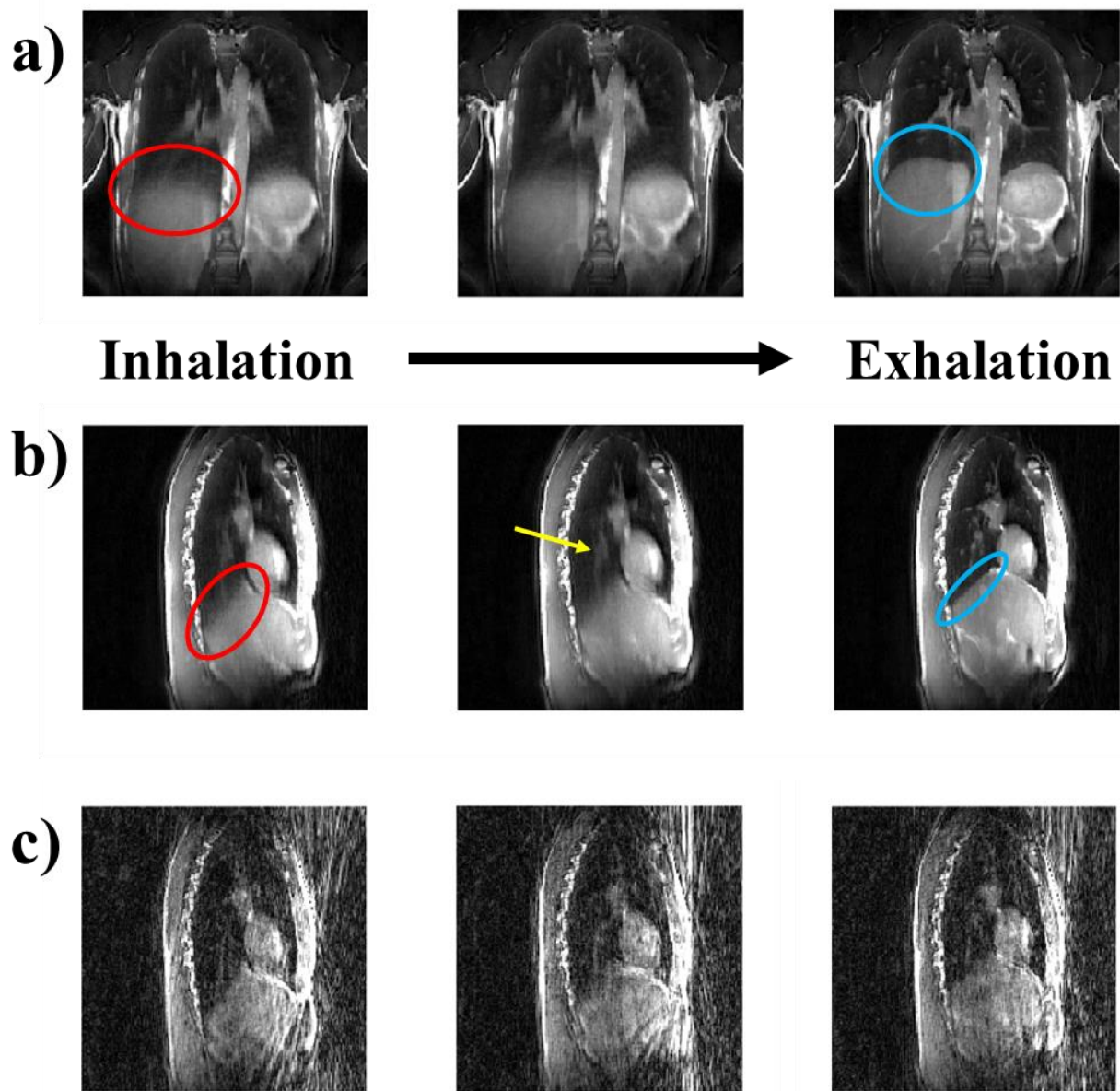
Figure 4.10: **a)** Coronal and **b)** sagittal frames reconstructed at different respiratory phases from free-breathing 4D ultrashort echo time (UTE) balanced steady-state free precession (bSSFP) MRI using XD-GRASP-Pro. Significant diaphragm blurring (red circles) is seen in the intermediate and end-of-inhalation frames, while diaphragm sharpness is maintained in the end-of-exhalation frame (blue circles). Vessel blurring is also apparent in the non-end-of-exhalation frames (yellow arrow). **c)** Under-sampled sagittal frames shown in b) prior to XD-GRASP-Pro reconstruction. Widespread streaking artifacts apparent in c) are essentially eliminated in the reconstructions depicted in a) and b).

Image series reconstructed using both XD-GRASP-Pro and standard XD-GRASP are shown in Fig. 4.11. Similar image quality was observed between the two reconstruction approaches. Slightly better vasculature definition at end-of-exhalation can be seen in XD-GRASP-Pro-reconstructed images, while slightly lower blurring of the vasculature and diaphragm at non-end-of-exhalation images is apparent in XD-GRASP-reconstructed images.
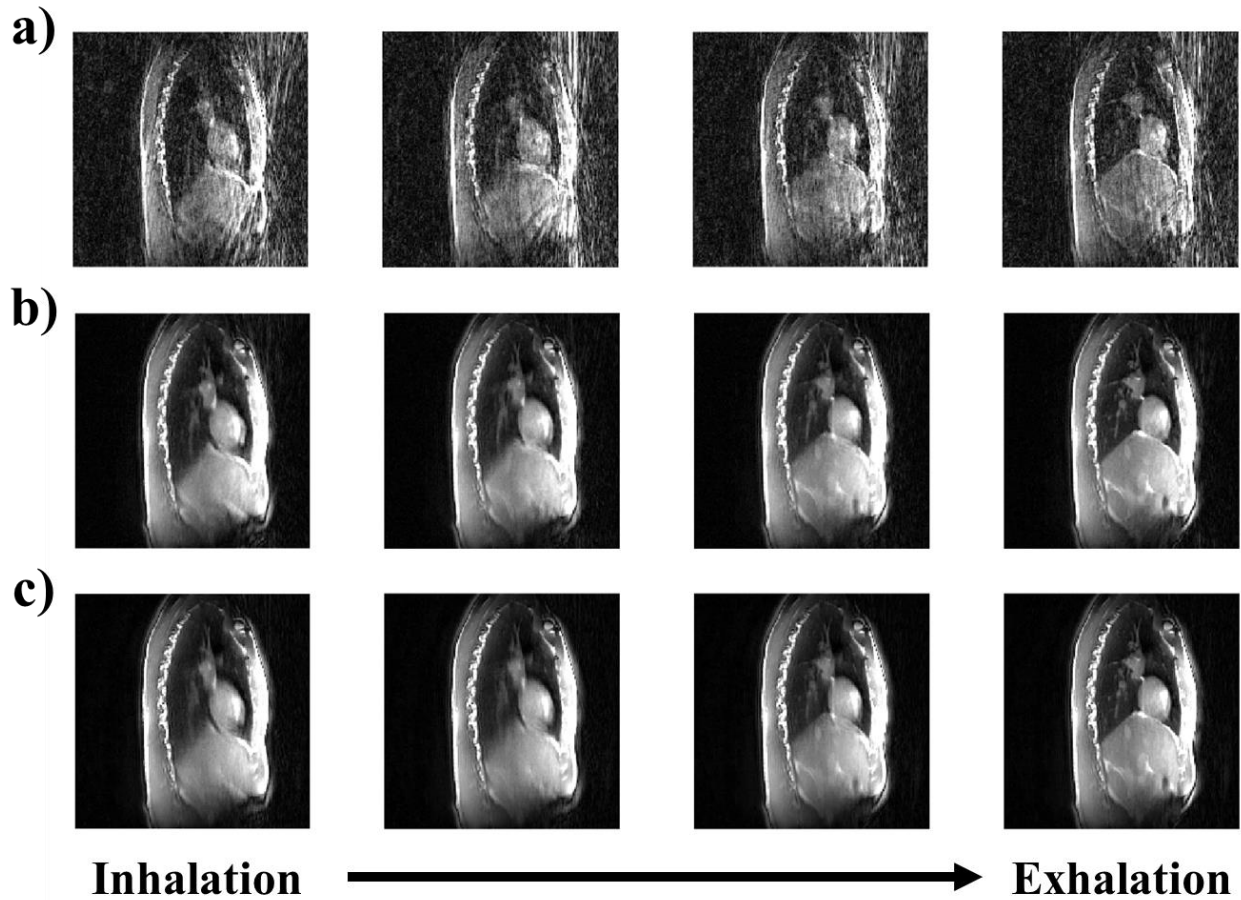
Figure 4.11: **a)** Under-sampled sagittal frames from free-breathing 4D ultrashort echo time (UTE) balanced steady-state free precession (bSSFP) MRI prior to constrained reconstruction. **b)** Sagittal frames shown in a) after being reconstructed using XD-GRASP. **c)** Sagittal frames shown in a) after being reconstructed using XD-GRASP-Pro.

Fig. 4.12 depicts coronal and sagittal views from reconstructed 4D UTE bSSFP and UTE spoiled images collected in the same individual. Higher vessel and parenchyma visibility is observed for the UTE bSSFP than the UTE spoiled images, with vessel definition particularly improved in the UTE bSSFP images as seen in the maximum intensity projections shown in Fig. 4.12a-b.
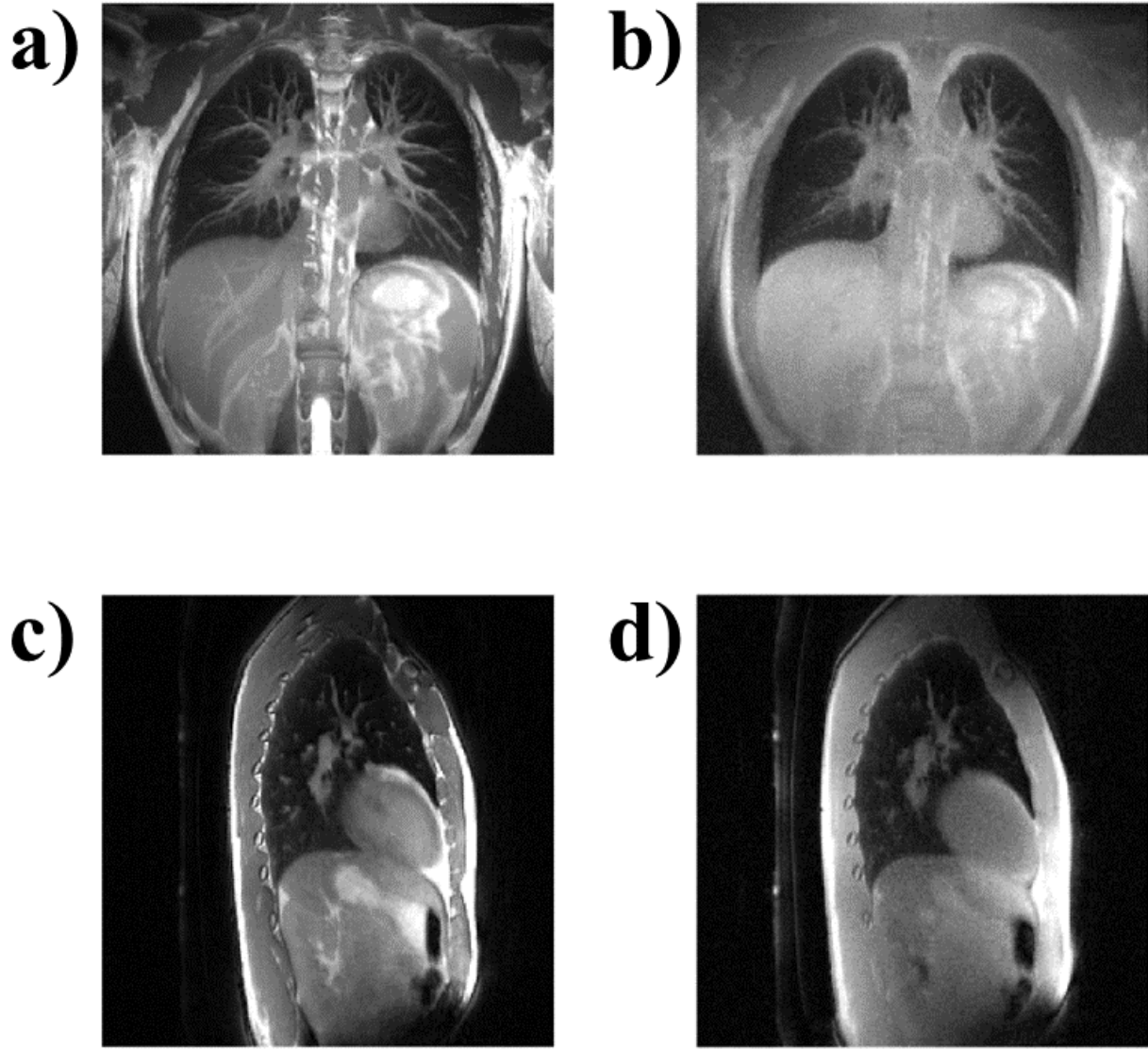
Figure 4.12: Coronal maximum intensity projections (MIPs) from **a)** ultrashort echo time (UTE) balanced steady-state free precession (bSSFP) MRI and **b)** UTE spoiled MRI, as well as sagittal frames from **c)** UTE bSSFP MRI and **d)** UTE spoiled MRI, reconstructed at end-of-exhalation from free-breathing data.

4.5. Discussion

The UTE bSSFP pulse sequence displayed higher signal and feature contrast than the UTE spoiled sequence, particularly for pulmonary blood vessels, in general agreement with simulations of the pulse sequences used in this work. Banding artifacts characteristic of bSSFP are heavily mitigated by the short TR and by the phase dispersion of parenchyma spins during the TR window, avoiding one of the key downsides of bSSFP.

MRI of the lung using prospective respiratory triggering is generally effective at freezing lung motion, but prolongs scan times significantly and only permits visualization of the lung at one respiratory phase. Images reconstructed from free-breathing data using a method that takes advantage of temporal sparsity can closely replicate fully-sampled images collected using respiratory triggering, as demonstrated here, permitting shorter scan times at the cost of significant computational time relative to the scanner-computer reconstructions of triggered 3D images. Continuously-acquired free-breathing data can also potentially be used to reconstruct high-quality images at several respiratory phases, although the techniques used in this work were only somewhat effective and significant blurring was noted in non-end-of-exhalation frames.

While all images shown in this work were reconstructed using only data sampled during the first lobe of the readout gradient (i.e., traversing k-space from center to periphery), it is clearly possible to sample k-space during the rewound portion of the readout gradient (i.e., retracing k-space from periphery to center). Future work might seek to incorporate data sampled during the retracing of each ray from the k-space periphery to the center. Doing so would require careful measurement of the executed k-space trajectory, as outbound lines would likely not exactly match corresponding inbound lines, and would require that the differing phase of the two readout sets be incorporated into the reconstruction (34).

Residual blurring was still evident after XD-GRASP-Pro reconstruction in frames not taken at end-of-exhalation. Improved respiratory binning would likely improve image sharpness, as the methods used in this work often struggled to precisely bin readouts taken at non-end-of-exhalation respiratory phases. That said, the length of time taken to execute each spiralling pass (roughly one second) likely results in a non-trivial degree of motion captured even within individual passes. Future work might seek to optimize the number of rays sampled per pass, weighting the need to minimize time taken per pass to minimize within-pass motion against the need to maintain a steady state by minimizing the distance between sequential rays in each pass.

Additionally, it can be observed that, for image regions of minimal motion, the temporal finite-difference from frame to frame is low, and the temporal finite-difference operator is an effective sparsifying transform; but for image regions that display significant motion through the breathing cycle, the temporal finite-difference operator enforces sparsity less effectively. Residual blurring from respiratory motion within bins, as well as possible reconstruction-induced blurring, could

therefore be better mitigated via adaptive weighting of temporal vs. spatial finite-differences such that temporal differences take stronger weight for regions of minimal motion, and spatial differences take stronger weight for regions of significant motion (35,36). Alternative sparsifying transforms on the image or on the subspace coefficient matrix could be tested and used as well. An early version of the XD-GRASP-Pro implementation shown in this work examined a temporal Fourier transform to enforce temporal sparsity in the image series, with results generally similar to those shown above using temporal finite-differences.

Another potential solution to blurring in reconstructed image frames would be the incorporation of motion fields relating the high-quality end-of-exhalation image to the other frames, a motif seen in other 4D MRI reconstruction approaches (12,36–38). The desired 4D image could be taken to be the registration of the end-of-exhalation image to all respiratory phases. Alternatively, if continuing to use an XD-GRASP-Pro-based approach, the temporal subspace could be generated from a time series composed of deformed copies of an end-of-exhalation frame matched to each of the pseudo-temporal frames, and this alternative subspace could then be used for a typical XD-GRASP-Pro reconstruction of the original pseudo-temporal frames.

The work shown here was performed in a 1.5 T magnet, which was chosen over a 3 T magnet because of the higher T_2^* of lung parenchyma at a lower field strength and to further mitigate banding artifacts due to field inhomogeneities for bSSFP imaging. Interest has recently developed in performing lung MRI at yet lower field strengths, and an increasing body of literature is being produced on lung MRI at 0.55 T (39–41). The bSSFP sequence described in this work could be adapted in straightforward fashion to MRI at 0.55 T, improving the robustness to banding artifacts that is already increased using this spoke-radial bSSFP method due to its short TR.

In this work, we demonstrated a free-breathing proton lung MRI approach that maximizes parenchyma and vessel signal in the lungs, combining a 3D UTE bSSFP pulse sequence with a GRASP-Pro-based reconstruction algorithm applied to respiratory phase-binned data. This approach produced high-signal, high-resolution lung images at end-of-exhalation collected during free breathing. While non-end-of-exhalation reconstruction was less effective using the methods investigated here, a similar reconstruction algorithm that additionally incorporates

motion fields or improved sparsifying transforms could improve results at these respiratory phases.

4.6. References

1. Miller GW, Mugler III JP, Sá RC, Altes TA, Prisk GK, Hopkins SR. Advances in functional and structural imaging of the human lung using proton MRI. NMR in Biomedicine. 2014;27(12):1542–56.

2. Robson MD, Gatehouse PD, Bydder M, Bydder GM. Magnetic resonance: an introduction to ultrashort TE (UTE) imaging. J Comput Assist Tomogr. 2003;27(6):825–46.

3. Dournes G, Grodzki D, Macey J, Girodet PO, Fayon M, Chateil JF, et al. Quiet Submillimeter MR Imaging of the Lung Is Feasible with a PETRA Sequence at 1.5 T. Radiology. 2015 Jul;276(1):258–65.

4. Wu C, Krishnamoorthy G, Yu V, Subashi E, Rimner A, Otazo R. 4D lung MRI with high-isotropic-resolution using half-spoke (UTE) and full-spoke 3D radial acquisition and temporal compressed sensing reconstruction. Phys Med Biol. 2023 Jan 27;68(3).

5. Scheffler K, Lehnhardt S. Principles and applications of balanced SSFP techniques. Eur Radiol. 2003 Nov;13(11):2409–18.

6. Bieri O. Ultra-fast steady state free precession and its application to in vivo 1H morphological and functional lung imaging at 1.5 tesla. Magnetic Resonance in Medicine. 2013;70(3):657–63.

7. Failo R, Wielopolski PA, Tiddens HAWM, Hop WCJ, Mucelli RP, Lequin MH. Lung morphology assessment using MRI: a robust ultra-short TR/TE 2D steady state free precession sequence used in cystic fibrosis patients. Magn Reson Med. 2009 Feb;61(2):299–306.

8. Klessen C, Asbach P, Kroencke TJ, Fischer T, Warmuth C, Stemmer A, et al. Magnetic resonance imaging of the upper abdomen using a free-breathing T2-weighted turbo spin echo sequence with navigator triggered prospective acquisition correction. J Magn Reson Imaging. 2005 May;21(5):576–82.

9. Lustig M, Santos JM, Donoho DL, Pauly JM. k-T SPARSE: High Frame Rate Dynamic MRI Exploiting Spatio-Temporal Sparsity.

10. Feng L, Srichai MB, Lim RP, Harrison A, King W, Adluru G, et al. Highly accelerated real-time cardiac cine MRI using k-t SPARSE-SENSE. Magn Reson Med. 2013 Jul;70(1):64–74.

11. Paul J, Divkovic E, Wundrak S, Bernhardt P, Rottbauer W, Neumann H, et al. High-resolution respiratory self-gated golden angle cardiac MRI: Comparison of self-gating

methods in combination with k-t SPARSE SENSE. Magn Reson Med. 2015 Jan;73(1):292–8.

12. Zhu X, Chan M, Lustig M, Johnson K, Larson P. Iterative Motion Compensation reconstruction ultra-short TE(iMoCo UTE) for high resolution free breathing pulmonary MRI. Magn Reson Med. 2020 Apr;83(4):1208–21.

13. Arai TJ, Nofiele J, Madhuranthakam AJ, Yuan Q, Pedrosa I, Chopra R, et al. Characterizing spatiotemporal information loss in sparse-sampling-based dynamic MRI for monitoring respiration-induced tumor motion in radiotherapy. Med Phys. 2016 Jun;43(6):2807–20.

14. Feng L, Delacoste J, Smith D, Weissbrot J, Flagg E, Moore WH, et al. Simultaneous Evaluation of Lung Anatomy and Ventilation Using 4D Respiratory-Motion-Resolved UTE Sparse MRI. J Magn Reson Imaging. 2019 Feb;49(2):411–22.

15. Feng L, Grimm R, Block KT, Chandarana H, Kim S, Xu J, et al. Golden-angle radial sparse parallel MRI: combination of compressed sensing, parallel imaging, and golden-angle radial sampling for fast and flexible dynamic volumetric MRI. Magn Reson Med. 2014 Sep;72(3):707–17.

16. Feng L, Axel L, Chandarana H, Block KT, Sodickson DK, Otazo R. XD-GRASP: Golden-angle radial MRI with reconstruction of extra motion-state dimensions using compressed sensing. Magnetic Resonance in Medicine. 2016;75(2):775–88.

17. Chen L, Liu D, Zhang J, Xie B, Zhou X, Grimm R, et al. Free-Breathing Dynamic Contrast-Enhanced MRI for Assessment of Pulmonary Lesions Using Golden-Angle Radial Sparse Parallel Imaging. J Magn Reson Imaging. 2018 Aug;48(2):459–68.

18. Chandarana H, Feng L, Ream J, Wang A, Babb JS, Block KT, et al. Respiratory Motion-Resolved Compressed Sensing Reconstruction of Free-Breathing Radial Acquisition for Dynamic Liver Magnetic Resonance Imaging. Invest Radiol. 2015 Nov;50(11):749–56.

19. Feng L, Wen Q, Huang C, Tong A, Liu F, Chandarana H. GRASP-Pro: imProving GRASP DCE-MRI through self-calibrating subspace-modeling and contrast phase automation. Magn Reson Med. 2020 Jan;83(1):94–108.

20. Feng L, Liu F. High spatiotemporal resolution motion-resolved MRI using XD-GRASP-Pro. In: Proc Intl Soc Mag Reson Med 28. 2020. p. 597.

21. Theilmann RJ, Arai TJ, Samiee A, Dubowitz DJ, Hopkins SR, Buxton RB, et al. Quantitative MRI measurement of lung density must account for the change in T with lung inflation. Journal of Magnetic Resonance Imaging. 2009;30(3):527–34.

22. Bauman G, Santini F, Pusterla O, Bieri O. Pulmonary relaxometry with inversion recovery ultra-fast steady-state free precession at 1.5T. Magnetic Resonance in Medicine. 2017;77(1):74–82.

23. Spees WM, Yablonskiy DA, Oswood MC, Ackerman JJH. Water proton MR properties of human blood at 1.5 Tesla: Magnetic susceptibility, T1, T2, T, and non-Lorentzian signal behavior. Magnetic Resonance in Medicine. 2001;45(4):533–42.

24. Jackson JI, Meyer CH, Nishimura DG, Macovski A. Selection of a convolution function for Fourier inversion using gridding [computerised tomography application]. IEEE Trans Med Imaging. 1991;10(3):473–8.

25. Piccini D, Littmann A, Nielles-Vallespin S, Zenge MO. Spiral phyllotaxis: The natural way to construct a 3D radial trajectory in MRI. Magnetic Resonance in Medicine. 2011;66(4):1049–56.

26. Delacoste J, Chaptinel J, Beigelman-Aubry C, Piccini D, Sauty A, Stuber M. A double echo ultra short echo time (UTE) acquisition for respiratory motion-suppressed high resolution imaging of the lung. Magn Reson Med. 2018 Apr;79(4):2297–305.

27. Fessler JA, Sutton BP. Nonuniform fast fourier transforms using min-max interpolation. IEEE Trans Signal Process. 2003 Feb;51(2):560–74.

28. Lloyd S. Least squares quantization in PCM. IEEE Transactions on Information Theory. 1982 Mar;28(2):129–37.

29. Arthur D, Vassilvitskii S. k-means++: the advantages of careful seeding. In: Proceedings of the eighteenth annual ACM-SIAM symposium on Discrete algorithms. USA: Society for Industrial and Applied Mathematics; 2007. p. 1027–35. (SODA '07).

30. Duff IS, Koster J. On Algorithms For Permuting Large Entries to the Diagonal of a Sparse Matrix. SIAM J Matrix Anal Appl. 2001 Jan;22(4):973–96.

31. Inati SJ, Hansen MS, Kellman P. A fast optimal method for coil sensitivity estimation and adaptive coil combination for complex images. In: Proc Intl Soc Mag Reson Med 22. 2014. p. 4407.

32. Fletcher R, Reeves CM. Function minimization by conjugate gradients. The Computer Journal. 1964 Jan 1;7(2):149–54.

33. Dai YH, Yuan Y. A Nonlinear Conjugate Gradient Method with a Strong Global Convergence Property. SIAM J Optim. 1999 Jan;10(1):177–82.

34. Jung Y, Samsonov AA, Bydder M, Block WF. Self-calibrated multiple-echo acquisition with radial trajectories using the conjugate gradient method (SMART-CG). Journal of Magnetic Resonance Imaging. 2011;33(4):980–7.

35. Ritschl L, Sawall S, Knaup M, Hess A, Kachelrieß M. Iterative 4D cardiac micro-CT image reconstruction using an adaptive spatio-temporal sparsity prior. Phys Med Biol. 2012 Mar;57(6):1517.

36. Rank CM, Heußer T, Buzan MTA, Wetscherek A, Freitag MT, Dinkel J, et al. 4D respiratory motion-compensated image reconstruction of free-breathing radial MR data with very high undersampling. Magnetic Resonance in Medicine. 2017;77(3):1170–83.

37. Huttinga NRF, Bruijnen T, van den Berg CAT, Sbrizzi A. Nonrigid 3D motion estimation at high temporal resolution from prospectively undersampled k-space data using low-rank MR-MOTUS. Magnetic Resonance in Medicine. 2021;85(4):2309–26.

38. Miller Z, Johnson KM. Motion compensated self supervised deep learning for highly accelerated 3D ultrashort Echo time pulmonary MRI. Magn Reson Med. 2023 Jun;89(6):2361–75.

39. Bhattacharya I, Ramasawmy R, Javed A, Lowery M, Henry J, Mancini C, et al. Assessment of lung structure and regional function using 0.55T MRI in patients with lymphangioleiomyomatosis. Invest Radiol. 2022 Mar 1;57(3):178–86.

40. Campbell-Washburn AE, Malayeri AA, Jones EC, Moss J, Fennelly KP, Olivier KN, et al. T2-weighted Lung Imaging Using a 0.55-T MRI System. Radiol Cardiothorac Imaging. 2021 Jun 10;3(3):e200611.

41. Azour L, Condos R, Keerthivasan MB, Bruno M, Sood TP, Landini N, et al. Low-field 0.55 T MRI for assessment of pulmonary groundglass and fibrosis-like opacities: Inter-reader and inter-modality concordance. Eur J Radiol. 2022 Nov;156:110515.

Chapter 5: Conclusion and future work

5.1. Conclusion

This dissertation describes methodological advancements for three types of dynamic magnetic resonance imaging (MRI) of the human lung – multi-frame 3D hyperpolarized-gas (HPG) tagging MRI, 3D dissolved-phase ^{129}Xe MRI, and 4D free-breathing ^{1}H MRI.

Chapter 2 of this work demonstrates a method for performing 3D multi-phase MRI of grid-tagged hyperpolarized ^{3}He gas in the lungs during exhalation, as well as calculation of displacement and strain maps from resulting image series. The predictable distribution of k-space energy in the tagging MRI context is used to design a highly under-sampled 3D Cartesian matrix of k-space readouts, and a relatively simple compressed sensing (CS) approach is used to reconstruct under-sampled 3D image frames. This work represents the first extension of HPG tagging lung MRI to multi-frame 3D imaging, opening up increased possibilities for research and clinical applications.

Chapter 3 of this work characterizes the repeatability and lung volume dependence of dissolved-phase ^{129}Xe MRI of the lung, a technique for visualization and quantification of pulmonary gas exchange efficacy. Scan-to-scan repeatability of the three ^{129}Xe MRI-derived gas-uptake metrics is strong in general, but better when scan-to-scan lung volumes were tightly repeated. Strong lung volume dependence is observed for two of the three metrics, with these metrics closely following a linear relative-difference relationship for both healthy individuals and individuals with chronic obstructive pulmonary disease (COPD). A preliminary method for lung volume correction using this relative-difference relationship is theorized and demonstrated, and groupwise differences in these metrics between healthy individuals and those with COPD lessened upon accounting for lung volume contributions using this correction. This result highlights the importance of careful consideration of lung-volume effects on ^{129}Xe-derived gas uptake metrics, particularly in diseased populations that frequency present with hyperinflation such as COPD.

Chapter 4 of this work demonstrates a combined acquisition and reconstruction approach for performing free-breathing 4D ^{1}H MRI of the lung. Data is acquired using a 3D ultrashort echo

time (UTE) balanced steady-state free precession (bSSFP) spoke-radial pulse sequence, which displays higher signal-to-noise ratio in lung parenchyma and vasculature than a 3D UTE spoiled spoke-radial sequence. Spoke-radial readouts are organized into interleaved passes based on a spiral phyllotaxis trajectory, and data sorting into respiratory phases is performed using either a navigator based on the sampled signal near the k-space center or using a 2D image-based navigator interspersed between 3D spiral passes. Respiratory-phase-resolved image reconstruction is performed using two golden-angle radial sparse parallel (GRASP)-based CS techniques, XD-GRASP and XD-GRASP-Pro, which both take advantage of the temporal sparsity inherent in respiratory-resolved lung image series. High-quality end-of-exhalation reconstructions are produced using both reconstruction methods, with other respiratory phases displaying diaphragm and vasculature blurring. XD-GRASP displays slightly improved image sharpness at these frames, while XD-GRASP-Pro displays better denoising and removing of radial under-sampling artifacts for all respiratory phases. This approach is promising for high-signal free-breathing MRI of pulmonary structures, and is particularly interesting for characterization of lung parenchymal density and for serial imaging and characterization of lung tumor burden.

5.2. Future work

5.2.1. 3D multi-phase hyperpolarized-gas tagging lung MRI

Continued development of the image acquisition and analysis methods for HPG tagging MRI described in Chapter 2 would be a useful area of future work. Image acquisition could be hastened by using equal-amplitude instead of equal-time-width radiofrequency (RF) pulses (1), and signal-to-noise ratio (SNR) could be improved by using an array of small receive RF coils. Any further increases in acquisition speed per image frame could potentially be leveraged to image serially throughout both exhalation and an ensuing inhalation, rather than only during exhalation as demonstrated here. With regard to sampling and CS reconstruction design, under-sampling artifacts prior to CS might be further mitigated by implementing data-driven learning of sampling patterns (2), and image reconstruction accuracy could be improved by optimizing hyperparameters in the CS reconstruction, such as the weighting factor λ for the L_1 term. Tag tracking through the image series could also be improved, and ideally an automated or semi-

automated approach (3) might be implemented to facilitate more robust and accurate tag tracking and associated displacement map generation.

In addition to methodological improvements, testing in diseased populations and for specific applications is an important goal. Initial work in healthy individuals has evaluated lung displacement fields generated using two-phase HPG tagging MRI alongside those generated using two-phase ^{1}H MR images collected during the same breathing maneuver as the HPG tagging MR images and co-registered to one another using deformable image registration (DIR) algorithms (4). These results indicated that displacement fields generated using DIR of ^{1}H MR images varied significantly depending on the particular DIR algorithm used, and that all DIR-based displacement fields differed from displacement fields generated from HPG tagging MR images collected in the same breathing maneuver. Similar work evaluating the 3D multi-phase tagging methods demonstrated in Chapter 2 as a readout of DIR-based lung displacement field accuracy, in both healthy individuals and those with lung cancer, represents a possible next step for this work.

5.2.2. Dissolved-phase ^{129}Xe lung MRI

The results shown in this work indicate that lung-volume differences between scans and between individuals must be considered when developing comparisons of ^{129}Xe-derived gas uptake metrics between individuals and between groups. While there is some limited ability for clinicians and researchers to control lung volume during studies by providing breathing instructions to the subjects and by providing specific gas volumes for inhalation, these results demonstrate that actual inflation levels during scans may differ significantly from the intended inflation level, particularly for intermediate inflation levels such as one-third of forced vital capacity.

Given the above, it is important that robust retrospective correction can be applied to account for lung volume contributions to ^{129}Xe MRI-derived gas uptake metrics. While the lung-volume correction approach suggested in this work is a useful start, it would be ideal to develop a more detailed model with specific underpinnings in pulmonary physiology and/or a more sophisticated, distribution-driven approach (5). It is theorized in this and in prior work (6) that lung volume differences between individuals, and between inflation levels within individuals, are

driven by differences in alveolar size. An implication of this theory is that larger and/or more inflated lungs would correspond to lower alveolar surface-to-volume ratio, which could be a key contributor to the apparent decrease in gas-exchange efficacy in larger and/or more inflated lungs. A natural direction for future study would be comparison of dissolved-phase ^{129}Xe MRI results at various lung volumes and inflation levels with those from diffusion-weighted ^{129}Xe MRI techniques designed to characterize voxel-wise mean alveolar size. Recent work has demonstrated single-breath-hold acquisition of both diffusion-weighted and dissolved-phase ^{129}Xe MR scans (7,8), and such techniques could be used to investigate and establish direct links between alveolar size and surface-to-volume ratio, lung volume, and ^{129}Xe MRI-derived gas uptake metrics. An ideal result of such work would be a model for lung volume correction of ^{129}Xe-derived gas uptake metrics incorporating alveolar geometry.

5.2.3. Free-breathing 4D ^{1}H lung MRI

This work is ripe for continued methodological development and improvement. One interesting avenue for improvement is the use of k-space samples collected both while moving away from the k-space center and while moving back toward the center, either reconstructing a single image with improved signal-to-noise ratio or reconstructing and comparing two separate images with slightly differing contrasts. As with the work shown in Chapter 2, image reconstruction accuracy might be improved by optimizing CS hyperparameters, particularly as ideal hyperparameters for bSSFP images likely differ from those for spoiled images. Improved reconstruction of non-end-of-exhalation image frames is of key importance, and various aspects of the reconstruction workflow might be altered in order to improve these frames. Improved respiratory phase binning would likely improve reconstruction of these frames by minimizing motion blurring present in respiratory frames prior to reconstruction. Direct incorporation of motion estimates into the reconstruction could also improve reconstruction performance, by allowing the high-fidelity reconstruction of end-of-exhalation frames to more directly inform reconstruction of frames at other respiratory phases (9,10).

A key potential application area for this technique is radiotherapy treatment planning and serial monitoring of lung and abdominal tumors and surrounding tissue areas during a course of radiation therapy. 4D computed tomography is an established method for planning and monitoring in this context (11,12), but suffers from disadvantages that include low soft-tissue

contrast relative to MR, susceptibility to motion artifacts (13), and high radiation dose (14). 4D-MRI techniques are therefore of significant established interest for this purpose (15), and the specific bSSFP techniques presented in this work could be particularly suited to tumor monitoring and treatment given the high observed SNR in vasculature. It was originally intended that individuals with lung tumors would be enrolled in the 4D-MRI study described in this work, but difficulties with patient availability and enrollment have precluded this to date.

Additionally, it is important to investigate and establish the potential utility of these techniques for evaluation of disease type and burden in diseases that impact lung parenchymal density. Pediatric lung conditions that affect parenchymal density and that CT imaging is commonly used to diagnose and/or monitor are of particular interest, as serial disease monitoring using MRI is potentially more appealing than using CT due to the high effective risk of stacked CT radiation doses in younger individuals relative to that in older individuals (16,17). An example condition of interest is pulmonary alveolar proteinosis (PAP), which is characterized by filling of alveoli with lipoproteinaceous material and which has a characteristic presentation in CT images (18,19). High-signal, high-resolution MR imaging with strong signal in parenchyma and vasculature serve as a useful tool for diagnosis and characterization of treatment response in PAP, and potentially as a tool to assist interventional planning as well (20).

5.3. References

1.	Wu EX, Towe CW, Tang H. MRI cardiac tagging using a sinc-modulated RF pulse train. Magnetic Resonance in Medicine. 2002;48(2):389–93.

2.	Zibetti MVW, Herman GT, Regatte RR. Fast data-driven learning of parallel MRI sampling patterns for large scale problems. Sci Rep. 2021 Sep 29;11(1):19312.

3.	Tustison NJ, Awate SP, Cai J, Altes TA, Miller GW, de Lange EE, et al. Pulmonary kinematics from tagged hyperpolarized helium-3 MRI. J Magn Reson Imaging. 2010 May;31(5):1236–41.

4.	Cui T, Miller GW, Mugler JP, Cates GD, Mata JF, de Lange EE, et al. An initial investigation of hyperpolarized gas tagging magnetic resonance imaging in evaluating deformable image registration-based lung ventilation. Med Phys. 2018 Dec;45(12):5535–42.

5. Plummer JW, Willmering MM, Cleveland ZI, Towe C, Woods JC, Walkup LL. Childhood to adulthood: Accounting for age dependence in healthy-reference distributions in 129Xe gas-exchange MRI. Magn Reson Med. 2023 Mar;89(3):1117–33.

6. Brown RH, Wise RA, Kirk G, Drummond MB, Mitzner W. Lung Density Changes With Growth and Inflation. Chest. 2015 Oct 1;148(4):995–1002.

7. Zhong J, Zhang H, Ruan W, Xie J, Li H, Deng H, et al. Simultaneous assessment of both lung morphometry and gas exchange function within a single breath-hold by hyperpolarized 129Xe MRI. NMR in Biomedicine. 2017;30(8):e3730.

8. Xie J, Li H, Zhang H, Zhao X, Shi L, Zhang M, et al. Single breath-hold measurement of pulmonary gas exchange and diffusion in humans with hyperpolarized 129Xe MR. NMR in Biomedicine. 2019;32(5):e4068.

9. Miller Z, Torres L, Fain S, Johnson K. Motion Compensated Extreme MRI: Multi-Scale Low Rank Reconstructions for Highly Accelerated 3D Dynamic Acquisitions (MoCo-MSLR) [Internet]. arXiv; 2022 [cited 2023 Oct 22]. Available from: http://arxiv.org/abs/2205.00131

10. Miller Z, Johnson KM. Motion compensated self supervised deep learning for highly accelerated 3D ultrashort Echo time pulmonary MRI. Magn Reson Med. 2023 Jun;89(6):2361–75.

11. Qin Y, Zhang F, Yoo DS, Kelsey CR, Yin FF, Cai J. Adaptive stereotactic body radiation therapy planning for lung cancer. Int J Radiat Oncol Biol Phys. 2013 Sep 1;87(1):209–15.

12. Ding K, Bayouth JE, Buatti JM, Christensen GE, Reinhardt JM. 4DCT-based measurement of changes in pulmonary function following a course of radiation therapy. Med Phys. 2010 Mar;37(3):1261–72.

13. Mutaf YD, Antolak JA, Brinkmann DH. The impact of temporal inaccuracies on 4DCT image quality. Med Phys. 2007 May;34(5):1615–22.

14. Li T, Schreibmann E, Thorndyke B, Tillman G, Boyer A, Koong A, et al. Radiation dose reduction in four-dimensional computed tomography. Med Phys. 2005 Dec;32(12):3650–60.

15. Stemkens B, Paulson ES, Tijssen RHN. Nuts and bolts of 4D-MRI for radiotherapy. Phys Med Biol. 2018 Oct 23;63(21):21TR01.

16. Brenner DJ. Effective dose: a flawed concept that could and should be replaced. BJR. 2008 Jul;81(967):521–3.

17. Mayo JR. Radiation Dose Issues in Longitudinal Studies Involving Computed Tomography. Proc Am Thorac Soc. 2008 Dec 15;5(9):934–9.

18.   Bush A, Pabary R. Pulmonary alveolar proteinosis in children. Breathe. 2020 Jun 1;16(2):200001.

19.   Berteloot L, Taam RA, Emond-Gonsard S, Mamou-Mani T, Lambot K, Grévent D, et al. Primary pulmonary alveolar proteinosis: computed tomography features at diagnosis. Pediatr Radiol. 2014 Jul 1;44(7):795–802.

20.   Wilson CA, Arthurs OJ, Black AE, Schievano S, Hunt C, van Hoog S, et al. Printed three-dimensional airway model assists planning of single-lung ventilation in a small child. Br J Anaesth. 2015 Oct;115(4):616–20.

Appendix: List of publications, presentations, and awards

Publications

Garrison WJ, Mugler JP, Mata JF, Nunoo-Asare RN, Shim YM, Miller GW. Acquiring hyperpolarized ^{129}Xe magnetic resonance images of lung ventilation. J Vis Exp. 201:e65982 (2023).

Garrison WJ, Qing K, He M, Zhao L, Tustison NJ, Patrie JT, Mata JF, Shim YM, Ropp AM, Altes TA, Mugler JP, Miller GW. Lung volume dependence and repeatability of hyperpolarized ^{129}Xe MRI gas uptake metrics in healthy volunteers and patients with COPD. Radiol Cardiothorac Imaging. 5(3):220096 (2023).

Garrison WJ, Qing K, Tafti S, Mugler JP, Shim YM, Mata JF, Cates GD, de Lange EE, Meyer CH, Cai J, Miller GW. Highly accelerated dynamic acquisition of 3D grid-tagged hyperpolarized-gas lung images using compressed sensing. Magn Reson Med. 89(6):2255-2263 (2023).

Sheybani ND, Witter AR, **Garrison WJ**, Miller GW, Price RJ, Bullock TNJ. Profiling of the immune landscape in murine glioblastoma following blood brain/tumor barrier disruption with MR image-guided focused ultrasound. J. Neurooncol. 156(1):109-122 (2022).

Mathew AS, Gorick CM, Thim EA, **Garrison WJ**, Klibanov AL, Miller GW, Sheybani ND, Price RJ. Transcriptomic response of brain tissue to focused ultrasound-mediated blood-brain barrier disruption depends strongly on anesthesia. Bioeng. Transl. Med. 6(2):e10198 (2020).

Tafti S, **Garrison WJ**, Mugler JP, Shim YM, Altes TA, Mata JF, de Lange EE, Cates GD, Ropp AM, Wang C, Miller GW. Emphysema index based on hyperpolarized ^{3}He or ^{129}Xe diffusion MRI: performance and comparison with quantitative CT and pulmonary function tests. Radiology 297(1):201-210 (2020).

Curley CT, Stevens AD, Mathew AS, Stasiak K, **Garrison WJ**, Miller GW, Sheybani ND, Engelhard VH, Bullock TNJ, Price RJ. Immunomodulation of intracranial melanoma in response to blood-tumor barrier opening with focused ultrasound. Theranostics 10(19):8821-8833 (2020).

Curley CT, Mead BP, Negron K, Kim N, **Garrison WJ**, Miller GW, Kingsmore KM, Thim EA, Song J, Munson JM, Klibanov AL, Suk JS, Hanes J, Price RJ. Augmentation of brain tumor interstitial flow via focused ultrasound promotes brain-penetrating nanoparticle dispersion and transfection. Sci. Adv. 6(18):eaay1344 (2020).

Gorick CM, Mathew AS, **Garrison WJ**, Thim EA, Fisher DG, Copeland CA, Song J, Klibanov AL, Miller GW, Price RJ. Sonoselective transfection of cerebral vasculature without blood-brain barrier disruption. Proc. Natl. Acad. Sci. U. S. A. 117(11):5644-5654 (2020).

Mead BP, Curley CT, Kim N, Negron K, **Garrison WJ**, Song J, Rao D, Miller GW, Mandell JW, Purow BW, Suk JS, Hanes J, Price RJ. Focused ultrasound preconditioning for augmented nanoparticle penetration and efficacy in the central nervous system. Small 15(49):e1903460 (2019).

Presentations

Garrison WJ, Qing K, He M, Zhao L, Tustison NJ, Mata JF, Shim YM, Ropp AM, Altes TA, Mugler JP, Miller GW. Lung volume dependence and repeatability of hyperpolarized ^{129}Xe MRI gas uptake metrics in healthy volunteers and patients with COPD. Oral presentation at the annual University of Virginia Radiology Research Week, Charlottesville, VA (2023).

Garrison WJ, Qing K, He M, Zhao L, Tustison NJ, Mata JF, Shim YM, Ropp AM, Altes TA, Mugler JP, Miller GW. Lung volume dependence and repeatability of hyperpolarized ^{129}Xe MRI gas uptake metrics in healthy volunteers and patients with COPD. Oral presentation at the biennial International Workshop on Pulmonary Imaging, Philadelphia, PA (2023).

Garrison WJ, Qing K, Tafti S, Mugler JP, Shim YM, Mata JF, Cates GD, de Lange EE, Meyer CH, Cai J, Miller GW. 4D MRI of lung biomechanics: highly accelerated dynamic acquisition of 3D grid-tagged ^{3}He lung images. Poster presentation at the biennial Gordon Research Conference on In Vivo Magnetic Resonance, Andover, NH (2022).

Garrison WJ, Miller GW, Qing K, Shim YM, Mata JF, He M, Altes TA, Cassani JM, Struchen SE, Nunoo-Asare RN, Tustison NJ, Ropp AM, Mugler JP. Same-session repeatability of hyperpolarized ^{129}Xe MRI gas uptake measures in healthy subjects and subjects with COPD.

Poster presentation at the annual meeting of the International Society for Magnetic Resonance in Medicine, online (2021).

Garrison WJ, Qing K, Tafti S, Mugler JP, Shim YM, Mata JF, Cates GD, de Lange EE, Meyer CH, Cai J, Miller GW. 4D-MRI of lung biomechanics: highly accelerated dynamic acquisition of 3D grid-tagged He-3 lung images using compressed sensing. Oral presentation at the annual University of Virginia Radiology Research Week, Charlottesville, VA (2021).

Garrison WJ, Qing K, Tafti S, Mugler JP, Shim YM, Mata JF, Cates GD, de Lange EE, Meyer CH, Cai J, Miller GW. Toward 4D MRI of lung biomechanics: highly accelerated dynamic acquisition of 3D grid-tagged He-3 lung images using compressed sensing. Oral and poster presentation at the biennial International Workshop on Pulmonary Imaging, Philadelphia, PA (2019).

Garrison WJ. Toward 4-D MRI of lung biomechanics: under-sampling and compressed sensing reconstruction of 3-D grid-tagged He-3 lung images. Oral presentation at the annual University of Virginia Graduate Biomedical Engineering Society Student Summer Seminar Series, Charlottesville, VA (2018).

Garrison WJ, Qing K, Tafti S, Mugler JP, Shim YM, Mata JF, Cates GD, de Lange EE, Meyer CH, Cai J, Miller GW. Highly accelerated dynamic acquisition of 3D grid-tagged He-3 lung images using compressed sensing. Electronic poster presentation at the annual meeting of the International Society for Magnetic Resonance in Medicine, Paris, FR (2018).

Awards

University of Virginia Radiology Research Week – Best Overall Presentation (2023)

International Workshop on Pulmonary Imaging – Junior Speaker Stipend (2019, 2023)

International Society for Magnetic Resonance in Medicine – Annual Meeting Educational Stipend (2018, 2021)

Focused Ultrasound Foundation – Winter School on Therapeutic Ultrasound Scholarship (2019)